國立交通大學

電子工程學系電子研究所碩士班

碩士論文

以濺鍍法製備氮摻雜二氧化鈦薄膜物性及光學特性之研究

Physical and Optical Characteristics of Sputtered Deposited $TiO_{2-x}N_x$ Thin Films

研究生：余松蒔

指導教授：曾俊元博士

中華民國九十六年七月

以濺鍍法製備氮摻雜二氧化鈦薄膜物性及光學特性之研究

Physical and Optical Characteristics of Sputtered Deposited $TiO_{2-x}N_x$ Thin Films

研 究 生：余松蒔　　Student： Sung-Shih Yu

指導教授：曾俊元　　Advisor：Tseung-Yuen Tseng

國 立 交 通 大 學

電子工程學系電子研究所碩士班

碩 士 論 文

A Thesis

Submitted to Department of Electronics Engineering & Institute of Electronics

College of Electrical and Computer Engineering

National Chiao Tung University

in partial Fulfillment of the Requirements

For the Degree of

Master

in

Electronics Engineering

June 2007

Hsinchu, Taiwan, Republic of China

中華民國九十六年七月

以濺鍍法製備氮摻雜二氧化鈦薄膜物性及光學特性之研究

研究生：余松蒔　　指導教授：曾俊元 博士

國立交通大學

電子工程學系　　電子研究所碩士班

摘　要

本論文中，是探討以濺鍍法使用TiN鈀在混合N_2/O_2比例的條件下長氮摻雜二氧化鈦薄膜於塑膠和玻璃上。從UV-VIS吸收光譜儀可以觀察到在PET和玻璃上的摻雜氮的二氧化鈦薄膜有特殊的吸收度曲線往電子能階較低的可見光波段區移動。氮摻雜二氧化鈦薄膜厚度越厚吸收度越高，而且在可見光波段區有越明顯的峰值。此薄膜的電子能階會隨著氮摻雜的濃度升高而縮小。鍍有此薄膜的塑膠和玻璃基板用紫外光和可見光照射會表現爲低接觸角的特性。在濺鍍功率爲 20 瓦到 120 瓦，60 分鐘的濺鍍時間和 5%氮的情況下，此薄膜在塑膠上

分別照射紫外光和可見光可以得到的接觸角爲最好的情況分別爲 8 度和 35 度。在濺鍍功率爲 60 瓦到 100 瓦，60 分鐘到 90 分鐘的濺鍍時間和 12.3%氮的情況下，此薄膜在玻璃上分別照射紫外光和可見光可以得到的接觸角爲最好的情況分別爲 4 度和 30 度。接觸角的好壞除了他本身照射光後的親水特性好壞之外，也跟他的表面粗糙程度有關。

Physical and Optical Characteristics of Sputtered Deposited $TiO_{2-x}N_x$ Thin Films

Student: Sung-Shih Yu Advisor: Dr. Tseung-Yuen Tseng

Department of Electronics Engineer and Institute of Electrics

National Chiao Tung University

Abstract

In this thesis, the nitrogen-doped thin films were prepared on PET and glass plates using sputtering method with TiN target under a N_2/O_2 gas mixture. UV-VIS absorbance spectroscopy of PET and glass coated with $TiO_{2-x}N_x$ thin films appear a significant shift of the absorption edge to a lower energy in the visible-light region for both PET and glass substrates. Absorption spectra of $TiO_{2-x}N_x$ thin films obtain higher intensity with increasing thickness, and appear absorption peaks in the visible region. The energy band gaps of $TiO_{2-x}N_x$ thin films narrow with increasing nitrogen. PET and glass plates coated with $TiO_{2-x}N_x$ thin films were found to exhibit a low water contact angle than without coated membranes when the surfaces were illuminated with UV and visible light in the air. In the conditions of 20~120W power supply, 60min sputtering time and 5% nitrogen flow ratios, the $TiO_{2-x}N_x$ thin film on the PET substrate upon UV-VIS light illumination exhibits lowest water contact angle near 8° and 35° respectively. In the conditions of 60~100W power supply, 60~90min sputtering time and 12.3% nitrogen flow ratios, the $TiO_{2-x}N_x$ thin film on the glass substrate upon UV-VIS light illumination exhibits lowest water contact angle near 4° and 30° respectively.

Roughness and the photo-induced surface wettability conversion reaction of the thin films affect the degrees of water contact angles.

致謝

首先誠摯的感謝指導教授曾俊元博士，老師悉心的教導使我得以一窺固態電子領域的深奧，不時的討論並指點我正確的方向，使我在這些年中獲益匪淺。老師對學問的嚴謹更是我輩學習的典範。

本論文的完成另外亦得感謝周秀玉學姊的大力協助。因爲有你的體諒及幫忙，使得實驗與本論文能夠更完整而嚴謹。

兩年裡的日子，實驗室裡共同的生活點滴，學術上的討論、敗戰隊友遠永都不離不棄、義氣到底的革命情感、因爲偷懶睡太晚而衝衝忙忙閃進實驗室.....，感謝眾位學長姐、同學、學弟妹的共同砥礪，你/妳們的陪伴讓兩年的研究生活變得絢麗多彩。

感謝秀玉學姐、群傑、志洋、猛男、小僑學長們不厭其煩的指出我研究中的缺失，且總能在我迷惘時爲我解惑，也感謝小尤、囧興、冠仲、承佑、重毅、陰帝、阿傑同學的幫忙，恭喜我們順利走過這兩年。實驗室的含一含、黑之、翁翁翁、阿兩、莊文仁學弟們當然也不能忘記，你們的幫忙及搞笑我銘感在心。

女朋友琳蓁在背後的默默支持更是我前進的動力，沒有琳蓁的體諒、包容，相信這兩年的生活將是很不一樣的光景。

最後，謹以此文獻給我摯愛的雙親。

Contents

Chinese Abstract……. II

English Abstract……. IV

Acknowledgements…… VI

Contents……. VII

Figure Captions…….. X

Table Captions…… XVIII

Chapter 1 Introduction…….....1

1.1 Introduction of TiO_2.....1

1.2 Material Groups and Structure of TiO_2.....2

1.3 Characteristic of $TiO_{2-x}N_x$.....10

1.4 Applications of TiO_2.....14

1.5 Polyethylene Terephthalate.....16

1.5.1 Introduction 16

1.5.2 Crystals 19

1.5.3 Applications...19

1.6 Review.....21

1.6.1 XRD Patterns of N-doped TiO_2 21

1.6.2 XPS Patterns of N-doped TiO_2.....23

1.6.3 Absorption and Energy Band Gap.....25

1.6.4 Water Contact Angle.....27

Chapter 2 Experiment Details……...…….28

2.1 System of Radio-Frequency Magnetron Sputter.....28

2.2 Thin Films Preparation by Sputter……...……30

2.3 The process of experiment……..…31

2.4 Measurements and Materials Analysis……...…….33

2.4.1 X-Ray Diffraction……..……33

2.4.2 Scanning Probe Microscopy……....33

2.4.3 Scanning Electron Microscopy……..…….35

2.4.4 X-ray Photoelectron Spectroscopy ……...…36

2.4.5 Ultraviolet-Visible Spectrophotometers……..…...36

2.4.6 Contact Angle System……..….37

2.4.7 Raman Spectroscopy……..…38

Chapter 3 Results and Discussion……...…...……39

3.1 Crystal of $TiO_{2-x}N_x$……..……39

3.2 Composition of $TiO_{2-x}N_x$……43

3.3 Thickness of Different Power……....47

3.4 The Relation between Absorption to Band Gap of TiO2-xNx……...52

3.5 The Water Contact Angle……...…59

3.6 Roughness Effects The Water Contact Angle……....66

3.7 Intensity of Light Effects The Water Contact Angle……....71

3.8 The Absorption on Different Bases of PET and Glass……..…72

3.9 The effect of Sputter's Power and Time for Absorption……..80

Chapter 4 Conclusions……...……..…84

References……..…….…….….86

Vita……..…….….…….90

Figure Captions

Chapter 1

Figure 1-1 The unit cell of rutile…….….5

Figure 1-2 The crystal structure of rutile…….....6

Figure 1-3 Ball-and-stick model of anatase's unit cell……8

Figure 1-4 The crystal structure of anatase……..9

Figure 1-5 Image from a video contact angle device which water drops on glass……...……..11

Figure 1-6 Chemical structure of polyethylene terephthalate……...…….17

Figure 1-7 Light absortion spectrum of polyethylene terephthalate measured using a light spectrophotometer……...……17

Figure 1-8 XRD patterns of N-doped TiO_2 films deposited with NH_3 flow rate of 150 sccm before and after annealing……...22

Figure 1-9 UV-visible absorption spectra of anatase and rutile TiO_2 nanoparticles in water……..22

Figure 1-10 N 1s XPS spectra of $TiO_{2-x}N_x$ and TiO_2 powders……..23

Figure 1-11 N 1 s X-ray photoelectron spectra of $TiO_{2-x}N_x$ (upper trace) and TiO_2 powders (lower trace)…….…24

Figure 1-12 XPS spectra of N-doped TiO_2 films deposited with NH3 flow rate of 150 sccm: N 1s respectively……...…….25

Figure 1-13. A): UV/Vis diffuse reflectance spectra of the samples. B): Plot of the modified Kubelka – Munk function versus the photon energy of the samples. (a) After doping with nitrogen. (b) Commercial UV photocatalyst. Doping conditions: 10 min at 873 K under a stream of ammonia gas……..….26

Figure 1-14 Models of the energy band gap structure of $TiO_{2-x}N_x$ for response in the visible-light region…….27

Figure 1-15 Water contact angle of N-doped TiO_2 films as a function of visible- or UV-light irradiation time……..…..28

Chapter 2

Figure 2-1 The illustration of our solution for $TiO_{2-X}N_X$ preparation flow…...30

Figure 2-2 The illustration of our experiment flow……...…32

Figure 2-3 Block diagram of atomic force microscope…….34

Figure 2-4 Image of contact angle goniometer system……...…37

Chapter 3

Figure 3-1 XRD profiles of the $TiO_{2-X}N_X$ thin film which conditions of power and treatment time are the same and no substrate temperature…...40

Figure 3-2 XRD profiles of the $TiO_{2-X}N_X$ thin film which conditions of treatment time and gas are the same and no substrate temperature…….…….40

Figure 3-3 XRD profiles of the $TiO_{2-X}N_X$ thin film which conditions of power and treatment time are the same after 500°C annealing and no substrate temperature…….……..41

Figure 3-4 XRD profiles of the $TiO_{2-X}N_X$ thin film which conditions of treatment time and gas are the same after 500°C annealing and no substrate temperature…….……..41

Figure 3-5 Raman profiles of the $TiO_{2-X}N_X$ thin film before annealing and no substrate temperature…….……..42

Figure 3-6 XPS spectra of Ti 2p peaks of the $TiO_{2-X}N_X$ thin film deposited by 100W power supply for 60min sputtering time and no substrate temperature……..44

Figure 3-7 XPS spectra of O 1s peaks of the $TiO_{2-X}N_X$ thin film deposited by 100W power supply for 60min sputtering time and no substrate temperature…….….45

Figure 3-8 XPS spectra of N 1s peaks of the $TiO_{2-X}N_X$ thin film deposited by 100W power supply for 60min sputtering time and no substrate temperature……..45

Figure 3-9 SEM images of the $TiO_{2-x}N_x$ thin film deposited by 60min sputtering time and N_2/O_2=7/2 flow rate with (a) 20W (b) 40W power supply……..…….48

Figure 3-10 SEM images of the $TiO_{2-x}N_x$ thin film deposited by 60min sputtering time and N_2/O_2=7/2 flow rate with (a) 60W (b) 80W power supply……...….49

Figure 3-11 SEM images of the $TiO_{2-x}N_x$ thin film deposited by 60min sputtering time and N_2/O_2=7/2 flow rate with (a) 100W (b) 120W power supply……..……..50

Figure 3-12 Top view image of the $TiO_{2-x}N_x$ thin film……..51

Figure 3-13 UV-visible absorption spectra of the $TiO_{2-x}N_x$ thin film deposited by 60min sputtering time and N_2/O_2=6.5/6.0 flow rate with various power supply……...…….54

Figure 3-14 Plots of the square root of the Kubelka-Munk function against the photon energy of the $TiO_{2-x}N_x$ thin film deposited by 60min sputtering time and N_2/O_2=6.5/6.0 flow rate with various power supply…….……..54

Figure 3-15 UV-visible absorption spectra of the $TiO_{2-x}N_x$ thin film deposited by 60min sputtering time and N_2/O_2=7/2 flow rate with various power supply……..……..55
Figure 3-16 Plots of the square root of the Kubelka-Munk function against the photon energy of the $TiO_{2-x}N_x$ thin film deposited by 60min sputtering time and N_2/O_2=7/2 flow rate with various power supply……...55
Figure 3-17 UV-visible absorption spectra of the $TiO_{2-x}N_x$ thin film deposited by 60min sputtering time and N_2/O_2=9/0 flow rate with various power supply……...….56
Figure 3-18 Plots of the square root of the Kubelka-Munk function against the photon energy of the $TiO_{2-x}N_x$ thin film deposited by 60min sputtering time and N_2/O_2=9/0 flow rate with various power supply…….……..56
Figure 3-19 UV-visible absorption spectra of the $TiO_{2-x}N_x$ thin film deposited by 90min sputtering time and N_2/O_2=9/0 flow rate with various power supply……...….57
Figure 3-20 Plots of the square root of the Kubelka-Munk function against the photon energy of the $TiO_{2-x}N_x$ thin film deposited by 90min sputtering time and N_2/O_2=9/0 flow rate with various power supply……...57
Figure 3-21 Plots of the square root of the Kubelka-Munk function against the photon energy of the $TiO_{2-x}N_x$ thin film deposited by 60min sputtering time and 100W power supply with different ratio of N_2/O_2……....58
Figure 3-22 Water contact angle images of the $TiO_{2-x}N_x$ thin film deposited by

40W sputtering for 60min with N_2/O_2=6.5/6.0 flow rate upon UV-light illumination……..….61

Figure 3-23 Water contact angle profiles of the $TiO_{2-x}N_x$ thin film deposited by 20W sputtering for 60 min with various x……...62

Figure 3-24 Water contact angle profiles of the $TiO_{2-x}N_x$ thin film deposited by 40W sputtering for 60 min with various x…….…..62

Figure 3-25 Water contact angle profiles of the $TiO_{2-x}N_x$ thin film deposited by 60W sputtering for 60 min with various x…….…..63

Figure 3-26 Water contact angle profiles of the $TiO_{2-x}N_x$ thin film deposited by 80W sputtering for 60 min with various x……...……63

Figure 3-27 Water contact angle profiles of the $TiO_{2-x}N_x$ thin film deposited by 100W sputtering for 60 min with various x…….64

Figure 3-28 Water contact angle profiles of the $TiO_{2-x}N_x$ thin film deposited by 120W sputtering for 60 min with various x…….64

Figure 3-29 Water contact angle profiles of the $TiO_{2-x}N_x$ thin film upon UV-VIS light illumination……...……65

Figure 3-30 The effect of extra Ar plasma for water contact angle of the $TiO_{2-x}N_x$ thin film deposited by 100W power sputtering for 90min with N_2/O_2=9/0 flow rate…….67

Figure 3-31 Roughness of the $TiO_{2-x}N_x$ thin film deposited by 100W sputtering for 90min with N_2/O_2=9/0 flow rate with extra Ar plasma treatment……..…67

Figure 3-32 Roughness of the $TiO_{2-x}N_x$ thin film deposited by 100W sputtering for 90min with N_2/O_2=9/0 flow rate without extra Ar plasma treatment……..…68

Figure 3-33 3D AFM images of the $TiO_{2-x}N_x$ thin film deposited by 100W

sputtering for 90min with N_2/O_2=9/0 flow rate with extra Ar plasma treatment……..68

Figure 3-34 3D AFM images of the $TiO_{2-x}N_x$ thin film deposited by 100W sputtering for 90min with N_2/O_2=9/0 flow rate without extra Ar plasma treatment……..…69

Figure 3-35 The effect of roughness for the water contact angle of the $TiO_{2-x}N_x$ thin film deposited with the same conditions…….…….69

Figure 3-36 Roughness of another $TiO_{2-x}N_x$ thin film deposited by 100W sputtering for 90min with N_2/O_2=9/0 flow rate without extra Ar plasma……..70

Figure 3-37 The $TiO_{2-x}N_x$ thin film illuminated upon different light intensity……71

Figure 3-38 UV-visible absorption spectra of the $TiO_{2-x}N_x$ thin film deposited on basis of glass by 90min sputtering time and N_2/O_2=9/0 flow rate with various power supply……...73

Figure 3-39 UV-visible absorption spectra of the $TiO_{2-x}N_x$ thin film deposited on basis of glass and PET by 90min sputtering time and N_2/O_2=9/0 flow rate with 60W power supply……...74

Figure 3-40 UV-visible absorption spectra of the $TiO_{2-x}N_x$ thin film deposited on basis of glass and PET by 90min sputtering time and N_2/O_2=9/0 flow rate with 80W power supply……...74

Figure 3-41 UV-visible absorption spectra of the $TiO_{2-x}N_x$ thin film deposited on basis of glass and PET by 90min sputtering time and N_2/O_2=9/0 flow rate with 100W power supply……..…75

Figure 3-42 UV-visible absorption spectra of the $TiO_{2-x}N_x$ thin film deposited on basis of glass and PET by 90min sputtering time and N_2/O_2=9/0

flow rate with 120W power supply…….75

Figure 3-43 UV-visible absorption spectra of the $TiO_{2-x}N_x$ thin film deposited on basis of glass and PET by 90min sputtering time and N_2/O_2=9/0 flow rate with 120W power supply at UV region……...….76

Figure 3-44 Water contact angle images of the $TiO_{2-x}N_x$ thin film deposited by 120W sputtering for 90min with N_2/O_2=9/0 flow rate upon UV-light illumination……..…76

Figure 3-45 UV-visible absorption spectra of the $TiO_{2-x}N_x$ thin film deposited on basis of glass and PET by 90min sputtering time and N_2/O_2=9/0 flow rate with 120W power supply at visible region……..….77

Figure 3-46 Water contact angle images of the $TiO_{2-x}N_x$ thin film deposited by 120W sputtering for 90min with N_2/O_2=9/0 flow rate upon visible-light illumination…….77

Figure 3-47 Water contact angle images of the TiO2-xNx thin film deposited on bases of PET and glass……78

Figure 3-48 The roughness of the TiO2-xNx thin film deposited on base of PET…….78

Figure 3-49 The roughness of the TiO2-xNx thin film deposited on base of glass…….79

Figure 3-50 UV-visible absorption spectra of the $TiO_{2-x}N_x$ thin film deposited by 100W sputtering power supply and N_2/O_2=7/2 flow rate with various time…….81

Figure 3-51 SEM images of the $TiO_{2-x}N_x$ thin film deposited by 60min sputtering time and N_2/O_2=7/2 flow rate with 120W power supply……..81

Figure 3-52 SEM images of the $TiO_{2-x}N_x$ thin film deposited by 70min

sputtering time and N_2/O_2=7/2 flow rate with 100W power supply……...……82

Figure 3-53 SEM images of the $TiO_{2-x}N_x$ thin film deposited by 60min sputtering time and N_2/O_2=7/2 flow rate with 100W power supply……...…82

Figure 3-54 UV-visible absorption spectra of the $TiO_{2-x}N_x$ thin film deposited through N_2/O_2=7/2 flow rate with various time and power supply in order to get the same thickness……...….83

Table Captions

Table 1-1 Properties of PET…….…….18

Table 2-1 Established types of scanning probe microscopy…….……..…35

Table 3-1 The composition of the $TiO_{2-x}N_x$ thin films with no substrate temperature……...……...46

Table 3-2 Growth rate of the $TiO_{2-x}N_x$ thin film with various power…. ……..51

Chapter 1 Introduction

1.1 Introduction of TiO_2

The discovery of the super-hydrophilicity on TiO_2 thin film surface has prompted extensive research on TiO_2 and other semiconductor materials such as ZnO, Ta_2O_5, In_2O_3, $InTaO_4$ or indium-tin oxides (ITO), which has been widely adopted as an important substance for solar energy conversion and environmental purification. Although various semiconductors have been studied, TiO_2 is known to be one of the most efficient and stable photocatalysts with respect to air or water purification and energy renewal. Its application spreads a wide variety of photochemical reaction, including used in photo-electrolysis, and solar cells. It was found out that the TiO_2 surface became slightly hydrophilic under UV irradiation. This wettability is originated in photo-generated holes produced in TiO_2. This highly hydrophilic phenomenon has been applied in various industrial items such as self-cleaning, exterior tiles, and antifogging mirrors. These applications have been limited to outdoor use only, as the super-hydrophilic conversion requires UV light irradiation of approximately the intensity as natural sunlight. The development of photo-induced sensitive in visual light irradiation condition is very important for indoor use. This photo-induced surface wettability conversion phenomenon has further aroused people's research interest in TiO_2, which will potentially an important role in environmental purification and solar energy conversion. Several approaches have been used to modify the TiO_2 for use in visible light. The main researches were doping transition metal into TiO_2, fabricating reduced TiO_{2-x} photocatalyst and substituted nitrogen, carbon or sulfur to oxygen in TiO_2. However, doped materials suffer from a thermal instability, an increase of carrier-recombination centers, or the requirement of an expensive ion-implantation

facility. Asahi have calculated densities of states (DOSs) of the substitutional doping of C, N, F, P, or S for O in the anatase TiO_2 crystal, by the full potential liberalized augmented plane wave formalism in the framework of the local density approximation. The substitutional doping of N was the most effective because its P states contribute to the band-gap narrowing by mixing with O 2p states.

1. 2 Material Groups and Structure of TiO_2 [22] [23]

Titanium dioxide

Titanium dioxide, also known as titanium(IV) oxide or titania, is the naturally occurring oxide of titanium, chemical formula TiO_2.

Natural occurrence

Titanium dioxide occurs in four forms:

- rutile, a tetragonal mineral usually of prismatic habit, often twinned;
- anatase or octahedrite, a tetragonal mineral of dipyramidal habit;
- brookite, an orthorhombic mineral. Both anatase and brookite are relatively rare minerals;
- Titanium dioxide (B) or TiO_2(B), a monoclinic mineral.
- Titanium Oxide or TiO, as present in K and M spectral type stars.

Titanium dioxide occurrences in nature are never pure; it is found with contaminant metals such as iron. The oxides can be mined and serve as a source for commercial titanium. The metal can also be mined from other minerals such as ilmenite or leucoxene ores, or one of the purest forms, rutile beach sand.

- **Rutile**

Rutile is a mineral composed primarily of titanium dioxide, TiO_2.Rutile is the most common natural form of TiO_2, with two rarer polymorphs anatase (sometimes

known by the obsolete name 'octahedrite'), a tetragonal mineral of pseudo-octahedral habit; and brookite, an orthorhombic mineral.

Rutile has among the highest refractive indices of any known mineral and also exhibits high dispersion. Natural rutile may contain up to 10% iron and significant amounts of niobium and tantalum.

Rutile derives its name from the Latin rutilus, red, in reference to the deep red color observed in some specimens when viewed by transmitted light.

Occurrence :

Rutile is a common accessory mineral in high-temperature and high-pressure metamorphic rocks and in igneous rocks.

Rutile is the preferred polymorph of TiO_2 in such environments because it has the lowest molecular volume of the three polymorphs; it is thus the primary titanium bearing phase in most high pressure metamorphic rocks, chiefly eclogites. Brookite and anatase are typical polymorphs of rutile formed by retrogression of metamorphic rutile.

Within the igneous environment, rutile is a common accessory mineral in plutonic igneous rocks, although it is also found occasionally in extrusive igneous rocks, particularly those which have deep mantle sources such as kimberlites and lamproites. Anatase and brookite are found in the igneous environment particularly as products autogenic alteration during the cooling of plutonic rocks; anatase is also found formed within placer deposits sourced from primary rutile.

The occurrence of large specimen crystals is most common in pegmatites, skarns and particularly granite greisens.

Rutile is found as an accessory mineral in some altered igneous rocks, and in certain gneisses and schists. In groups of acicular crystals it is frequently seen penetrating quartz as in the "fléches d'amour" from Grisons, Switzerland.

Uses and economic importance:

Rutile, when present in large enough quantities in beach sands, forms an important constituent of heavy mineral sands ore deposits. It is primarily extracted for use in refractory manufacture or use as a base for paints. Rarely is it extracted as an ore of titanium.

Finely powdered rutile is a brilliant white pigment and is used in paints, plastics, papers, foods, and other applications that call for a bright white color. Titanium dioxide pigment is the single greatest use of titanium worldwide. Nanoscale particles of rutile are transparent to optical light but remain highly reflective to UV light. Hence, they are used in sunscreens.

Small rutile needles present in gems are responsible for an optical phenomenon known as asterism. Asteriated gems are known as "star" gems. Star sapphires, star rubies, and other "star" gems are highly sought after and often more valuable than their normal equivalents.

Synthetic rutile

Synthetic rutile was first produced in 1948 and is sold under a variety of names. Very pure synthetic rutile is transparent and almost colorless (slightly yellow) in large pieces. Synthetic rutile can be made in a variety of colors by doping, although the purest material is almost colorless. The high refractive index gives an adamantine lustre and strong refraction that leads to a diamond-like appearance. The

near-colorless diamond substitute is sold under the name Titania, which is the old-fashioned chemical name for this oxide. However, rutile is seldom used in jewellery because it is not very hard (scratch-resistant), measuring only about 6 on the Mohs hardness scale.

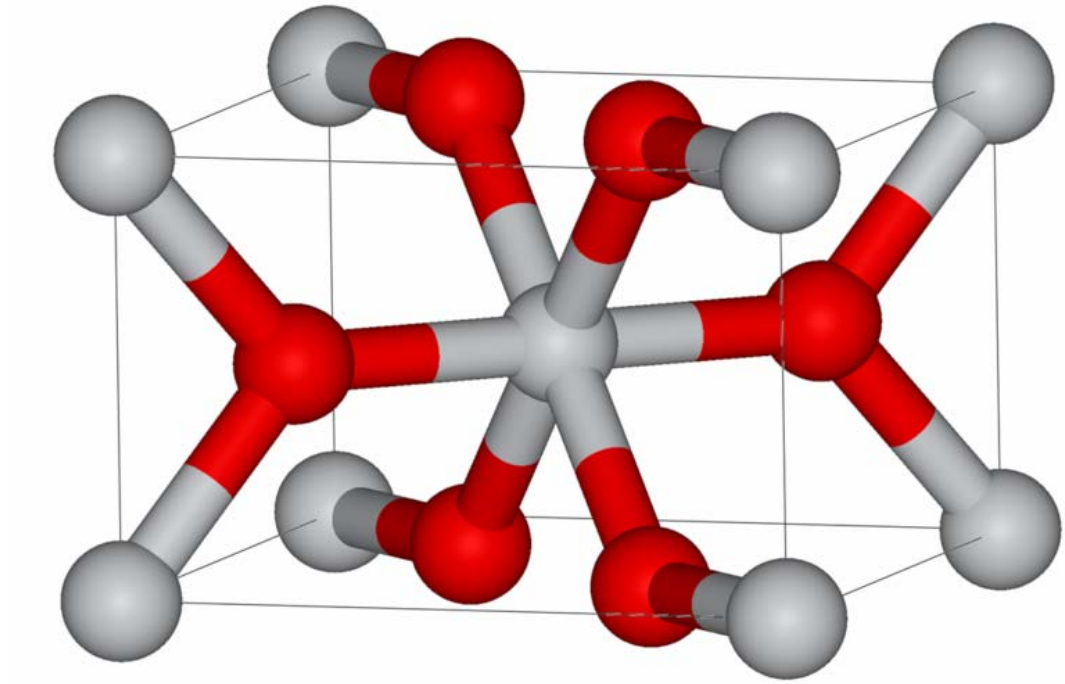

Figure 1-1 The unit cell of rutile

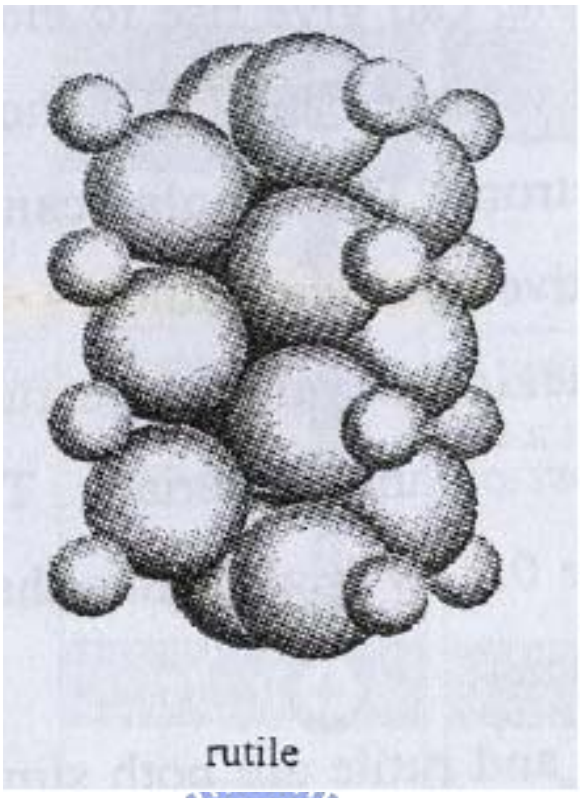

Figure 1-2 The crystal structure of rutile .

- **Anatase** [24]

Anatase is one of the three mineral forms of titanium dioxide (the other two being brookite and rutile). It is always found as small, isolated and sharply developed crystals, and like rutile, a more commonly occurring modification of titanium dioxide, it crystallizes in the tetragonal system; but, although the degree of symmetry is the same for both, there is no relation between the interfacial angles of the two minerals, except, of course, in the prism-zone of 45° and 90°. The common pyramid of anatase, parallel to the faces of which there are perfect cleavages, has an angle over the polar edge of 82°9', the corresponding angle of rutile being 56°52½'It was on account of this steeper pyramid of anatase that the mineral was named, by RJ Haüy in 1801, from the Greek anatasis, "extension," the vertical axis of the crystals being longer than in rutile. There are also important differences between the physical characters of anatase and rutile; the former is not quite so hard (H=5½-6) or dense

(specific gravity 3.9); it is optically negative, rutile being positive; and its lustre is even more strongly adamantine or metallic-adamantine than that of rutile.

Two types or habits of anatase crystals may be distinguished. The commoner occurs as simple acute double pyramids with an indigo-blue to black colour and steely lustre. Crystals of this kind are abundant at Le Bourg-d'Oisans in Dauphiné, where they are associated with rock-crystal, feldspar, and axinite in crevices in granite and mica-schist. Similar crystals, but of microscopic size, are widely distributed in sedimentary rocks, such as sandstones, clays, and slates, from which they may be separated by washing away the lighter constituents of the powdered rock.

Crystals of the second type have numerous pyramidal faces developed, and they are usually flatter or sometimes prismatic in habit; the colour is honey-yellow to brown. Such crystals closely resemble xenotime in appearance and, indeed, were for a long time supposed to belong to this species, the special name wiserine being applied to them. They occur attached to the walls of crevices in the gneisses of the Alps, the Binnenthal near Brig in canton Valais, Switzerland, being a well-known locality.

When strongly heated, anatase is converted into rutile, changing in specific gravity to 4.1; naturally occurring pseudomorphs of rutile after anatase are also known. Crystals of anatase have and continue to be artificially prepared in laboratories by introducing the moisture-sensitive titanium tetrachloride, $TiCl_4$, to water at very cold temperatures (the process is very exothermic) to produce TiO_2 and HCl gas. Such synthetic forms of anatase are currently under scrutiny in the field of semiconductors and photovoltaic materials.

Another name commonly in use for this mineral is octahedrite, a name which, indeed, is earlier than anatase, and given because of the common (acute) octahedral habit of the crystals. Other names, now obsolete, are oisanite and dauphinite, from the well-known French locality.

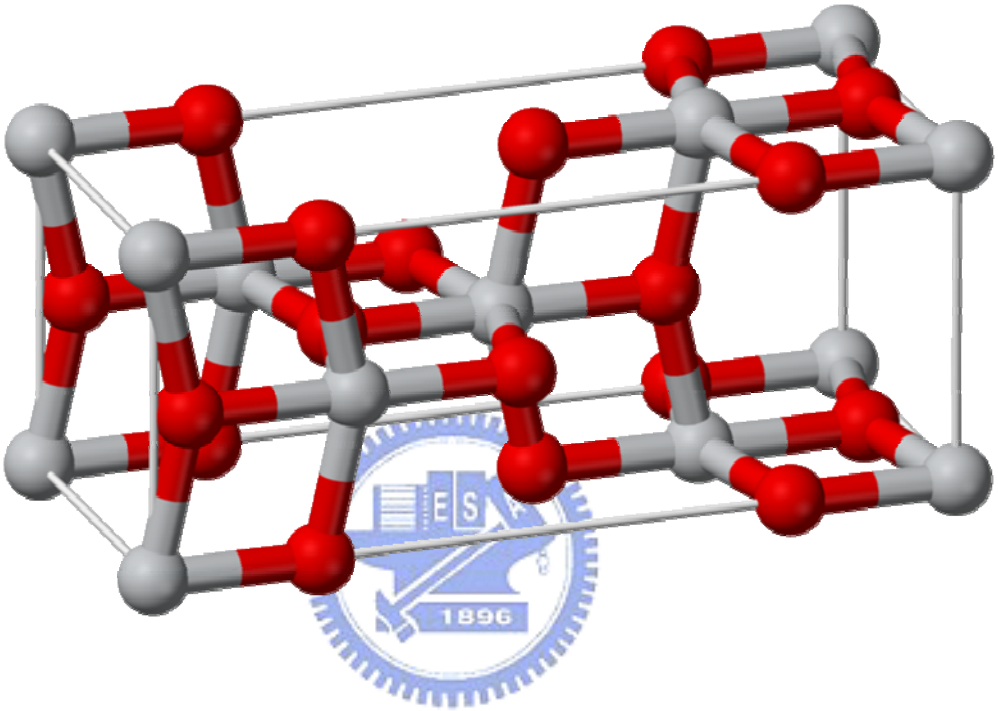

Figure 1-3 Ball-and-stick model of anatase's unit cell

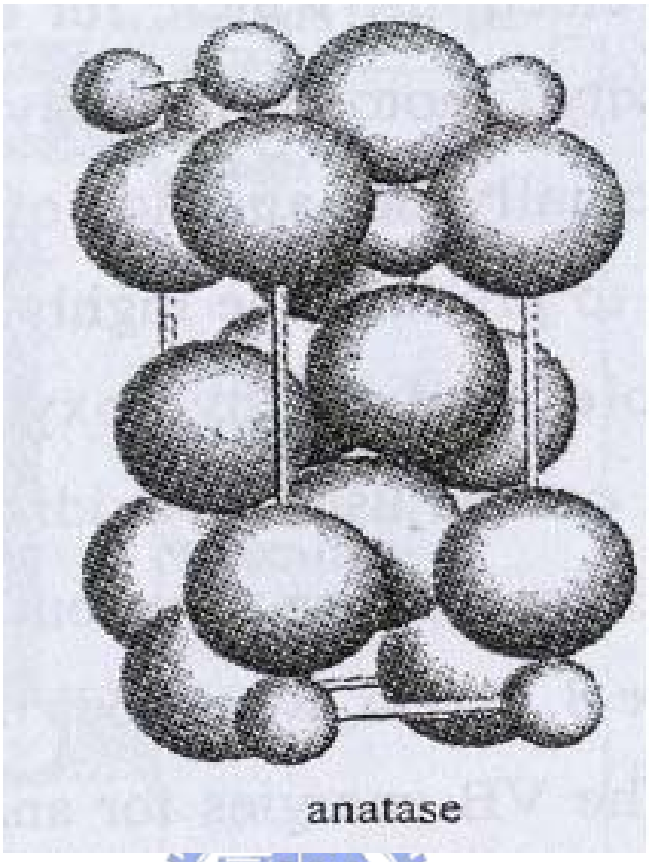

Figure 1-4 The crystal structure of anatase .

- **Brookite**

Brookite is a mineral consisting of titanium oxide, TiO_2, and hence identical with rutile and anatase in composition, but crystallizing in the orthorhombic system (see crystal structure).

It was named for Henry James Brooke, English mineralogist, 1771 - 1857.

- **Titanium dioxide (B)** [25] [26] [27] [28]

Titanium dioxide (B) or TiO_2(B) is the monoclinic form of titanium dioxide. The mineral is found in weathering rims on tektites and perovskite and as lamellae in

anatase from hydrothermal veins and has a density lower than that of the other three polymorphs.

In the laboratory anatase can be converted in a hydrothermal route to TiO_2(B) nanotubes and nanowires which are of potential interest as catalytic supports and photocatalysts. For this to happen anatase is mixed with 15M sodium hydroxide and heated at 150 °C for 72 hours. The reaction product is washed with dilute hydrochloric acid and heated at 400 °C for another 15 hours. the yield of nanotubes is quantitative and the tubes have an outer diameter of 10 to 20 nanometres and an inner diameter of 5 to 8 nanometres and have a length of 1 micrometres. A higher reaction temperature (170 °C) and less reaction volume gives the corresponding nanowires.

1.3 Characteristic of $TiO_{2-x}N_x$

UV-VIS light absorption

In physics, absorption is the process by which the energy of a photon is taken up by another entity, for example, by an atom whose valence electrons make transition between two electronic energy levels. The photon is destroyed in the process. The absorbed energy may be re-emitted as radiant energy or transformed into heat energy. The absorption of light during wave propagation is often called attenuation.

The absorbance of an object quantifies how much light is absorbed by it. This may be related to other properties of the object through the Beer-Lambert law.

For most substances, the amount of absorption varies with the wavelength of the light, leading to the appearance of colour in pigments that absorb some wavelengths but not others. For example, an object that absorbs blue, green and

yellow light will appear red when viewed under white light. More precise measurements at many wavelengths allow the identification of a substance via absorption spectroscopy.

Contact angle [29][31]

The contact angle is the angle at which a liquid/vapor interface meets the solid surface. The contact angle is specific for any given system and is determined by the interactions across the three interfaces. Most often the concept is illustrated with a small liquid droplet resting on a flat horizontal solid surface. The shape of the droplet is determined by the Young-Laplace equation. The contact angle plays the role of a boundary condition. Contact angle is measured using a contact angle goniometer. The contact angle is not limited to a liquid/vapour interface; it is equally applicable to the interface of two liquids or two vapours.

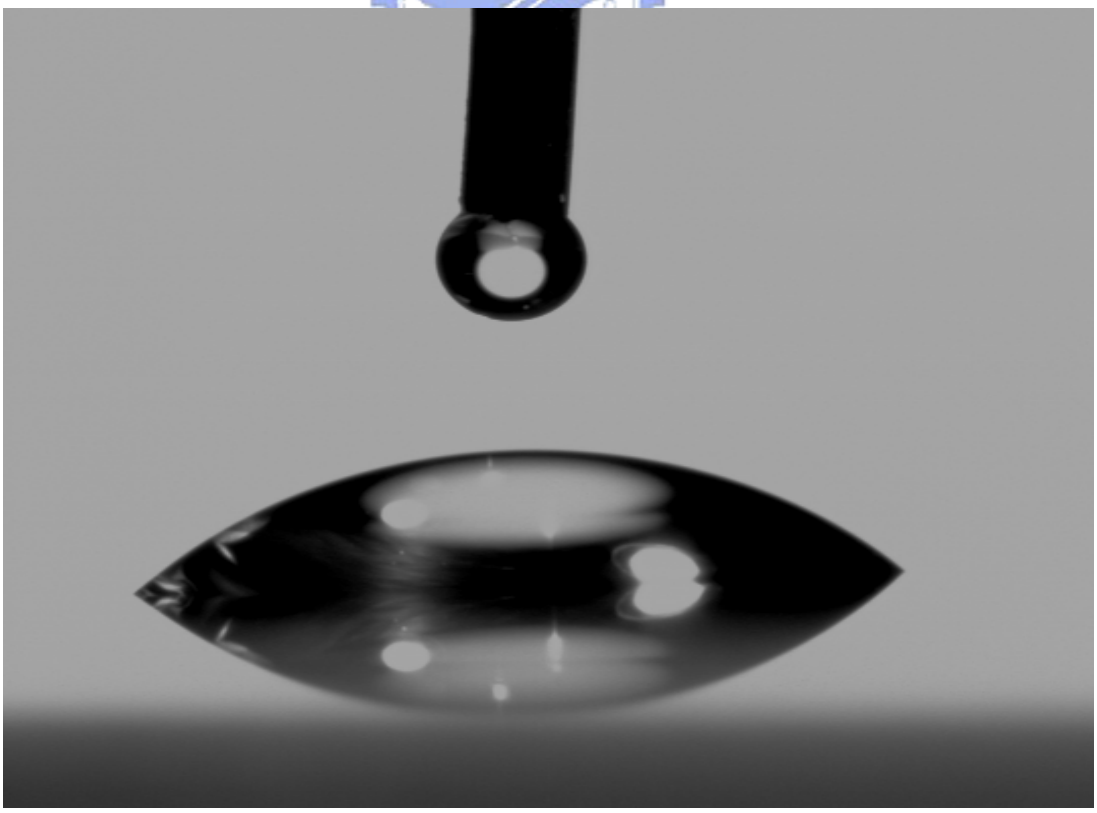

Figure 1-5 Image from a video contact angle device which water drops on glass.

In near years , the other people report about the change in water contact angle on

semiconductor oxides such as ZnO, Ta2O5, In2O3, InTaO4 or indium – tin oxides (ITO) and the unexpected response of some of them to irradiation with visible light. TiO2 has been used as a reference material. These oxides are known because they present some kind of photoactivity and have band gaps within the UV region of the spectrum. Except for ZnO, no results about hydrophilic adjustment of contact angles upon light irradiation have been reported for the other investigated oxides. Meanwhile, for InTaO4 it has been reported recently that this photoactive material doped with nickel is able to split the water into H2 and O2 when irradiated with visible light .

Wetting [30]

Wetting is the contact between a fluid and a surface, when the two are brought into contact. When a liquid has a high surface tension (strong internal bonds), it will form a droplet, whereas a liquid with low surface tension will spread out over a greater area (bonding to the surface). On the other hand, if a surface has a high surface energy (or surface tension), a drop will spread, or wet, the surface. If the surface has a low surface energy, a droplet will form. This phenomenon is a result of the minimization of interfacial energy. If the surface is high energy, it will want to be covered with a liquid because this interface will lower its energy, and so on.

The primary measurement to determine wettability is a contact angle measurement. This measures the angle between the surface and the surface of a liquid droplet on the surface. For example, a droplet would have a high contact angle, but a liquid spread on the surface would have a small one. The contact angle and the surface energies of the materials involved are related by the Young–Dupré equation

where is the surface tension between two substances and S, V, and L correspond to the solid, vapor, and liquid substances in a contact angle experiment respectively.

A contact angle of 90° or greater generally characterizes a surface as not-wettable, and one less than 90° means that the surface is wettable. In the context of water, a wettable surface may also be termed hydrophilic and a non-wettable

surface hydrophobic. Superhydrophobic surfaces have contact angles greater than 150°, showing almost no contact between the liquid drop and the surface. This is sometimes referred to as the "Lotus effect". This characteristic of spreading out over a greater area is sometimes called 'wetting action' when discussing solders and soldering.

Wetting is often an important factor in the bonding (adherence) of two materials. It is also the basis for capillary action, the ability of a narrow tube to draw a liquid, even against the force of gravity.

Hydrophile

Hydrophile, from the Greek (hydros) "water" and φιλια (philia) "friendship," refers to a physical property of a molecule that can transiently bond with water (H_2O) through hydrogen bonding. This is thermodynamically favorable, and makes these molecules soluble not only in water, but also in other polar solvents. There are hydrophillic and hydrophobic parts of the cell membrane.

A hydrophilic molecule or portion of a molecule is one that is typically charge-polarized and capable of hydrogen bonding, enabling it to dissolve more readily in water than in oil or other hydrophobic solvents. Hydrophilic and hydrophobic molecules are also known as polar molecules and nonpolar molecules, respectively.

Soap has a hydrophilic head and a hydrophobic tail which allows it to dissolve in both waters and oils, therefore allowing the soap to clean a surface.

Super hydrophilicity [32]

Under light irradiation, water dropped onto titanium dioxide forms no contact angle (almost 0 degrees). This effect, called super hydrophilicity, was discovered in 1995. Super hydrophilic material has various advantages. For example, it can defog glass, and it can also enable oil spots to be swept away easily with water. Such

materials are already commercialized as door mirrors for cars, coatings for buildings, etc.

Several mechanisms of this super hydrophilicity have been proposed by researchers. One is the change of the surface structure to a metastable structure, and another is cleaning the surface by the photodecomposition of dirt such as organic compounds adsorbed on the surface, after either of which water molecules can adsorb to the surface. The mechanism is still controversial, and it is too soon to decide which suggestion is correct. To decide, atomic scale measurements and other studies will be necessary.

1.4 Applications of TiO_2 [22] [23]

As a pigment of high refringence, titanium dioxide is the most widely used white pigment because of its brightness and very high refractive index (n=2.4), in which it is surpassed only by a few other materials. When deposited as a thin film, its refractive index and colour make it an excellent reflective optical coating for dielectric mirrors and some gemstones, for example "mystic fire topaz". TiO_2 is also an effective opacifier in powder form, where it is employed as a pigment to provide whiteness and opacity to products such as paints, coatings, plastics, papers, inks, foods, and most toothpastes. Used as a white food coloring, it has E number E171. In cosmetic and skin care products, titanium dioxide is used both as a pigment and a thickener. It is also used as a tattoo pigment and styptic pencils.

This pigment is used extensively in plastics and other applications for its UV resistant properties where it acts as a UV reflector.

In ceramic glazes titanium dioxide acts as an opacifier and seeds crystal formation. In almost every sunscreen with a physical blocker, titanium dioxide is

found both because of its refractive index and its resistance to discoloration under ultraviolet light. This advantage enhances its stability and ability to protect the skin from ultraviolet light.

Titanium oxide is also used as a semi-conductor.

Photocatalyst

Titanium dioxide, particularly in the anatase form, is a photocatalyst under ultraviolet light. Recently it has been found that titanium dioxide, when spiked with nitrogen ions, is also a photocatalyst under visible light. The strong oxidative potential of the positive holes oxidizes water to create hydroxyl radicals. It can also oxidize oxygen or organic materials directly. Titanium dioxide is thus added to paints, cements, windows, tiles, or other products for sterilizing, deodorizing and anti-fouling properties and is also used as a hydrolysis catalyst. It is also used in the Graetzel cell, a type of chemical solar cell.

Titanium dioxide has potential for use in energy production: as a photocatalyst, it can carry out hydrolysis, i.e., break water into hydrogen and oxygen. Were the hydrogen collected, it could be used as a fuel. The efficiency of this process can be greatly improved by doping the oxide with carbon, as described in "Carbon-doped titanium dioxide is an effective photocatalyst" .

As TiO_2 is exposed to UV light, it becomes increasingly hydrophilic; thus, it can be used for anti-fogging coatings or self-cleaning windows. TiO_2 incorporated into outdoor building materials can substantially reduce concentrations of airborne pollutants such as volatile organic compounds and nitrogen oxides.

1.5 Polyethylene Terephthalate [33]

1.5.1 Introduction

Polyethylene terephthalate (aka PET, PETE or the obsolete PETP or PET-P) is a thermoplastic polymer resin of the polyester family that produced by the chemical industry and is used in synthetic fibers; beverage, food and other liquid containers; thermoforming applications; and engineering resins often in combination with glass fiber. It is one of the most important raw materials used in man-made fibers.

Depending on its processing and thermal history, it may exist both as an amorphous (transparent) and as a semi-crystalline (opaque and white) material. Its monomer can be synthesized by the esterification reaction between terephthalic acid and ethylene glycol with water as a byproduct or the transesterification reaction between ethylene glycol and dimethyl terephthalate with methanol as a byproduct. Polymerization is through a polycondensation reaction of the monomers (done immediately after esterification/transesterification) with ethylene glycol as the byproduct (the ethylene glycol is recycled in production).

The majority of the world's PET production is for synthetic fibers (in excess of 60%) with bottle production accounting for around 30% of global demand. In discussing textile applications, PET is generally referred to as simply "polyester" while "PET" is used most often to refer to packaging applications.

Chemical structure :

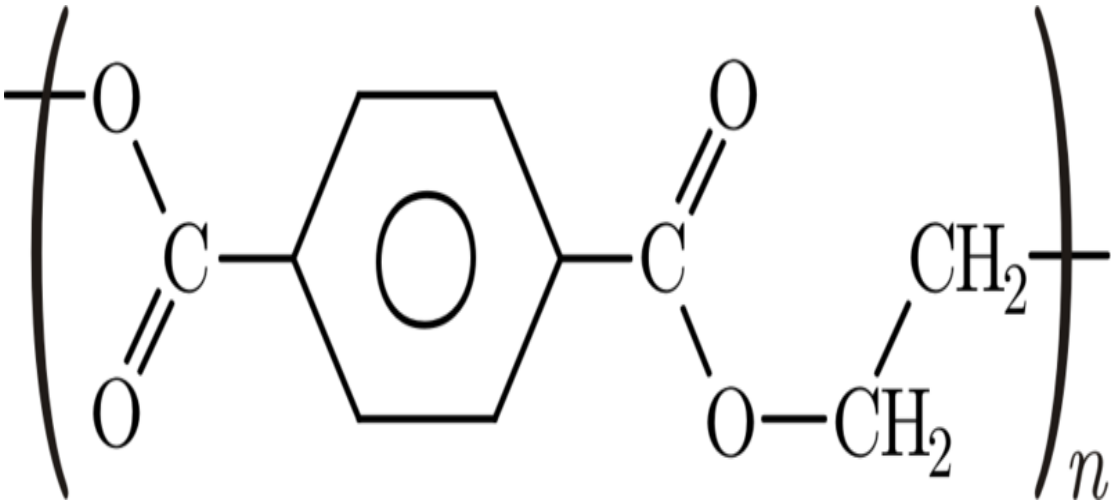

Figure 1-6 Chemical structure of polyethylene terephthalate.

Light absorption spectrum :

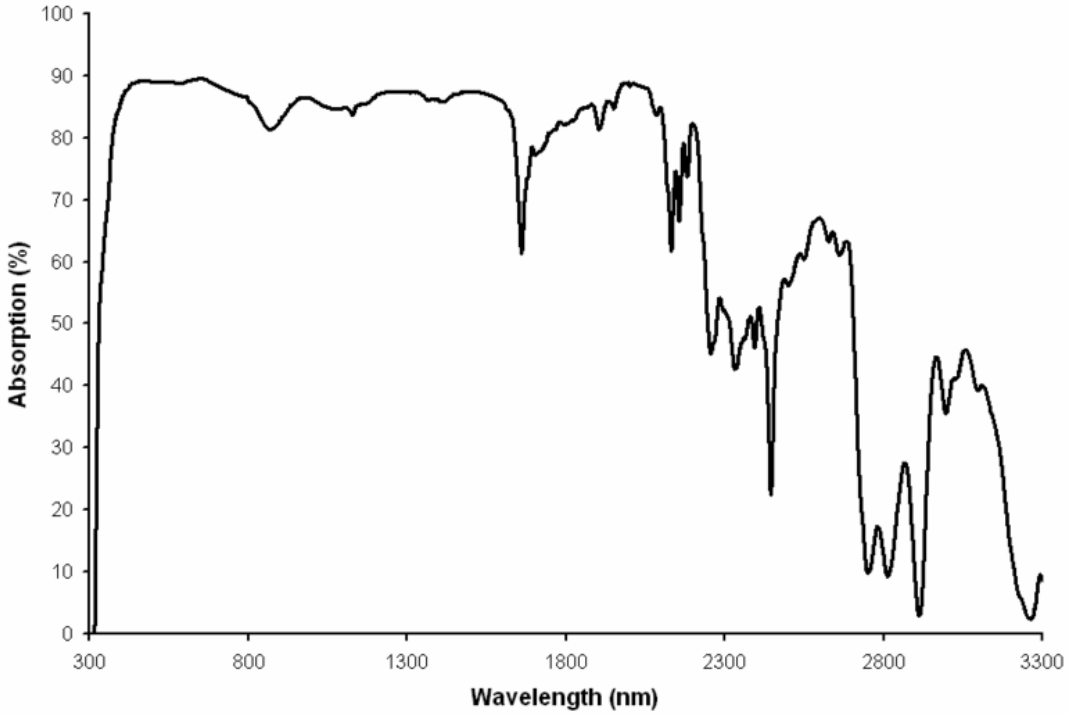

Figure 1-7 Light absortion spectrum of polyethylene terephthalate measured using a light spectrophotometer .

Table 1-1 Properties of PET.

[33]

PET	
Density	1370 kg/m^3
Young modulus(E)	2800 – 3100 MPa
Tensile strength(σ_t)	55 – 75 MPa
Elongation @ break	50 – 150%
notch test	3.6 kJ/m^2
Glass temperature	75 ˚C
melting point	260 ˚C
Vicat B	170 ˚C
Thermal conductivity	0.24 W/m.K
linear expansion coefficient (α)	7×10^{-5}/K
Specific heat (c)	1.0 kJ/kg.K
Water absorption (ASTM)	0.16
Price	0.5 – 1.25 €/kg

1.5.2 Crystals

Crystallization occurs when polymer chains fold up on themselves in a repeating, symmetrical pattern. Long polymer chains tend to become entangled on themselves, which prevents full crystallization in all but the most carefully controlled circumstances. PET is no exception to this rule; 60% crystallization is the upper limit for commercial products, with the exception of polyester fibers.

PET in its natural state is a crystalline resin. Clear products can be produced by rapidly cooling molten polymer to form an amorphous solid. Like glass, amorphous PET forms when its molecules are not given enough time to arrange themselves in an orderly fashion as the melt is cooled. At room temperature the molecules are frozen in place, but if enough heat energy is put back into them, they begin to move again, allowing crystals to nucleate and grow. This procedure is known as solid-state crystallization.

Like most materials, PET tends to produce many small crystallites when crystallized from an amorphous solid, rather than forming one large single crystal. Light tends to scatter as it crosses the boundaries between crystallites and the amorphous regions between them. This scattering means that crystalline PET is opaque and white in most cases. Fiber drawing is among the few industrial processes that produces a nearly single-crystal product.

1.5.3 Applications

PET can be semi-rigid to rigid, depending on its thickness, and is very lightweight. It makes a good gas and fair moisture barrier, as well as a good barrier to alcohol (requires additional "Barrier" treatment) and solvents. It is strong and impact-resistant. It is naturally colorless and transparent.

When produced as a thin film (often known by the tradename Mylar), PET is often

coated with aluminium to reduce its permeability, and to make it reflective and opaque. PET bottles are excellent barrier materials and are widely used for soft drinks, (see carbonation). PET or Dacron is also used as a thermal insulation layer on the outside of the International Space Station as seen in an episode of Modern Marvels "Sub Zero". For certain specialty bottles, PET sandwiches an additional polyvinyl alcohol to further reduce its oxygen permeability.

When filled with glass particles or fibers, it becomes significantly stiffer and more durable. This glass-filled plastic, in a semi-crystalline formulation, is sold under the tradename Rynite.

While all thermoplastics are technically recyclable, PET bottle recycling is more practical than many other plastic applications. The primary reason is that plastic carbonated soft drink bottles and water bottles are almost exclusively PET which makes them more easily identifiable in a recycle stream. PET has a resin identification code of 1. PET, as with many plastics, is also an excellent candidate for thermal recycling (incineration) as it is composed of carbon, hydrogen and oxygen with only trace amounts of catalyst elements (no sulfur) and has the energy content of soft coal.

PET was patented in 1941 by the Calico Printers' Association of Manchester. The PET bottle was patented in 1973.

1.6 Review

1.6.1 XRD patterns of N-doped TiO_2

X-ray diffraction patterns of the N-doped TiO_2 films deposited with NH_3 flow rate of 150 sccm before and after annealing are shown in Fig. 1-8. The as-grown film does not show any diffraction peaks. After annealing, the crystalline phase of anatase is found in the 400°C annealed film, both anatase and rutile phases in the 600°C annealed film, and the rutile phase in the 900°C annealed film, respectively. Similar results are obtained in the films deposited by changing NH_3 flow rate. In the undoped TiO_2 films, only anatase phase is observed after 600°C annealing. Because the intermingled structure of anatase and rutile phases is formed in the N-doped TiO_2 films annealed at 600°C, it is found that the transition temperature from anatase to rutile becomes lower by nitrogen doping [11]. To evaluate the effect of UV-visible absorption performance on photocatalytic activity of the nanoparticles, UV-visible absorption spectra of anatase and rutile TiO_2 nanoparticles in water were measured in Fig. 1-9. Clearly, absorption and scattering of anatase TiO_2 nanoparticles are stronger than those of rutile TiO_2, which guarantees the relatively high photocatalytic activity of the former [17].

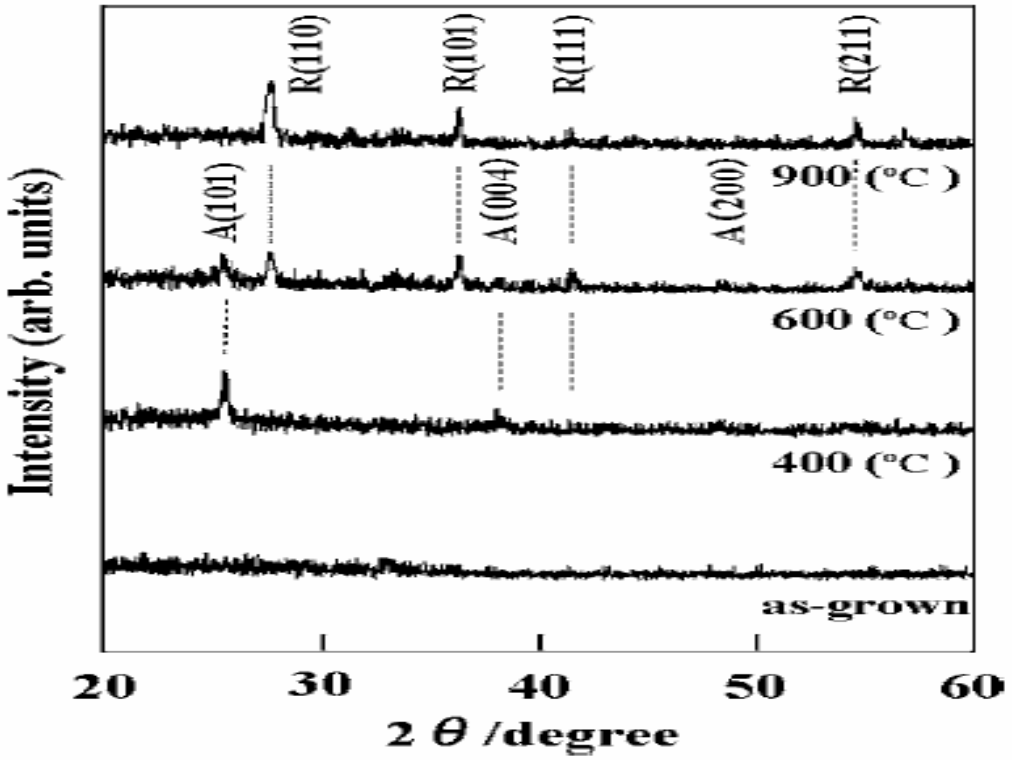

Figure 1-8 XRD patterns of N-doped TiO_2 films deposited with NH_3 flow rate of 150 sccm before and after annealing.

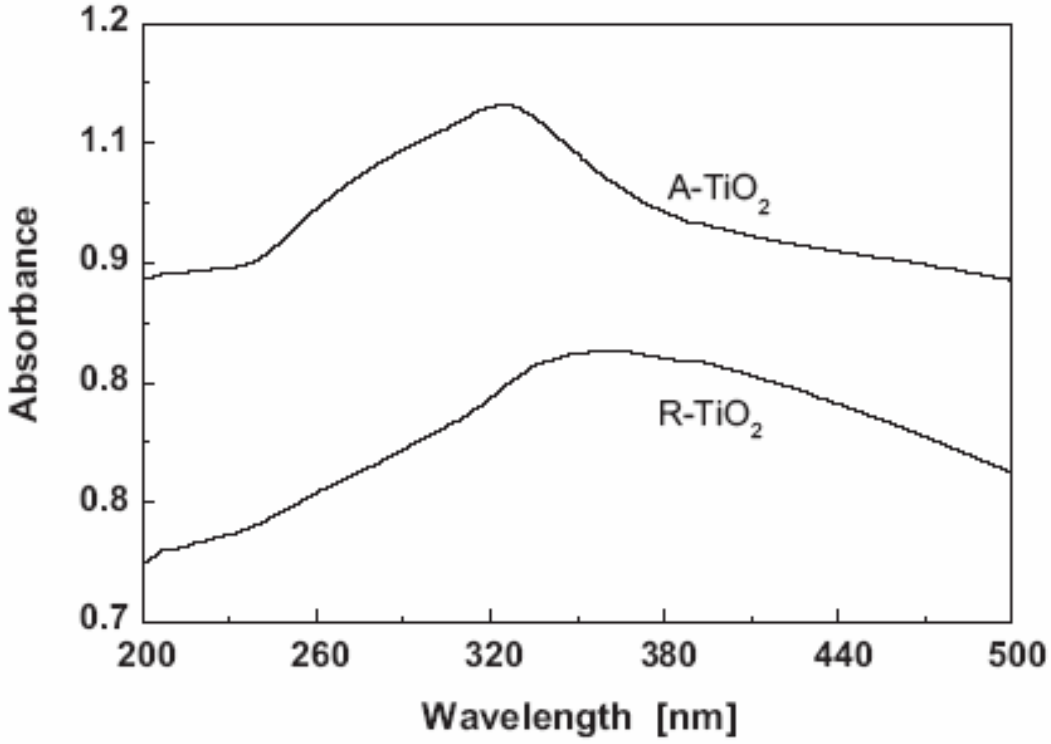

Figure 1-9 UV-visible absorption spectra of anatase and rutile TiO_2 nanoparticles in water.

1.6.2 XPS patterns of N-doped TiO_2

Fig. 1-10 shows the N 1s XPS spectra of $TiO_{2-x}N_x$ and TiO_2 powders. Since peaks at 396 eV, which have previously been found to result from Ti-N bonds, are observed for the powders annealed under NH3, it was determined that the oxygen sites were substituted by nitrogen atoms. Since the XRD did not indicate the formation of TiN bonds, it was determined that O-Ti-N bonds formed. Therefore, these powders were described as $TiO_{2-x}N_x$. In contrast, the air-annealed samples did not display a peak at 396 eV and is TiO_2. The peak around 400 eV is the chemisorbed N_2 molecule, which absorbs onto the surface. While the N 1 s X-ray photoelectron spectrum of $TiO_{2-x}N_x$ shown in Fig. 1-11 features a peak at 399.95 eV, known to be attributable to adsorbed NO or N in Ti-O-N, no weak peak attributable to Ti-N bonding can be seen at 396 eV due to the noise, as shown in the upper trace in Fig. 1-11. In the case of undoped TiO_2 powder, neither peak is observed, as shown in the lower trace in Fig. 1-11[13].

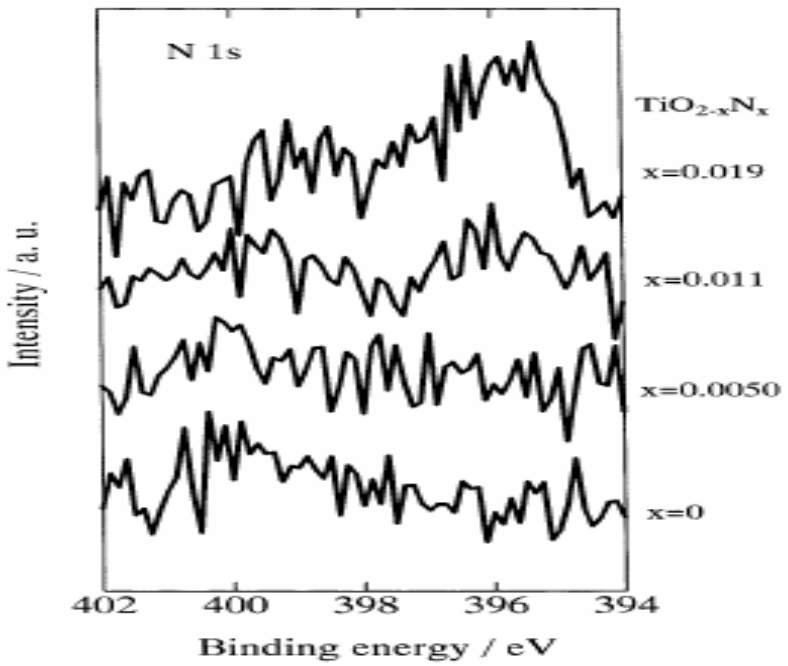

Figure 1-10 N 1s XPS spectra of $TiO_{2-x}N_x$ and TiO_2 powders.

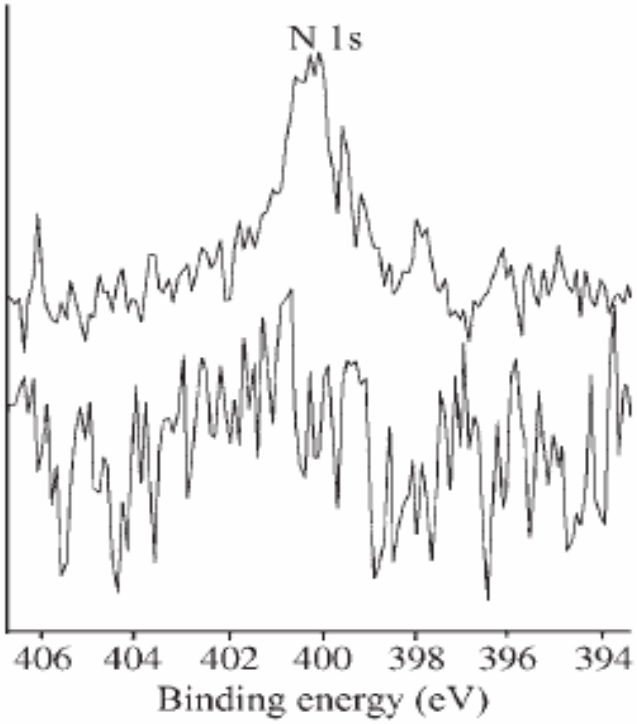

Figure 1-11 N 1 s X-ray photoelectron spectra of $TiO_{2-x}N_x$ (upper trace) and TiO_2 powders (lower trace).

XPS spectra of the N-doped TiO_2 film deposited with NH_3 flow rate of 150 sccm are shown in Fig. 1-12 for Ti 2p, b for O 1s, and c for N 1s electrons, respectively. The binding energy of Ti 2p at 459.1 eV shifting from 454 eV of metallic Ti is the signal of Ti in TiO_2, and that of O 1s at 531 eV is assigned to metallic oxide. For N 1s electrons, two bonding states of nitrogen atoms are observed whose binding energies are 396.1 and 399.3 eV, and these are assigned to the nitrogen atoms substituting for the oxygen atoms (N_{sub}) and those existing interstitially in the TiO_2 matrices (N_{int}), respectively. N_{sub}:N_{int} ratio estimated from the spectrum intensities becomes about 80:20 [11].

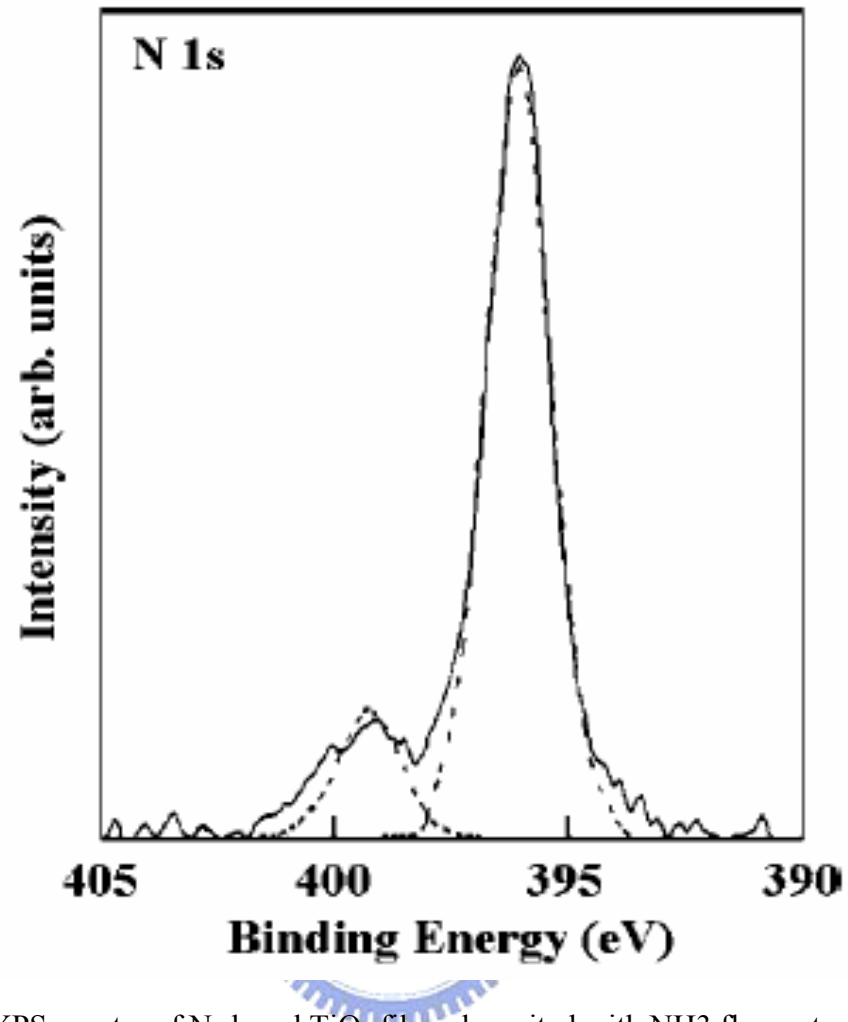

Figure 1-12 XPS spectra of N-doped TiO_2 films deposited with NH3 flow rate of 150 sccm: N 1s respectively.

1.6.3 Absorption and energy band gap

In the case of Si- $TiO_{2-x}N_x$ films, the crystalline forms before and after doping with nitrogen were characterized as being of anatase-type, with a crystalline size of 11 nm. Fig. 1-13(A) shows a comparison of the UV/Vis diffuse reflectance spectra of $TiO_{2-x}N_x$ and undoped TiO2. The prepared $TiO_{2-x}N_x$ photocatalysts, in the form of powders or thin films, were very vivid yellow in color, and showed a shift to longer wavelengths in accordance with color. Fig. 1-13(B) shows plots of the modified Kubelka—Munk function versus the photon energy, from which the band-gap energies can be obtained. The band-gap energy for $TiO_{2-x}N_x$ can be seen to be 2.95 eV,

corresponding to the visible-light region, whereas that for undoped TiO2 is 3.2 eV.

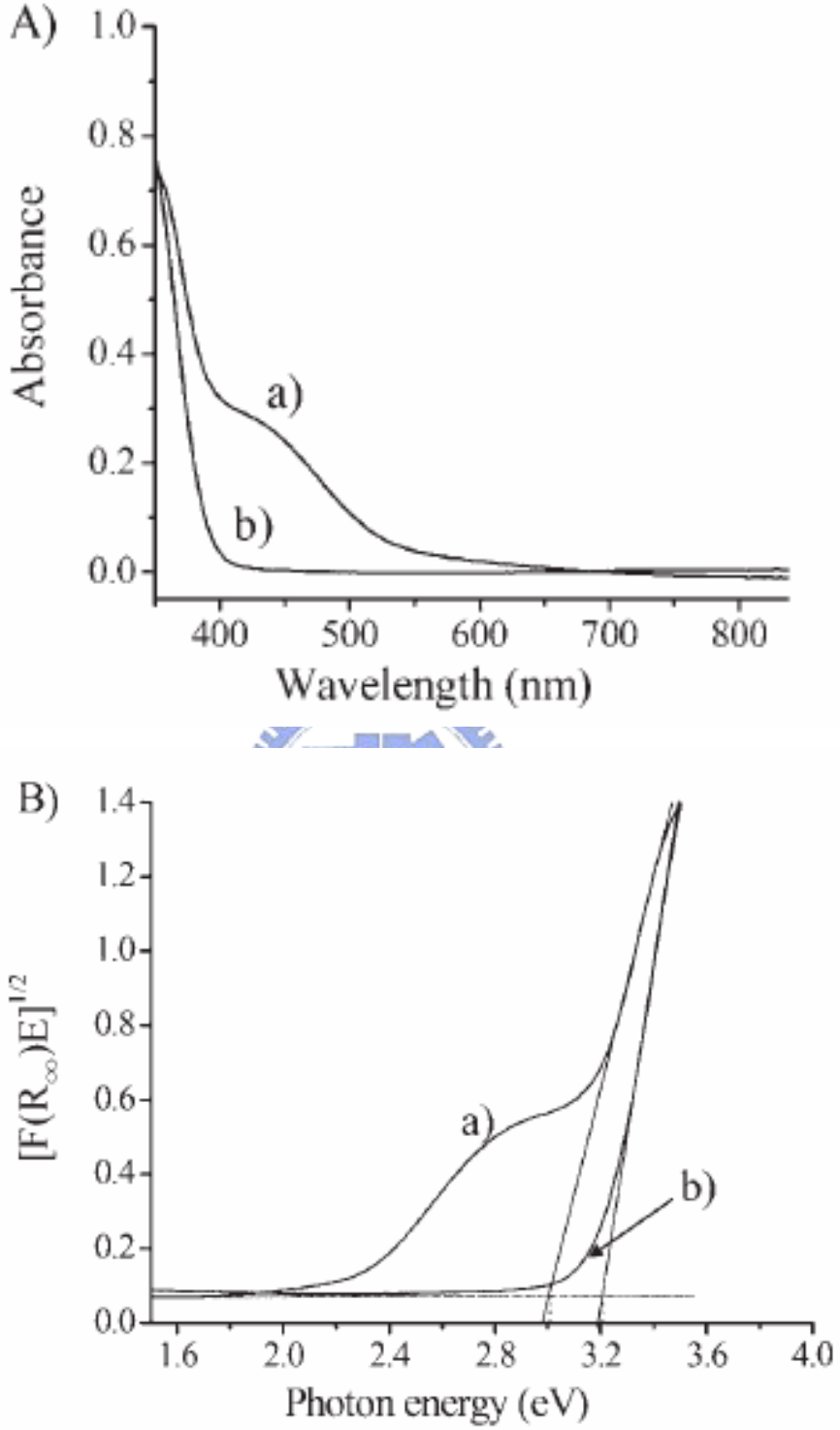

Figure 1-13. A): UV/Vis diffuse reflectance spectra of the samples. B): Plot of the modified Kubelka – Munk function versus the photon energy of the samples. (a) After doping with nitrogen. (b) Commercial UV photocatalyst. Doping conditions: 10 min at 873 K under a stream of ammonia gas.

Fig. 1-14(a) shows the band-gap energy structure of the anatase-type UV-driven photocatalyst, while Fig. 1-14(b), reported by Asahi et al., shows the narrowed band-gap structure obtained by mixing of N 2p and O 2p orbit. Fig. 1-14(c), reported by Nakamura et al., shows the midgap energy level formed slightly above the valence band. The schemes represented in Figure 1-14(b) and (c) are both used in engineering for visible-light-driven photocatalyst materials. Mechanisms to achieve responsiveness to visible light are still under investigation, and no complete interpretation has yet been formulated. Thus, the mechanisms of reactions of specific compounds with $TiO_{2-x}N_x$ may help in delineating the mechanistic aspects of reactivity in the visible-light region [13].

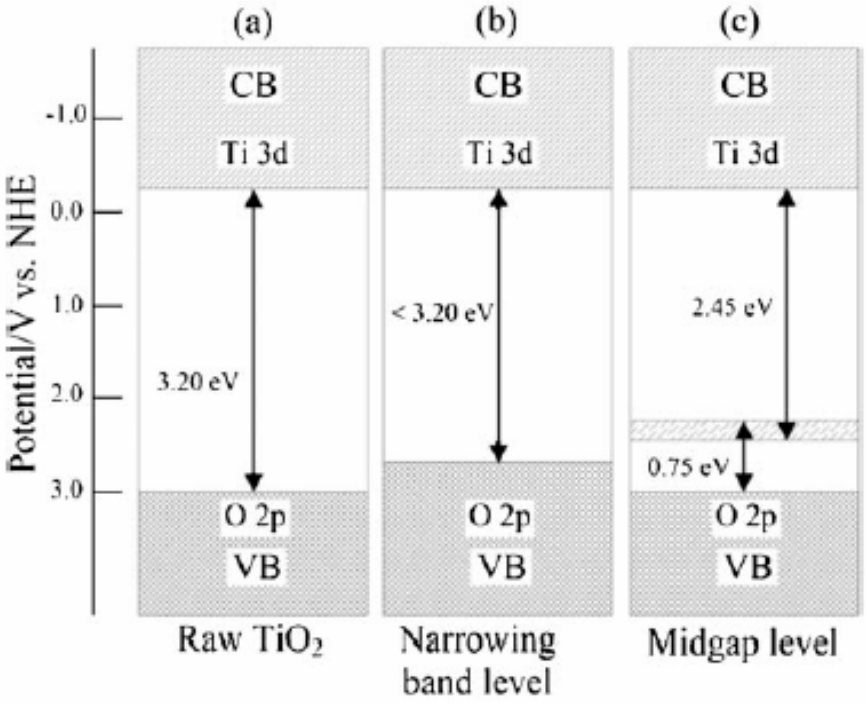

Figure 1-14. Models of the energy band gap structure of $TiO_{2-x}N_x$ for response in the visible-light region.

1.6.4 Water contact angle

Photo-induced hydrophilicity after the visible-light irradiation was evaluated by measuring the contact angle of water on the film surface. The contact angle of

as-grown and annealed N-doped TiO_2 films deposited using NH_3 flow rates of 150 sccm as a function of visible-light irradiation time is shown in Fig. 1-15. It is found that weak photo-induced hydrophilicity for visible-light irradiation is observed even in the as-grown film. The photo-induced hydrophilicity enhances remarkably when the film is annealed. Higher photo-induced hydrophilicity is also observed in the film with intermingled structure of anatase and rutile [11]. All of these experiments heat the substrate for a high temperature.

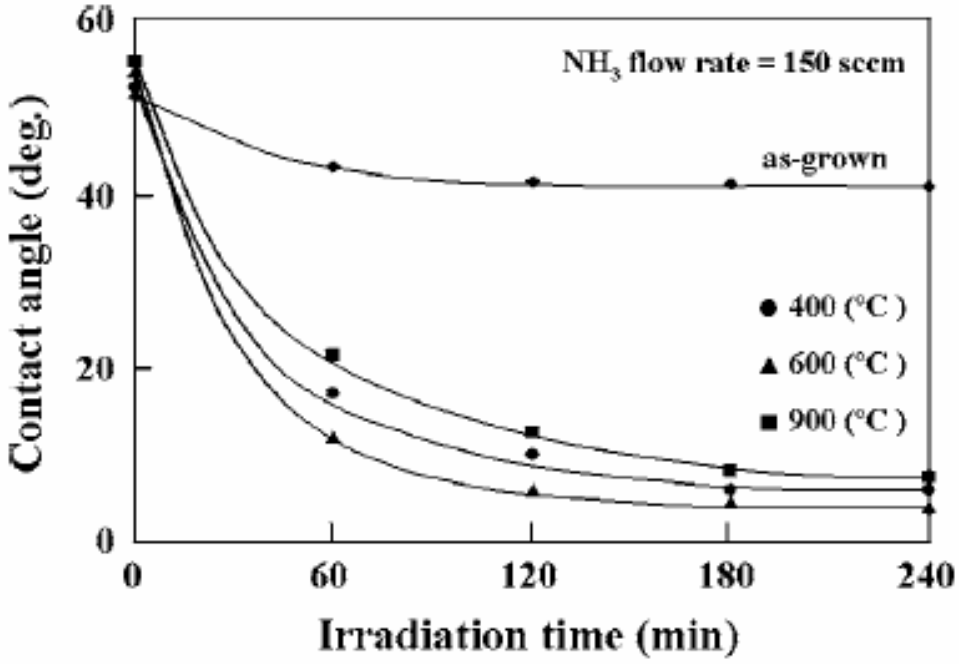

Figure 1-15. Water contact angle of N-doped TiO_2 films as a function of visible- or UV-light irradiation time.

Chapter 2 Experiment Details

2.1 System of Radio-Frequency Magnetron Sputter

Sputtering system has been widely used to deposit various metal films in ULSI fabrication, and it was also used to deposit dielectrics because of its easy-control and low cost. In the experiment, the thin films were deposited by a single target radio-frequency (RF) magnetron sputtering system. The sputtering system is composed of several parts including

(a) Gas flow controlling system: In general, the percentage of oxygen in the sputtering atmosphere played an important role in oxide ceramics. We used Gas MFC (mass flow meter) to control the flow rate and atmosphere contents during the sputtering process. So we could find out that the dependence of the mass ratio for the device performance by tuning recipe

(b) Mechanical modules: vacuum chamber, targets, and shutter. In addition, a DC motor to let the thin films grow uniformly controlled the rotational substrate holder.

(c) Vacuum pump modules: a diffusion pump (high vacuum pump) and one mechanical pump (low vacuum pump). The chamber base pressure was evacuated to 3×10^{-5} torr prior to the thin film deposition.

(d) RF power modules: the RF power generator (13.56 MHz) was controlled by a RF power supply with an automatic matching network, which can be tuned to minimum reflected power.

(e) Pressure modules: pressure gauges, exhaust valves, gas supply, and mass flow controllers. Pure gas was introduced by mass flow controllers after the system was evacuated to base pressure. Pressure modules and vacuum pump modules control the working pressure.

(f) Cooling system: There was cooling water that flows in the pipe welded on the chamber and in the magnetron gun. During the sputtering process, the heating lamps and plasma always produced a lot of redundant heat energy in the chamber. We needed cooling water to prevent from mechanical breakdown and maintain the sample uniformity.

2.2 Thin Films Preparation by Sputter

TiO_2 films were deposited on PET substrates by RF(13.56 MHz) sputtering method without heating. The sputtered target was TiN (2 inches) with a purity of 99.999%, the distance between the target and the substrate was about 30 mm. The sputtering and reactive gas was a mixture of oxygen and nitrogen with a partial pressure ratio of 0.5: 0.5, 0.2: 0.7, 0.0:1.0. The base pressure of the sputtering chamber was 3×10^{-5} torr, and the sputtering pressure was about 1.5×10^{-2} torr during the deposition, and the sputtering power was 20W~120W in Fig. 2-1.

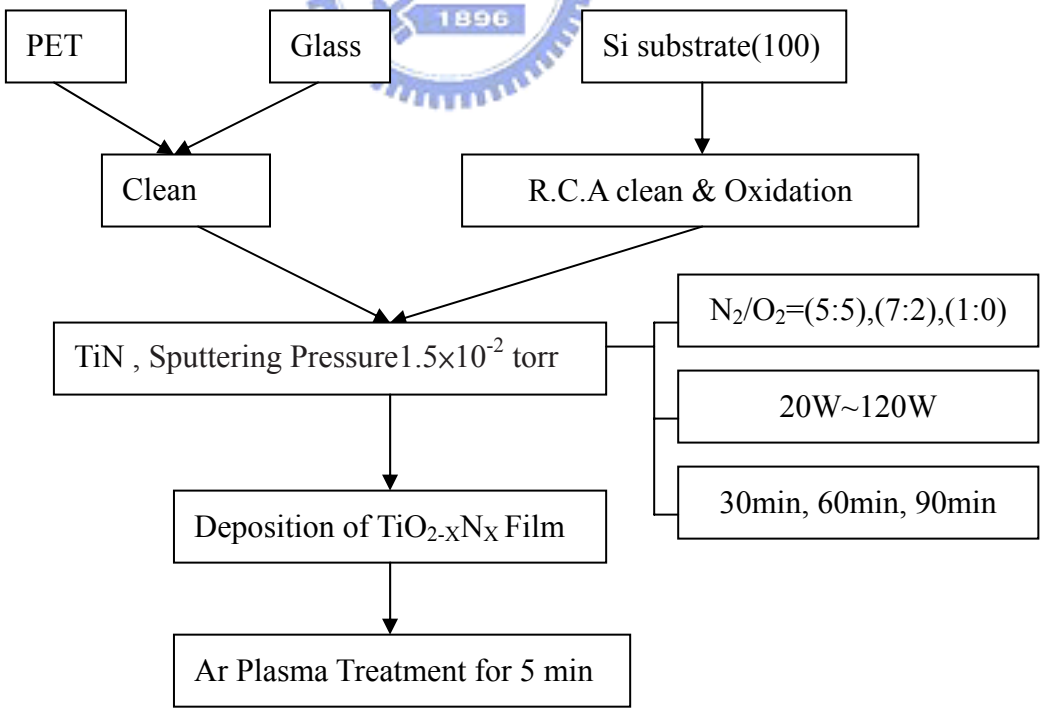

Figure 2-1 The illustration of our solution for $TiO_{2-X}N_X$ preparation flow

2.3 The process of experiment

In our experiment, it can be sorted into sample preparation, optical property analysis, and material analysis, as Fig. 2-2.

There are many aspects of our sample analysis. In the side of material analysis, the microstructure and crystallization analysis, that is realized by the scanning electron microscope system (SEM), X-ray Photoelectron Spectroscopy (XPS), Raman Spectroscopy, the atomic force microscopy (AFM), and the X-ray diffraction system (XRD). In the side of optical property analysis, the photo-induced surface wettability conversion reaction of the thin films was investigated by water contact angle measurement, and the absorbance of $TiO_{2-X}N_X$ thin films was measured by UV-VIS spectrophotometer.

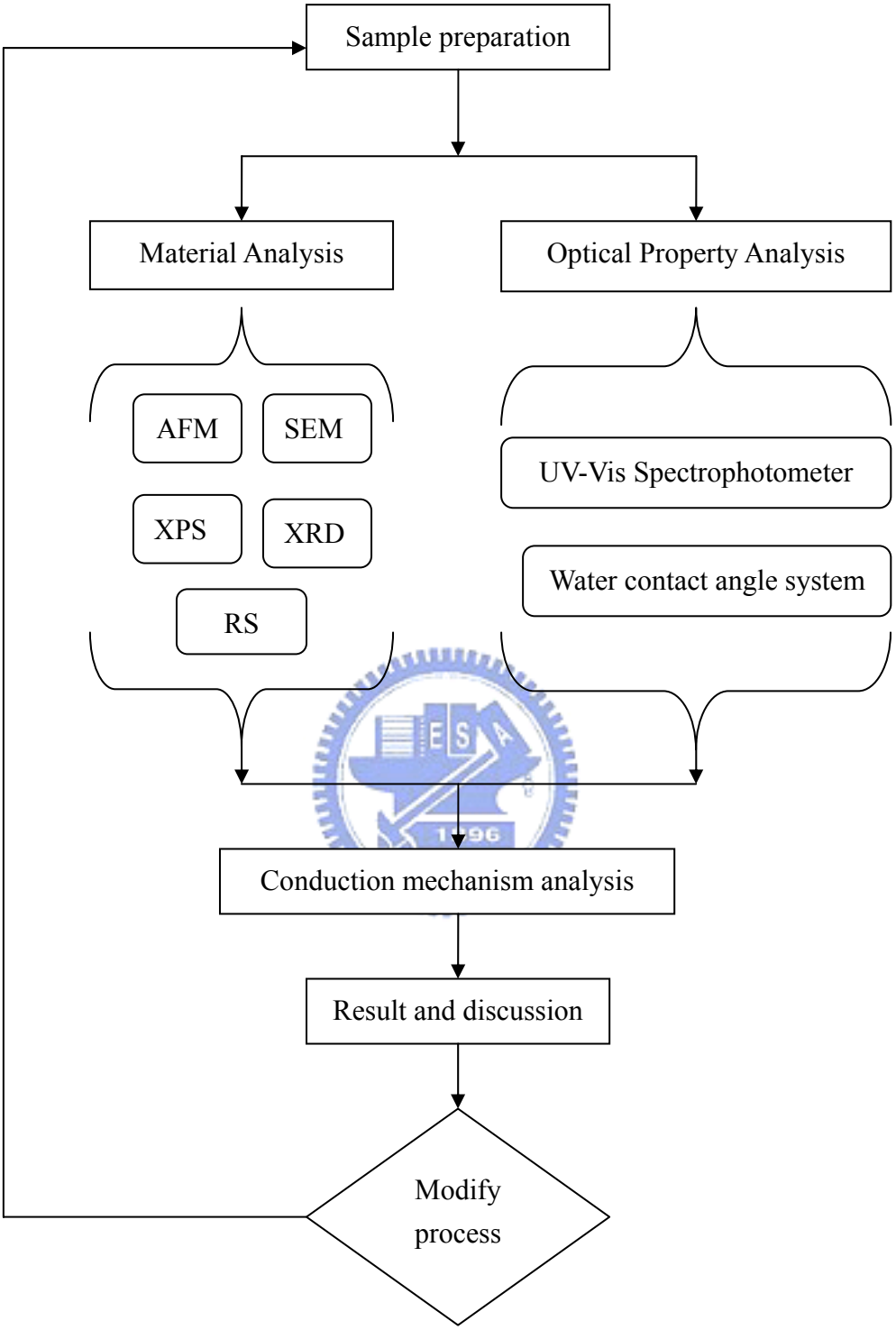

Figure 2-2 The illustration of our experiment flow

2.4 Measurements and Materials Analysis

2.4.1 X-Ray Diffraction (XRD)

The crystal structure of the $TiO_{2-x}N_x$ was observed by the X-ray diffraction (XRD, MAC Science, MXP18, Japan). X-ray diffraction (XRD) was the equipment used for identifying the crystal structure, but the thin film of $TiO_{2-x}N_x$ is too thin .If the included angle θ (Bragg's angle) between the crystal plane and the incident light matched the Bragg's law ($n\lambda=2d\sin\theta$) , the incident light was diffracted by the crystal plane .By using Bragg's law for diffraction , the reflected x-rays from the respective atomic planes can be measured by the detector .In the Bragg's law ($n\lambda=2d\sin\theta$) , nλ is an integral number of wavelengths , and d is the distance between two successive crystal planes .

The X-ray diffraction measurement with Cu Kα radiation (λ=1.5418 Å) was operated at 30KV and 20mA. In order to avoid the peak of silicon at about 70°, the angle 2θ of the measurement was from 20° to 60°. The sweeping rate was 4° per minute.

2.4.2 Scanning Probe Microscopy (SPM)

Scanning probe microscopy (SPM) is a branch of microscopy that forms images of surfaces using a physical probe that scans the specimen .An image of the surface is obtained by mechanically moving the probe in a raster scan of the specimen, line by line, and recording the probe-surface interaction as a function of position. SPM was founded with the invention of the scanning tunneling microscope in 1981.

Many scanning probe microscopes can image several interactions simultaneously. The manner of using these interactions to obtain an image is generally called a mode.

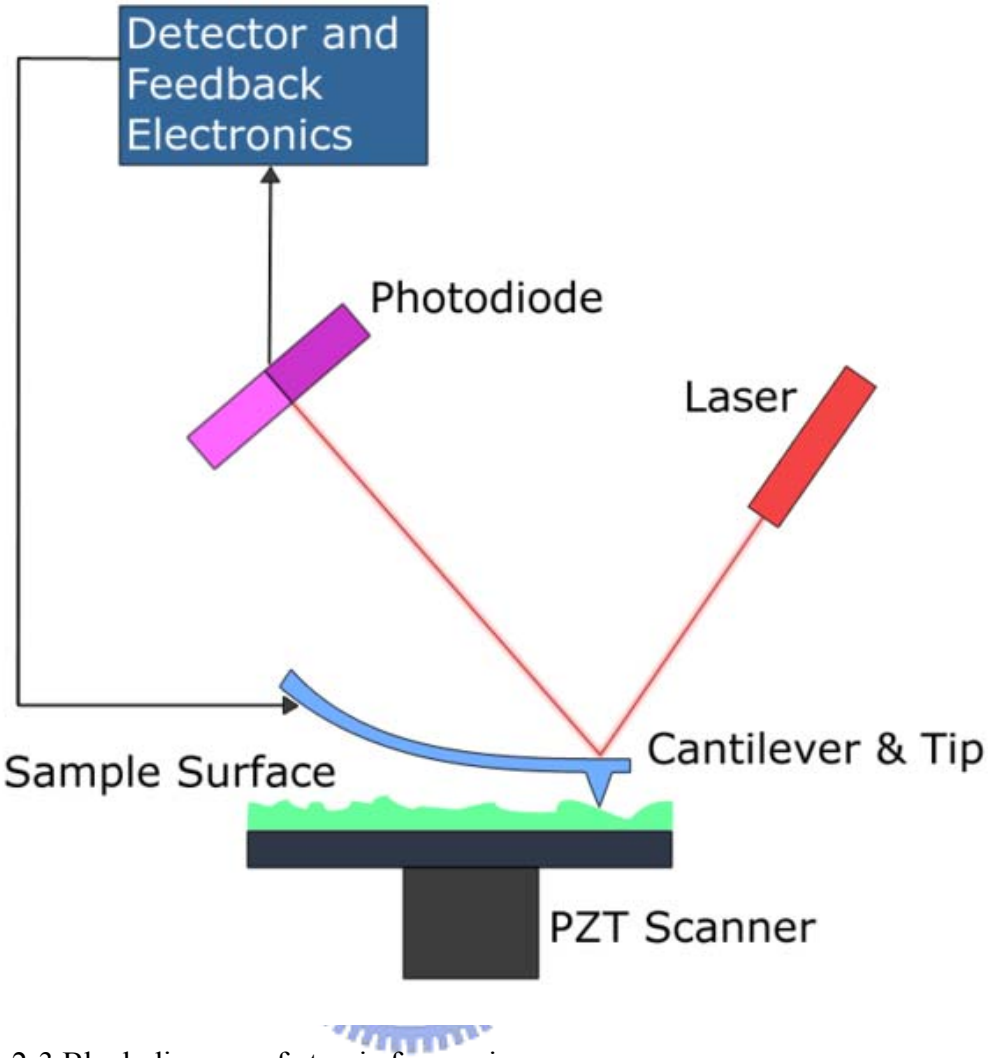

Figure 2-3 Block diagram of atomic force microscope.

Advantages of scanning probe microscopy

1. The resolution of the microscopes is not limited by diffraction, but only by the size of the probe-sample interaction volume (i.e., point spread function), which can be as small as a few Pico meter.
2. The interaction can be used to modify the sample to create small structures.

Disadvantages of scanning probe microscopy

1. The scanning techniques are generally slower in acquiring images, due to the scanning process. As a result, efforts are being made to greatly improve the scanning rate.

2. The maximum image size is generally smaller.

Table 2-1 Established types of scanning probe microscopy

1. AFM ● Contact AFM ● Non-contact AFM ● Dynamic contact AFM	Atomic force microscopy
2. EFM	Electrostatic force microscope
3. ESTM	Electrochemical scanning tunneling microscope
4. FMM	force modulation microscopy
5. KPFM	Kelvin probe force microscopy
6. MFM	Magnetic force microscopy
7. MRFM	Magnetic resonance force microscopy
8. NSOM	Near-field scanning optical microscopy (or SNOM, scanning near-field optical microscopy)
9. PSTM	Photon scanning tunneling microscopy
10. SECM	Scanning electrochemical microscopy
11. SCM	Scanning capacitance microscopy
12. SGM	Scanning gate microscopy
13. SICM	Scanning ion-conductance microscopy
14. SPSM	Spin polarized scanning tunneling microscopy
15. SThM	Scanning thermal microscopy
16. STM	Scanning tunneling microscopy
17. SVM	Scanning voltage microscopy

2.4.3 Scanning Electron Microscopy (SEM)

The surface structural and morphology analysis of the $TiO_{2-x}N_x$ thin film was observed by field emission scanning electron microscopy (FE-SEM, Hitachi S-4700I, Japan). The measured pressure was at 2 x 10^{-6} Torr. The working voltage was 15K eV. The working current was 10μA.

Comprehensively, the surface morphology issue is also a quite important character compared with the character of bulk for the thin films. We could observe the surface micro-morphology and cross section of our sample by SEM. Besides, the

crystallization of the thin films needed to be investigated directly by XRD analysis. So, we could get enough information to support our illustration. The SEM model is S4700I with high resolution of 15 Å made by Hitachi.

2.4.4 X-ray Photoelectron Spectroscopy (XPS)

The X-ray spectroscopy was used to characterize the binding energy and the composition of the $TiO_{2-x}N_x$ thin film. The electron binding energy is influenced by its chemical surroundings making binding energy suitable for determining chemical states. XPS is a surface-sensitive method because the emitted photoelectrons originate from the upper 0.5~5 nm of the sample, just as Auger electrons do, despite the deeper penetration of the primary X-rays compared to a primary electron beam.

2.4.5 Ultraviolet-Visible Spectrophotometers

Absorbance

In spectroscopy, the absorbance A is defined as

$$A_\lambda = \log_{10}(I_0/I)$$

where I is the intensity of light at a specified wavelength λ that has passed through a sample (transmitted light intensity) and I_0 is the intensity of the light before it enters the sample or incident light intensity. Absorbance measurements are often carried out in analytical chemistry, since the absorbance of a sample is proportional to the thickness of the sample and the concentration of the absorbing species in the sample, in contrast to the transmittance I / I_0 of a sample, which varies exponentially with thickness and concentration. See the Beer-Lambert law for a more complete discussion. The UV-VIS Spectrophotometer is made in Japan(Hitachi U3010, Japan).

2.4.6 Contact Angle System

This quantity examines the system and is different from other factories card only energy examine single some machine platforms which contact the angle. Full-automatic control, but quantity is examined small to the fragmentation, it is big to the glass base plate of 50×60cm. The quantity exposed to the angle examines not only has generally commonly used static mode, still have a advance mode and recede mode, can reflect that lie between the roughness of the interface. In addition, possess four load different polarity inject syringe of solution, can test for the surface free energy of block to appear to ask in time at the same time. This system can be used for being engaged in the following analysis**:** (1) Hydrophilic of the membrane and Hydrophobe of the membrane. (2) The surface free energy of membrane assessment. (3) Measuring static contact angle. (4) Measuring dynamic contact angle . (5) Measuring surface and interfacial tension. (6) Using for nano-material, polymer composite material, biomaterial, paint, coating, etc.

Figure 2-4 Image of contact angle goniometer system(KRŰSS GmbH, model GH-100).

2.4.7 Raman Spectroscopy(RS)

Raman spectroscopy is a spectroscopic technique used in condensed matter physics and chemistry to study vibrational, rotational, and other low-frequency modes in a system. It relies on inelastic scattering, or Raman scattering of monochromatic light, usually from a laser in the visible, near infrared, or near ultraviolet range. The laser light interacts with phonons or other excitations in the system, resulting in the energy of the laser photons being shifted up or down. The shift in energy gives information about the phonon modes in the system. Infrared spectroscopy yields similar, but complementary information.

Typically, a sample is illuminated with a laser beam. Light from the illuminated spot is collected with a lens and sent through a monochromator. Wavelengths close to the laser line (due to elastic Rayleigh scattering) are filtered out and those in a certain spectral window away from the laser line are dispersed onto a detector.

Spontaneous Raman scattering is typically very weak, and as a result the main difficulty of Raman spectroscopy is separating the weak inelastically scattered light from the intense Rayleigh scattered laser light. Raman spectrometers typically use holographic diffraction gratings and multiple dispersion stages to achieve a high degree of laser rejection. A photon-counting photo-multiplier tube (PMT) or, more commonly, a CCD camera is used to detect the Raman scattered light. In the past, PMTs were the detectors of choice for dispersive Raman setups, which resulted in long acquisition times. However, the recent uses of CCD detectors have made dispersive Raman spectral acquisition much more rapid.

Raman spectroscopy has a stimulated version, analogous to stimulated emission, called stimulated Raman scattering.

Chapter 3 Results and Discussion

3.1 Crystal of $TiO_{2-x}N_x$

$TiO_{2-x}N_x$ thin films were deposited on PET substrates by sputtering a TiN target under O_2, N_2, and Ar gas mixture. The thin films were deposited in plasma of argon, oxygen, and nitrogen with varying nitrogen content without heating temperature. XRD profiles of $TiO_{2-X}N_X$ thin film which conditions of power and treatment time are the same but the scales of treatment gas different are shown in Fig. 3-1. The deposition conditions used were oxygen flow rate of 0 to 7 sccm and nitrogen flow rate of 9 to 2 sccm, radio-frequency power of 100 W, and no substrate temperature. The as-grown film shows a peak which being indexed to the silicon substrate structure. Fig. 3-2 shows XRD profiles of the $TiO_{2-X}N_X$ thin film which conditions of treatment time and gas are the same but power different. The deposition conditions used were a nitrogen flow rate of 9 sccm, a RF power of 20 to 100 W, and no substrate temperature. The result is the same that shows a peak that have been indexed to the silicon substrate structure. However, we anneal those samples. After 500°C annealing, the crystalline phase of anatase is found in those annealed films. In Fig. 3-3 shows XRD profiles of the $TiO_{2-X}N_X$ thin film which conditions of power and treatment time are the same after 500°C annealing. Our $TiO_{2-X}N_X$ thin films that contain the anatase phase with the many peaks of (101) (004) (003) (200) are similar to the anatase powder samples and films reported in many other works. [11] [14] [21] [35] [36] In Fig. 3-4 also shows the anatase phase with the many peaks of (004) (003) are similar to the anatase powder samples and films. In order to be sure that our $TiO_{2-X}N_X$ thin film is anatase phase, we also have Raman profiles showing in Fig. 3-5. Our $TiO_{2-X}N_X$ thin films contain the anatase phase can be confirmed. Absorption and scattering of anatase TiO_2 nanoparticles are stronger than those of rutile TiO_2,

which guarantees the relatively high photocatalytic activity of the former. [17]

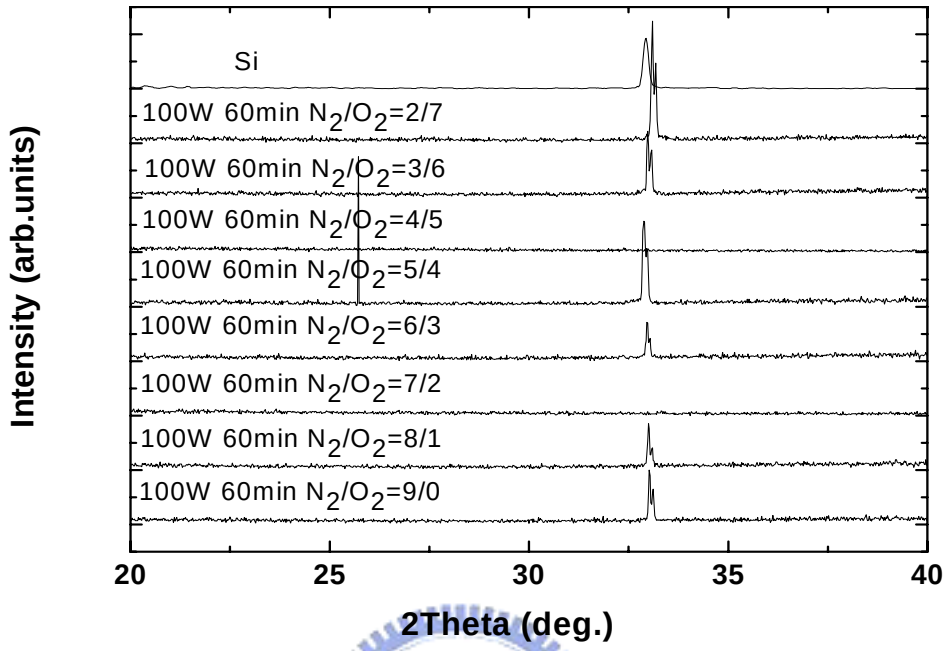

Figure 3-1. XRD profiles of the $TiO_{2-X}N_X$ thin film which conditions of power and treatment time are the same and no substrate temperature.

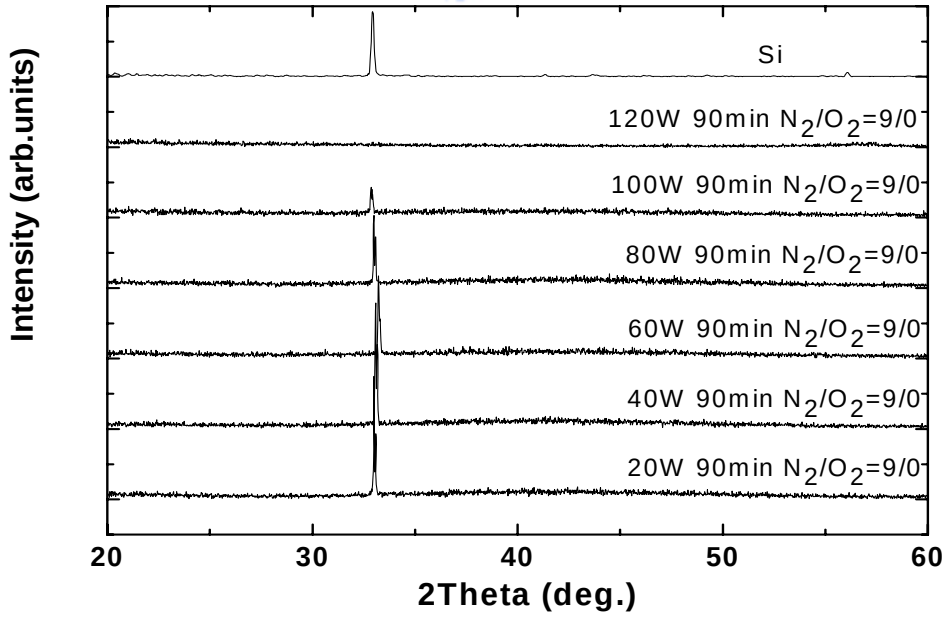

Figure 3-2. XRD profiles of the $TiO_{2-X}N_X$ thin film which conditions of treatment time and gas are the same and no substrate temperature.

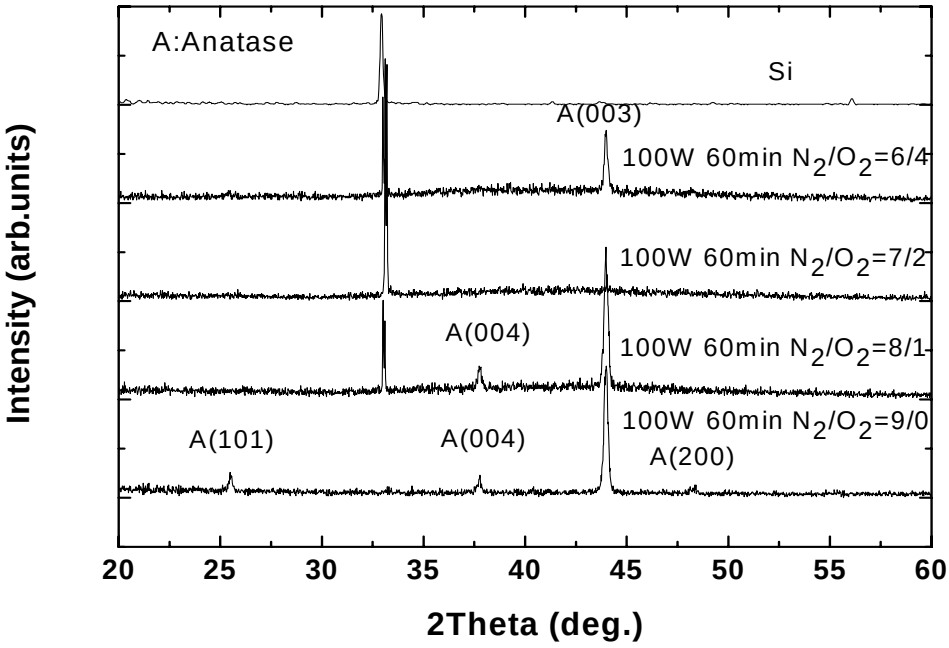

Figure 3-3. XRD profiles of the $TiO_{2-X}N_X$ thin film which conditions of power and treatment time are the same after 500°C annealing and no substrate temperature.

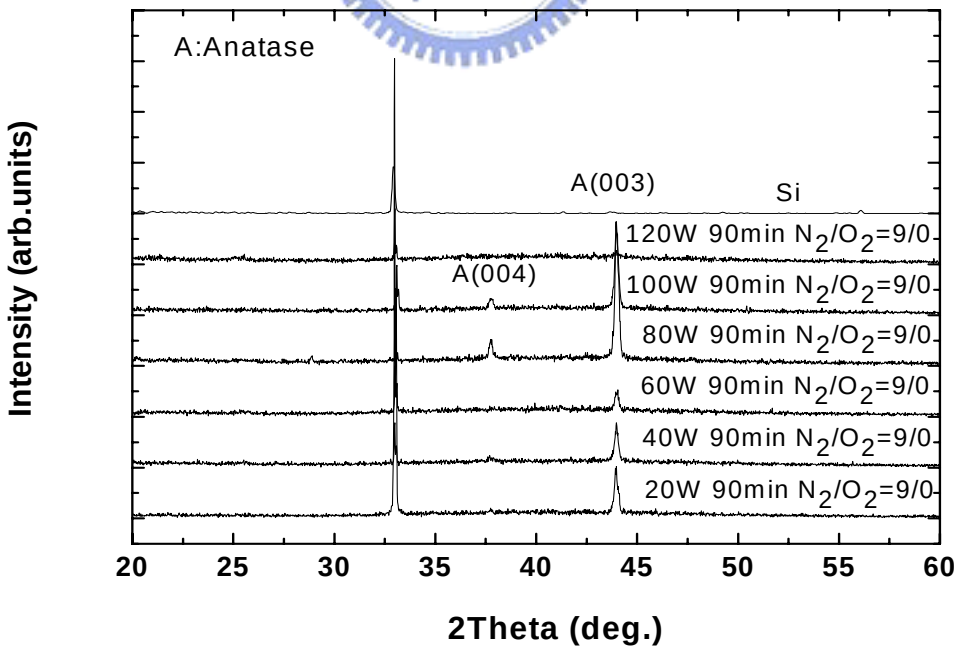

Figure 3-4. XRD profiles of the $TiO_{2-X}N_X$ thin film which conditions of treatment time and gas are the same after 500°C annealing and no substrate temperature.

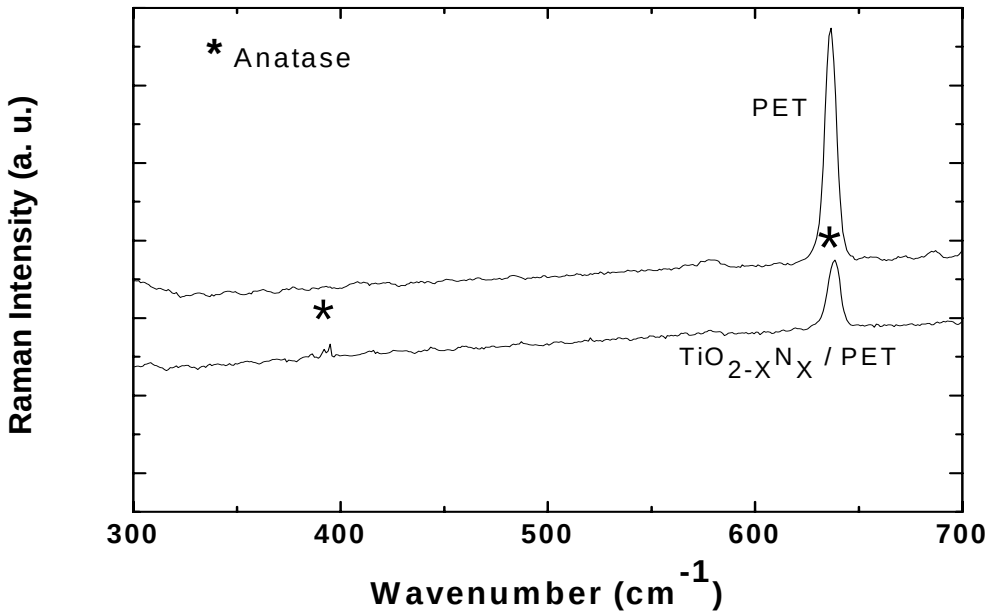

Figure 3-5. Raman profiles of the $TiO_{2-X}N_X$ thin film before annealing and no substrate temperature.

3.2 Composition of $TiO_{2-x}N_x$

$TiO_{2-x}N_x$ thin films were deposited on PET substrates by sputtering a TiN target under O_2, N_2, and Ar gas mixture. The thin films were deposited in plasma of argon, oxygen, and nitrogen with varying nitrogen content without heating temperature. XPS spectra of Ti 2p peaks of $TiO_{2-X}N_X$ thin film deposited by 100W power supply for 60min sputtering time and no substrate temperature. The deposition conditions used were oxygen flow rate of 0 to 7 sccm and nitrogen flow rate of 9 to 2 sccm. XPS spectra of Ti 2p peaks of $TiO_{2-X}N_X$ thin film deposited by 100W sputtering for 60min and no substrate temperature is shown in Fig. 3-6. Peaks for Ti $2p_{3/2}$ and Ti $2p_{1/2}$ observed at 458.1 eV and 464.3 eV are known to be due to Ti^{4+} in pure anatase titania form. The binding energy of Ti 2p at 458.1 eV shifting from 454 eV of metallic Ti is the signal of Ti in TiO_2, and that of O 1s at 529.9 eV is assigned to metallic oxide in Fig. 3-7. The peak of O 1s at 529.9 eV is derived from Ti-O bonds. XPS spectra of N 1s peaks of $TiO_{2-X}N_X$ thin film deposited by 100W sputtering for 60min and no substrate temperature is shown in Fig. 3-8. While the N 1 s X-ray photoelectron spectrum of $TiO_{2-X}N_X$ thin film shown in Fig. 3-8 features peaks at 399.6 eV , 403eV and 406.2eV[37], known to be attributable to adsorbed NO or N in Ti-O-N, no weak peak attributable to Ti-N bonding can be seen at 396 eV due to the noise [4] [13] [14] . For N 1s electrons, two bonding states of nitrogen atoms are observed whose binding energies are 396 and 399.6 eV, and these are assigned to the nitrogen atoms substituting for the oxygen atoms (N_{sub}) and those existing interstitially in the TiO_2 matrices (N_{int}), respectively [11]. So that we can confirm our bonding state of nitrogen atoms is interstitial. The composition of $TiO_{2-x}N_x$ thin films is shown in Table 3-1. While the deposition conditions used were a oxygen flow rate of 0 sccm and a nitrogen flow rate of 9 sccm, the percentage of nitrogen is 12.3%. While the deposition

conditions used were a oxygen flow rate of 2 sccm and a nitrogen flow rate of 7 sccm, the percentage of nitrogen is 8.2%. While the deposition conditions used were a oxygen flow rate of 4 sccm and a nitrogen flow rate of 5 sccm, the percentage of nitrogen is 5%.

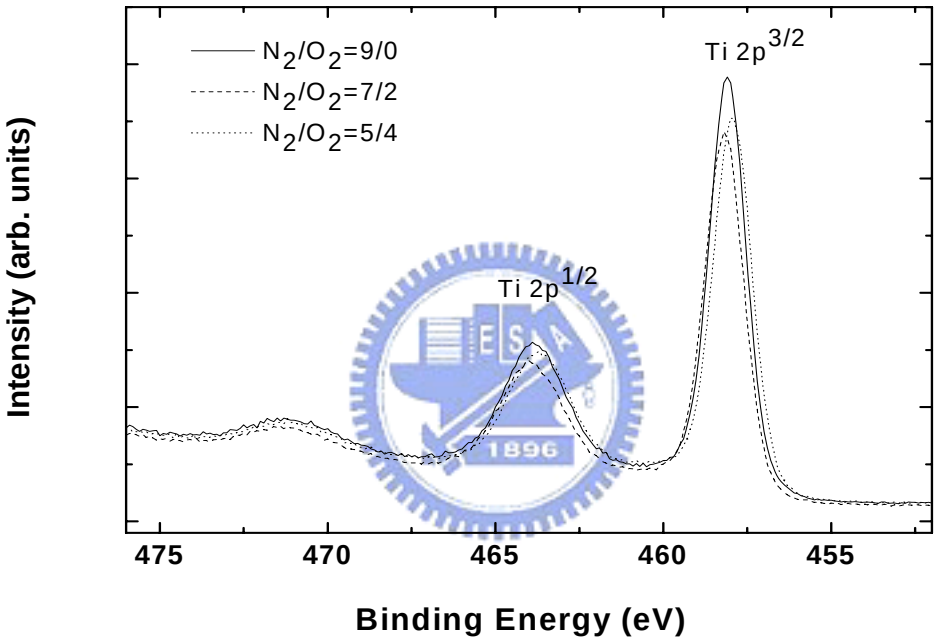

Figure 3-6. XPS spectra of Ti 2p peaks of the $TiO_{2-X}N_X$ thin film deposited by 100W power supply for 60min sputtering time and no substrate temperature.

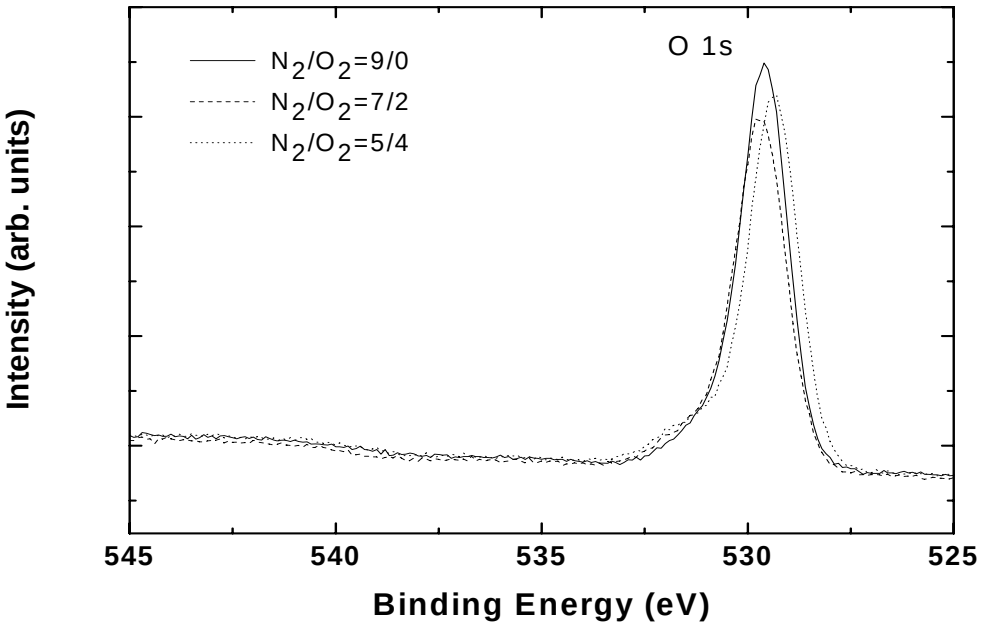

Figure 3-7. XPS spectra of O 1s peaks of the $TiO_{2-X}N_X$ thin film deposited by 100W power supply for 60min sputtering time and no substrate temperature.

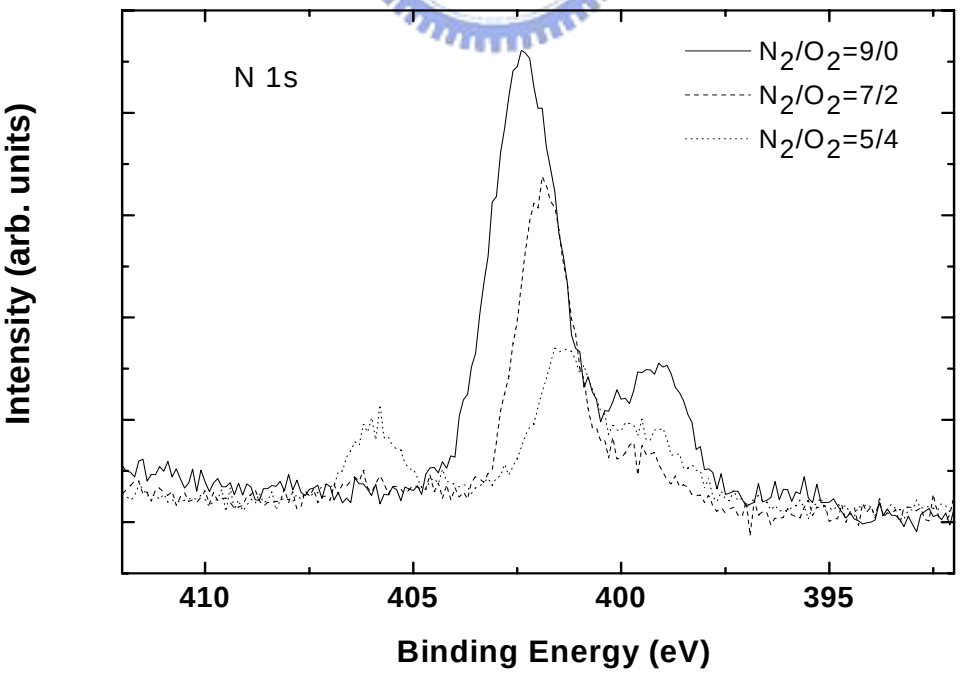

Figure 3-8. XPS spectra of N 1s peaks of the $TiO_{2-X}N_X$ thin film deposited by 100W power supply for 60min sputtering time and no substrate temperature.

Table 3-1. The composition of the $TiO_{2-x}N_x$ thin films with no substrate temperature

O_2/N_2 flowing ratios	N (at. %)	O (at. %)	Ti (at. %)
0/9	12.3	59.2	28.5
2/7	8.2	62.6	29.6
4/5	5.0	65.7	29.3

3.3 Thickness of Different Power

The thickness of the $TiO_{2-x}N_x$ thin film was observed by field emission scanning electron microscopy (FE-SEM, Hitachi S-4700I, Japan). $TiO_{2-x}N_x$ thin films were deposited on PET substrates by sputtering a TiN target under O_2 and N_2 mixture. The thin films were deposited in plasma of oxygen and nitrogen without heating temperature. The deposition conditions used were oxygen flow rate of 2 sccm and nitrogen flow rate of 7 sccm, radio-frequency power of 100 W, and no substrate temperature. The growth rate of the $TiO_{2-x}N_x$ thin film was shown in Table 3-2. The growth rate of 20W power is 0.43 nm/min. The growth rate of 40W power is 0.83 nm/min. The growth rate of 60W power is 1.18 nm/min. The growth rate of 80W power is 1.32 nm/min. The growth rate of 100W power is 1.93 nm/min. The growth rate of 120W power is 2.12 nm/min. All SEM images of the $TiO_{2-x}N_x$ thin film were shown in Fig. 3-9. In Fig. 3-9, SEM images of the $TiO_{2-x}N_x$ thin film deposited by 60min sputtering time and N_2/O_2=7/2 flow rate with (a) 20W (b) 40W power supply are shown. The $TiO_{2-x}N_x$ thin film is vary uniform and grain is vary small. In Fig. 3-12, SEM top view image of the $TiO_{2-x}N_x$ thin film is shown clearly.

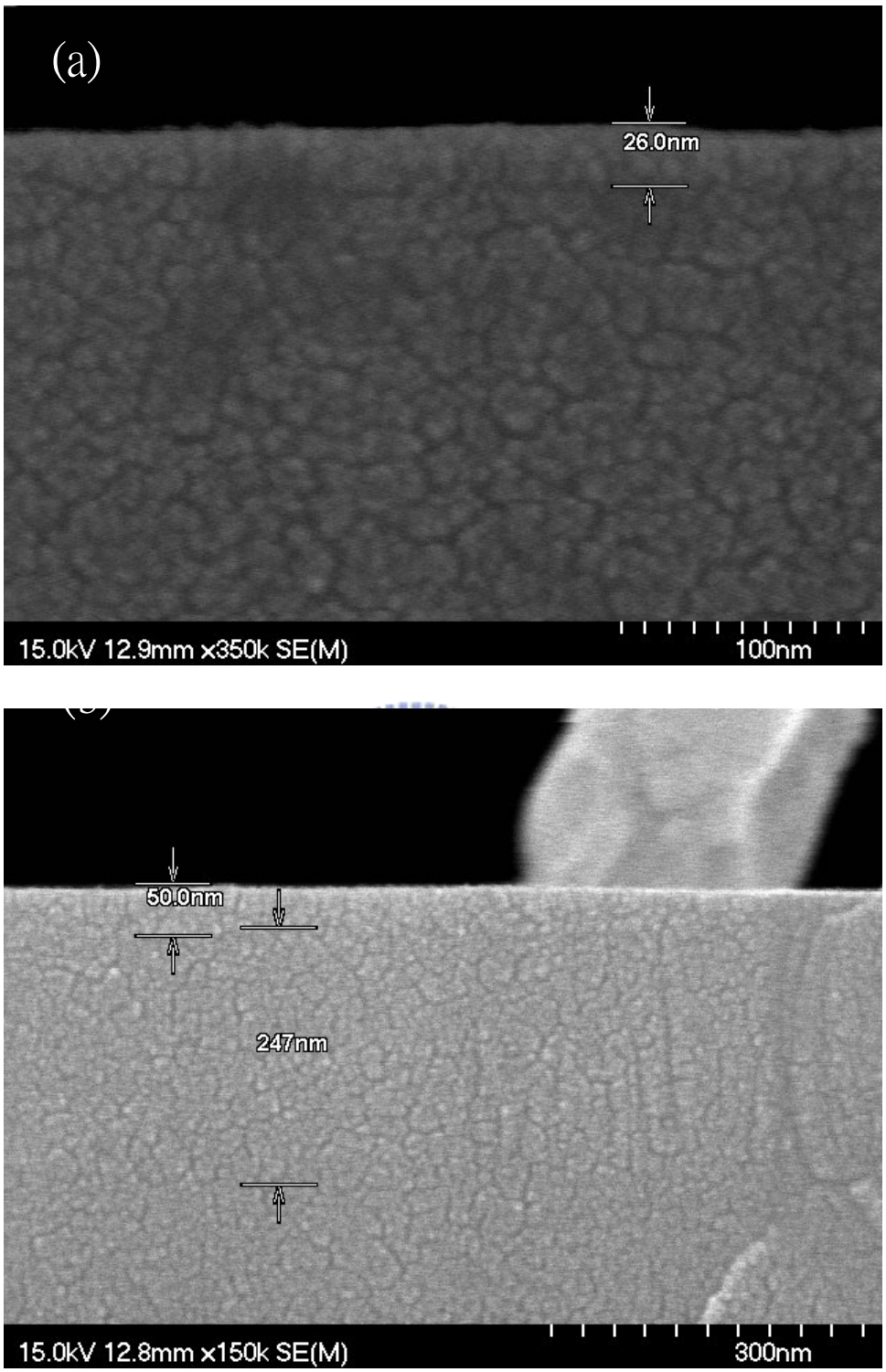

Figure 3-9. SEM images of the $TiO_{2-x}N_x$ thin film deposited by 60min sputtering time and N_2/O_2=7/2 flow rate with (a) 20W (b) 40W power supply.

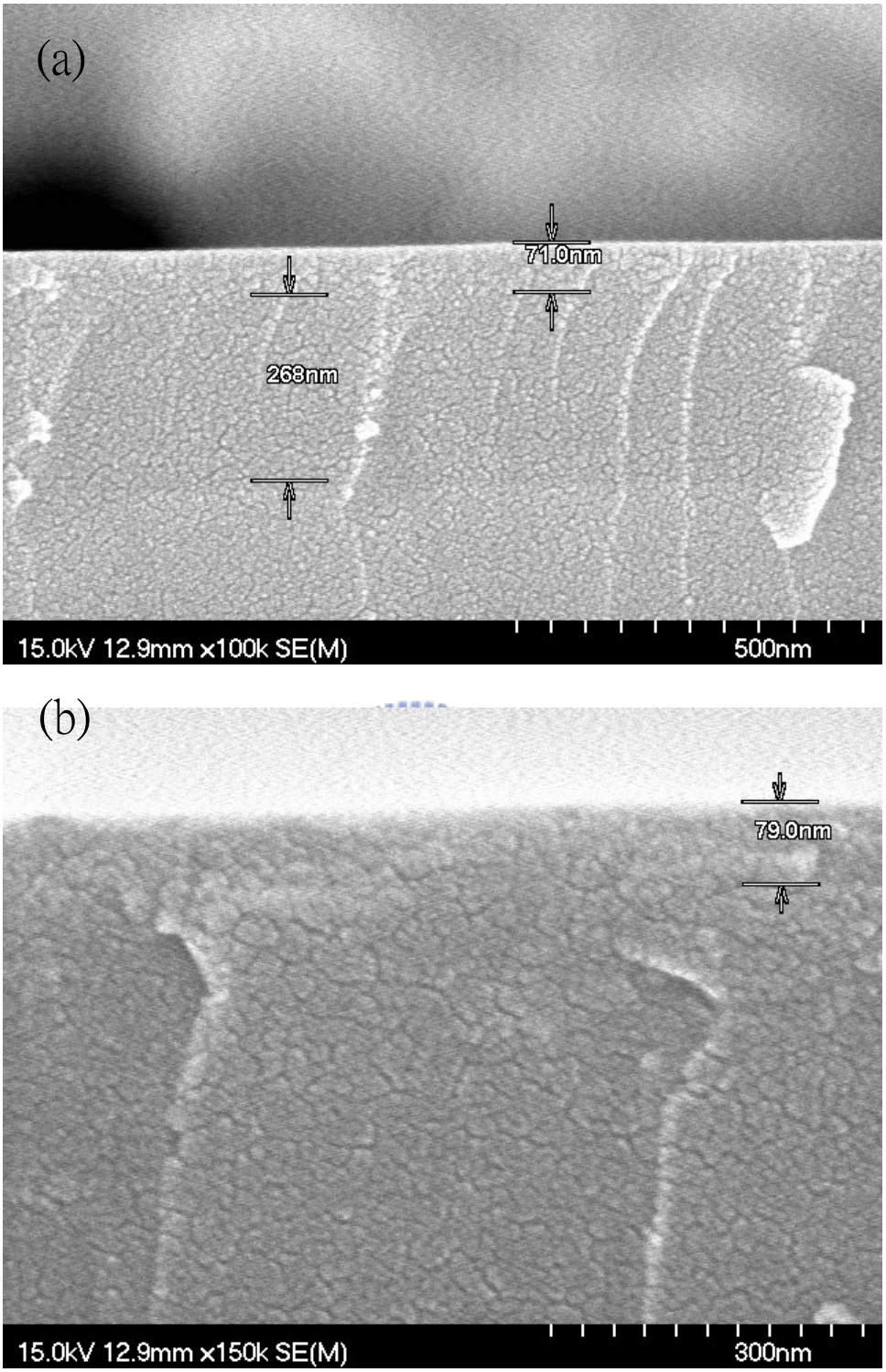

Figure 3-10. SEM images of the $TiO_{2-x}N_x$ thin film deposited by 60min sputtering time and N_2/O_2=7/2 flow rate with (a) 60W (b) 80W power supply.

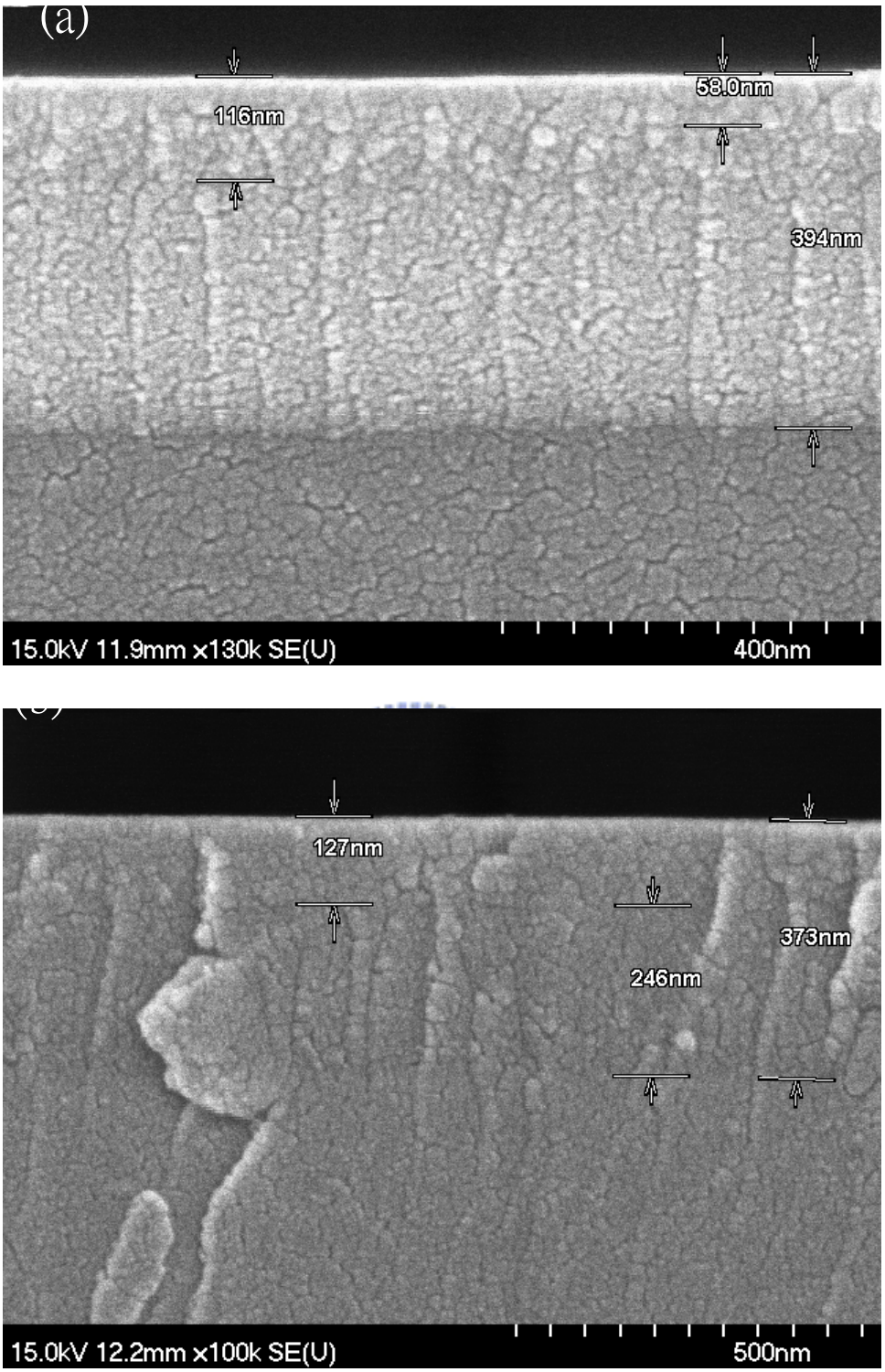

Figure 3-11. SEM images of the $TiO_{2-x}N_x$ thin film deposited by 60min sputtering time and N_2/O_2=7/2 flow rate with (a) 100W (b) 120W power supply.

Table 3-2. Growth rate of the $TiO_{2-x}N_x$ thin film with various power.

	20W	40W	60W	80W	100W	120W
60min	26	50	71	79	116	127
nm/min	0.43	0.83	1.18	1.32	1.93	2.12

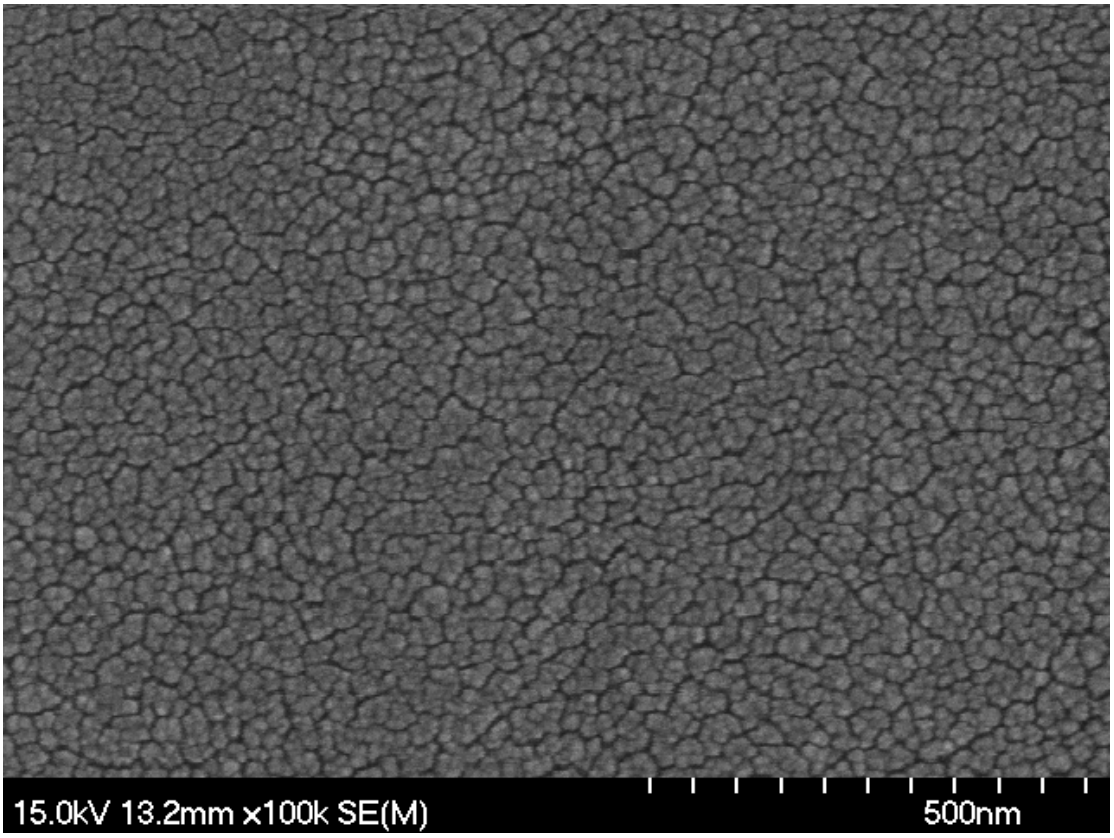

Figure 3-12. Top view image of the $TiO_{2-x}N_x$ thin film.

3.4 The Relation between Absorption to Band Gap of $TiO_{2-x}N_x$

The visible light absorption in the $TiO_{2-x}N_x$ thin films must originate from doping of nitrogen into titanium oxide. The addition of nitrogen obviously helps maintain a high degree of visible light absorption. This result indicates that band gap narrowing has been successfully achieved by doping nitrogen into the TiO_2 lattice. The absorption bands extend into the visible range was dependent on the deposited condition of the $TiO_{2-x}N_x$ thin films. It appears more red-shifted into the visible range as the increasing sputtering power. In Fig. 3-13, UV-visible absorption spectra of the $TiO_{2-x}N_x$ thin film deposited by sputtering for 60min N_2/O_2=6.5/6.0 with different powers is shown. The absorbance shoulder at 360nm is shifted into 450nm with increasing power supply. In order to observe energy band gap, we use plots of the square root of the Kubelka-Munk function against the photon energy of the $TiO_{2-x}N_x$ thin film deposited by 60min sputtering time and N_2/O_2=6.5/6.0 flow rate with various power supply. The function is shown below:

$$h\nu \quad \alpha \quad = B(h\nu \quad - E_g)^2 \qquad [3.1]$$

In Fig. 3-14, the optical energy band gaps of the $TiO_{2-x}N_x$ thin films are about 3.2eV, and the midgap levels of energy band gaps shilt to about 2.4eV. The same result can be observed in UV-visible absorption spectra of the $TiO_{2-x}N_x$ thin film deposited by 60min sputtering time and N_2/O_2=7/2 flow rate with various power supply. The shoulder at 360nm is shifted into 450nm with increasing power supply in Fig.3-15. In Fig. 3-16, the optical energy band gaps of the $TiO_{2-x}N_x$ thin films are about 3.3eV, and the midgap levels of energy band gaps shilt to about 2.4eV. The

same result also can be observed in UV-visible absorption spectra of the $TiO_{2-x}N_x$ thin film deposited by 60min sputtering time and N_2/O_2=9/0 flow rate with various power supply. The absorbance shoulder at 360nm is shifted into 450nm with increasing power supply in Fig.3-17. The optical energy band gaps of the $TiO_{2-x}N_x$ thin films are about 3.3eV in Fig. 3-18, and the midgap levels of energy band gaps shilt to about 2.5eV. The phenomenon of absorption in visible-light region has peaks in Fig.3-19. UV-visible absorption spectra of the $TiO_{2-x}N_x$ thin film deposited by 90min sputtering time and N_2/O_2=9/0 flow rate with various power supply is shown the phenomenon. In Fig.3-20, we use plots of the square root of the Kubelka-Munk function against the photon energy of the $TiO_{2-x}N_x$ thin film deposited by 90min sputtering time and N_2/O_2=9/0 flow rate with various power supply to obtain the energy band gap in the visible-light region. The midgap levels of energy band gaps of the TiO2-xNx thin films are about 2.1eV. In Fig. 3-21 shows plots of the square root of the Kubelka-Munk function against the photon energy of the $TiO_{2-x}N_x$ thin film deposited by 60min sputtering time and 100W power supply with different ratio of N_2/O_2 . We can observe that these energy band gaps narrow with increasing nitrogen flow rate.

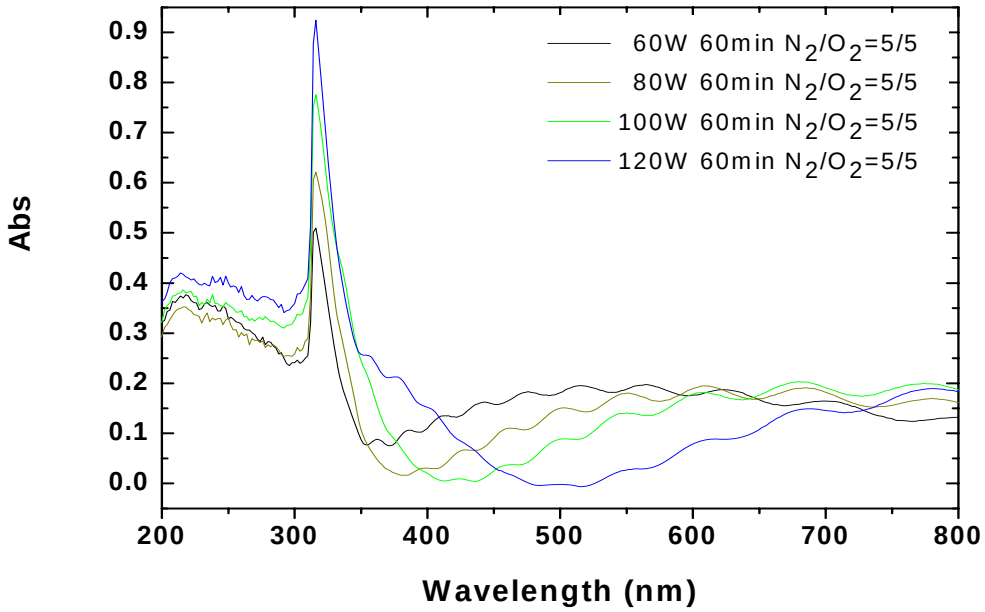

Figure 3-13 UV-visible absorption spectra of the $TiO_{2-x}N_x$ thin film deposited by 60min sputtering time and N_2/O_2=6.5/6.0 flow rate with various power supply.

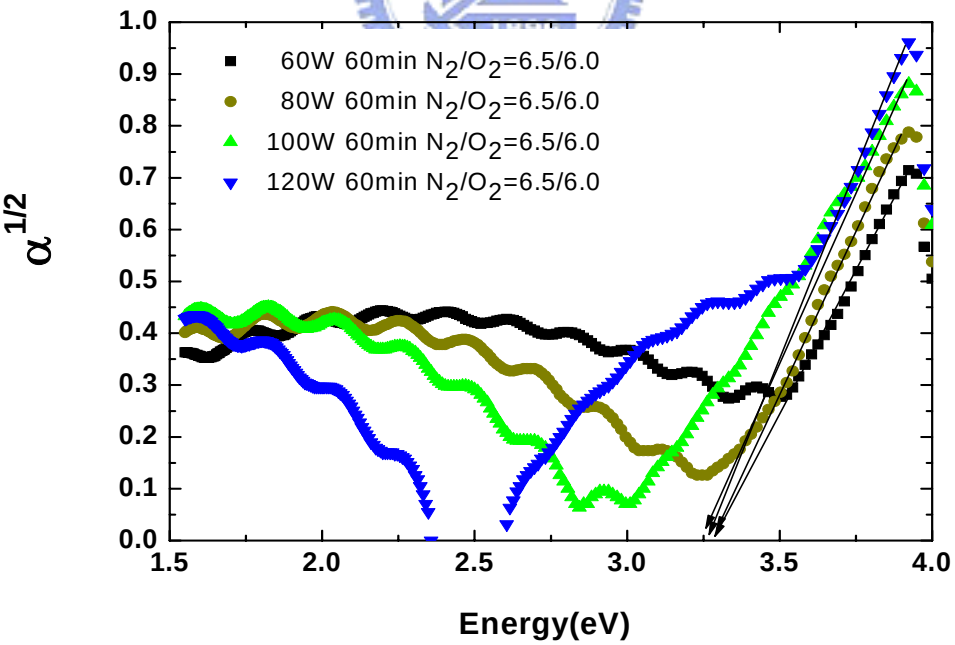

Figure 3-14 Plots of the square root of the Kubelka-Munk function against the photon energy of the $TiO_{2-x}N_x$ thin film deposited by 60min sputtering time and N_2/O_2=6.5/6.0 flow rate with various power supply.

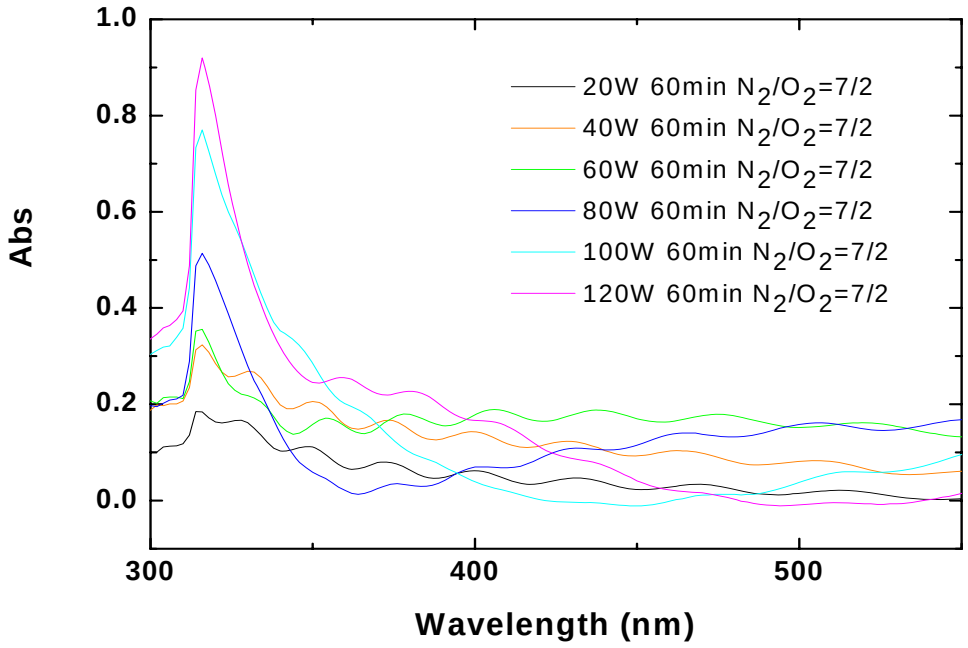

Figure 3-15 UV-visible absorption spectra of the $TiO_{2-x}N_x$ thin film deposited by 60min sputtering time and N_2/O_2=7/2 flow rate with various power supply

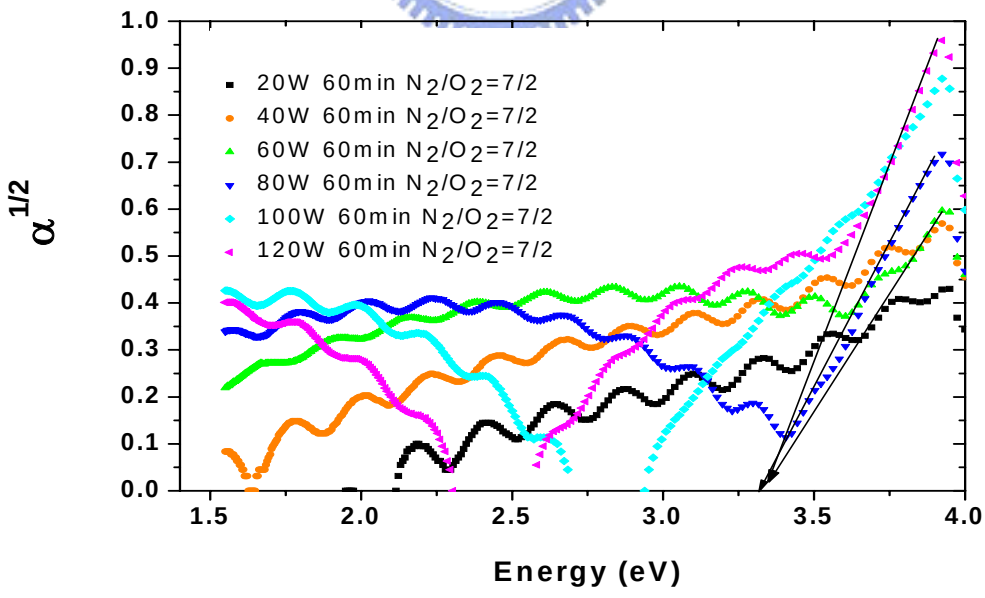

Figure 3-16 Plots of the square root of the Kubelka-Munk function against the photon energy of the $TiO_{2-x}N_x$ thin film deposited by 60min sputtering time and N_2/O_2=7/2 flow rate with various power supply.

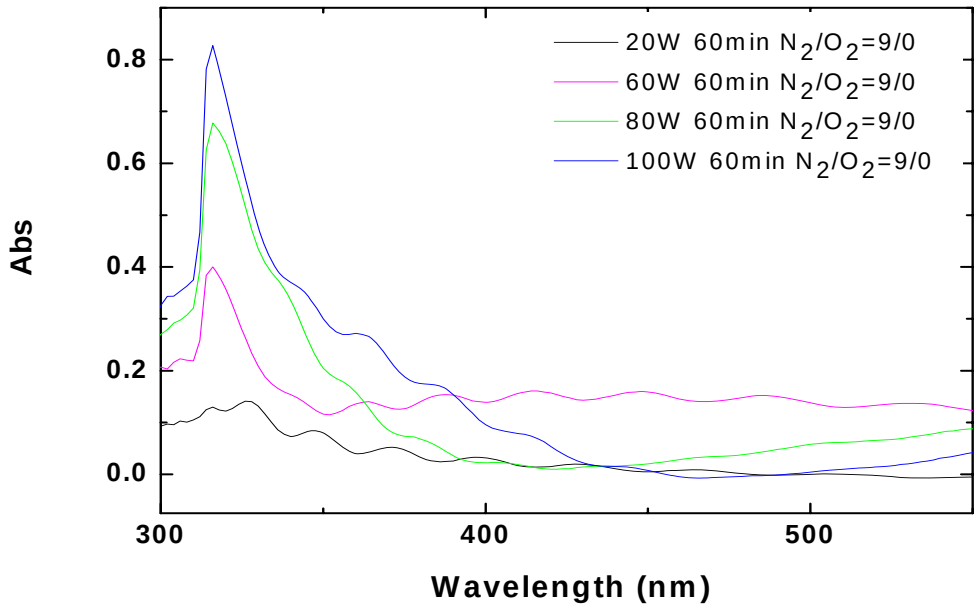

Figure 3-17 UV-visible absorption spectra of the $TiO_{2-x}N_x$ thin film deposited by 60min sputtering time and N_2/O_2=9/0 flow rate with various power supply.

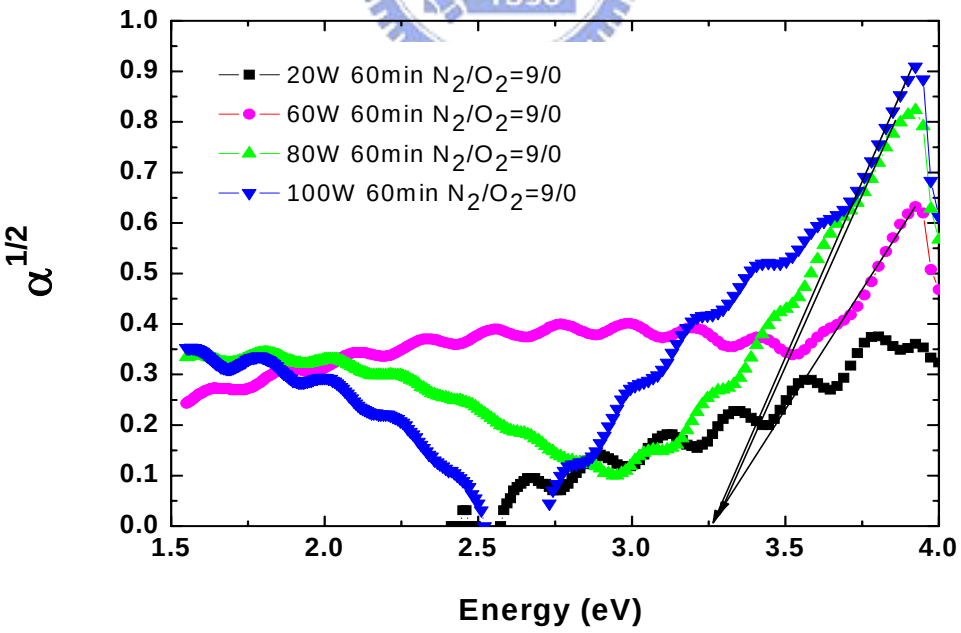

Figure 3-18 Plots of the square root of the Kubelka-Munk function against the photon energy of the $TiO_{2-x}N_x$ thin film deposited by 60min sputtering time and N_2/O_2=9/0 flow rate with various power supply.

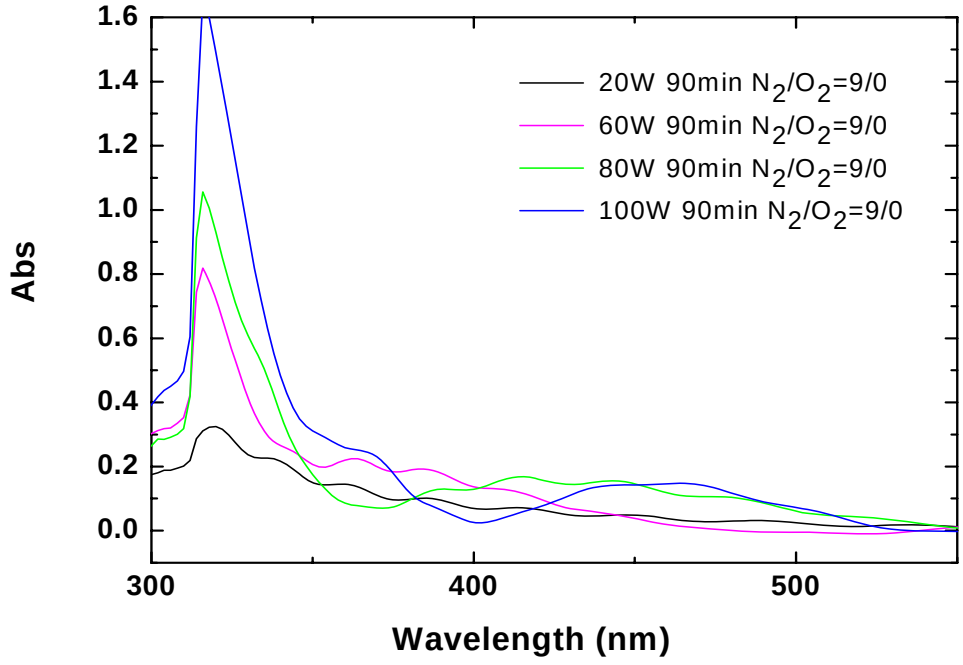

Figure 3-19 UV-visible absorption spectra of the $TiO_{2-x}N_x$ thin film deposited by 90min sputtering time and N_2/O_2=9/0 flow rate with various power supply.

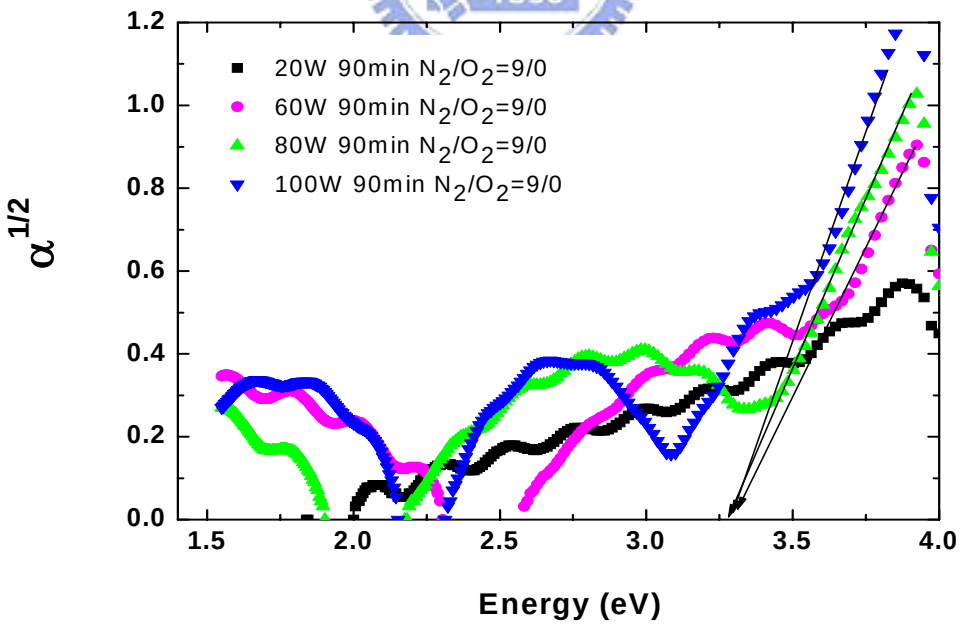

Figure 3-20 Plots of the square root of the Kubelka-Munk function against the photon energy of the $TiO_{2-x}N_x$ thin film deposited by 90min sputtering time and N_2/O_2=9/0 flow rate with various power supply.

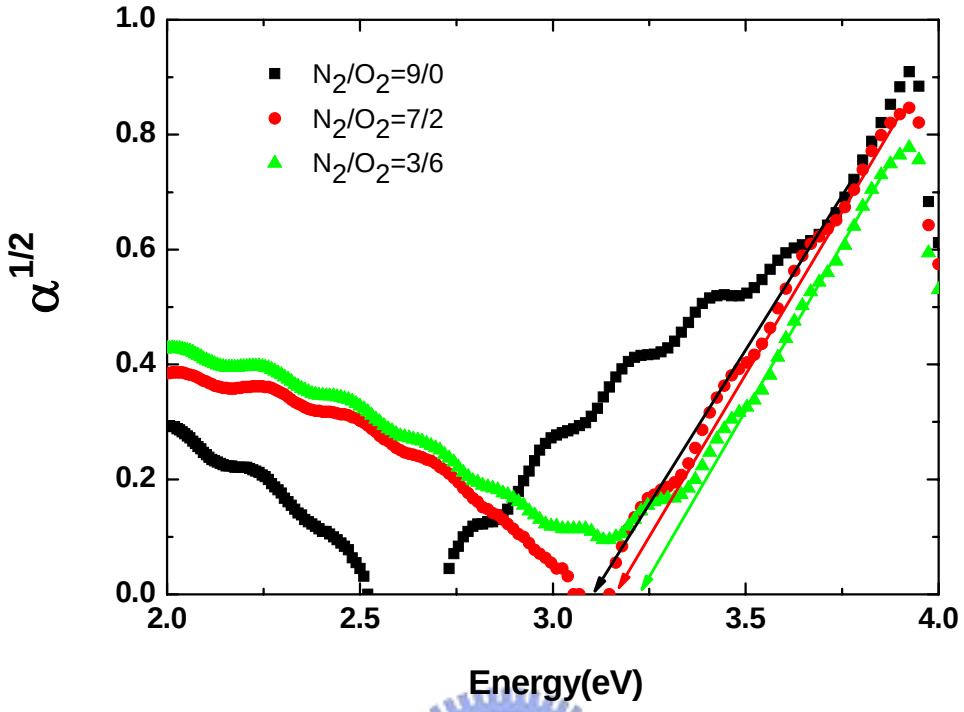

Figure 3-21 Plots of the square root of the Kubelka-Munk function against the photon energy of the $TiO_{2-x}N_x$ thin film deposited by 60min sputtering time and 100W power supply with different ratio of N_2/O_2.

3.5 Water Contact Angle

This $TiO_{2-x}N_x$ thin film deposited on PET upon UV-light which the power is 77μW/cm^2 at 365nm and visible-light illumination and then spread water droplets on the film surface exhibits water contact angle of ~8° and ~35° in Fig.3-22, respectively. The surface wettability conversion reactions are dependent on illumination. The results clearly demonstrated that the photo-induced surface wettability conversion phenomenon take place on PET plate coated with $TiO_{2-x}N_x$ thin film. The water contact angle of the $TiO_{2-x}N_x$ thin film deposited by 20W power supply for 60 min sputtering time with various x are shown in Fig.3-23, and the water contact angle of the $TiO_{2-x}N_x$ thin film deposited by 20W power supply for 60min sputtering time and N_2/O_2=5/5 flow rate is the smallest water contact angle. But roughness and the photo-induced surface wettability conversion reaction of the thin films affect the degrees of water contact angles. The water contact angle profiles of the $TiO_{2-x}N_x$ thin film deposited by 40W power supply for 60 min sputtering time with various x are shown in Fig.3-24, and the water contact angle of the $TiO_{2-x}N_x$ thin film deposited by 40W power supply for 60min sputtering time and N_2/O_2=5/5 flow rate is the smallest water contact angle. The water contact angle profiles of the $TiO_{2-x}N_x$ thin film deposited by 60W power supply for 60 min sputtering time with various x are shown in Fig.3-25, and the water contact angle of the $TiO_{2-x}N_x$ thin film deposited by 60W power supply for 60min sputtering time and N_2/O_2=5/5 flow rate is the smallest water contact angle. The water contact angle of the $TiO_{2-x}N_x$ thin film deposited by 80W power supply for 60 min sputtering time with various x are shown in Fig.3-26, and the water contact angle of the $TiO_{2-x}N_x$ thin film deposited by 80W power supply for 60min sputtering time and N_2/O_2=5/5 flow rate is the smallest water contact angle. The water contact angle of the $TiO_{2-x}N_x$ thin film deposited by

100W power supply for 60 min sputtering time with various x are shown in Fig.3-27, and the water contact angle of the $TiO_{2-x}N_x$ thin film deposited by 100W power supply for 60min sputtering time and N_2/O_2=5/5 flow rate is the smallest water contact angle. The water contact angle of the $TiO_{2-x}N_x$ thin film deposited by 120W power supply for 60 min sputtering time with various x are shown in Fig.3-28, and the water contact angle of the $TiO_{2-x}N_x$ thin film deposited by 120W power supply for 60min sputtering time and N_2/O_2=5/5 flow rate is the smallest water contact angle. Water contact angle of thin films are decreased with oxygen flow rate increasing. All profiles are shown below. The water contact angle of the $TiO_{2-x}N_x$ thin film upon UV- VIS light illumination is shown in Fig. 3-29. The water contact angles of the $TiO_{2-x}N_x$ thin films upon UV- light illumination are better than those upon VIS- light illumination. It is because that the intensity of absorbance in UV-light region is higher than that in VIS-light region.

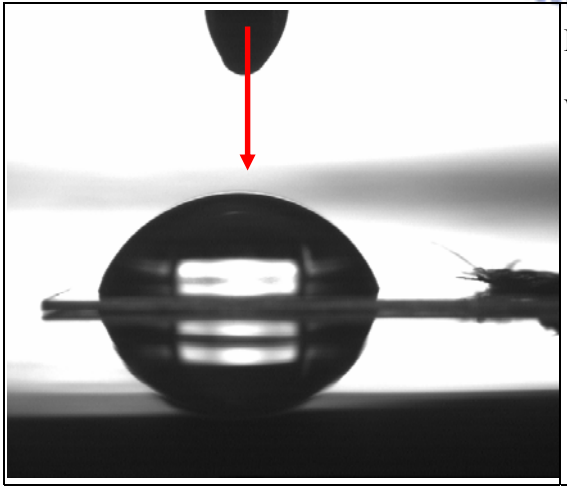

Before illuminating

Water contact angle is 65.3°.

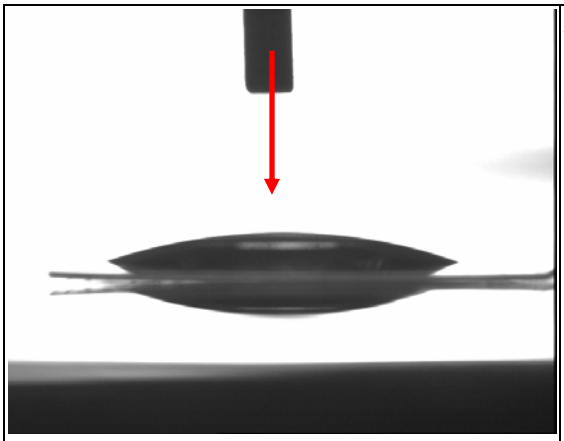	UV-light illuminating for 30min Water contact angle is 19°.
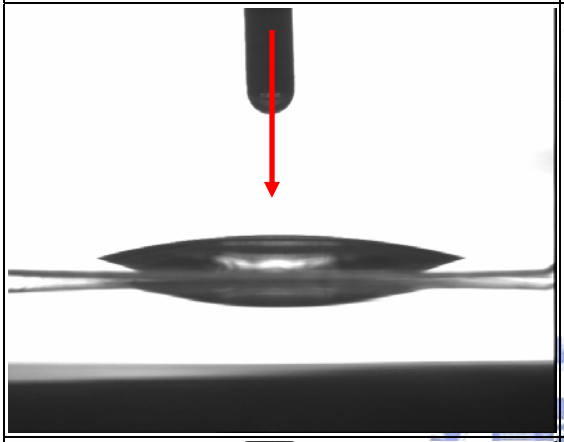	UV-light illuminating for 60min Water contact angle is 13.6°.
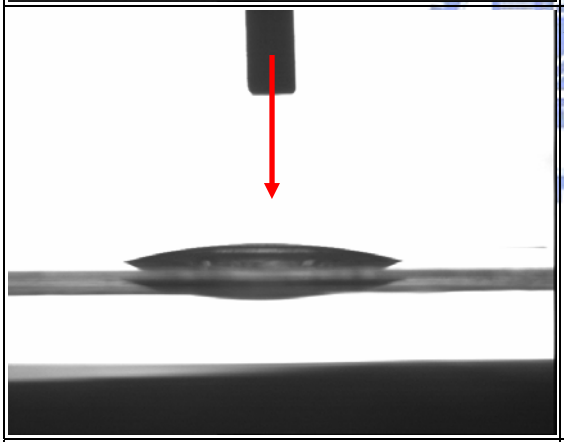	UV-light illuminating for 90min Water contact angle is 12°.
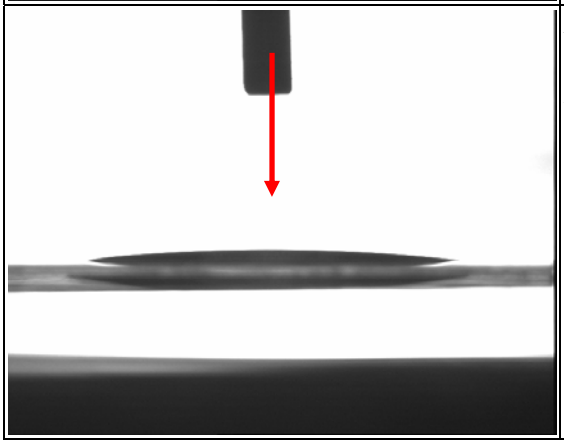	UV-light illuminating for 120min Water contact angle is 8.8°.

Figure 3-22 Water contact angle images of the $TiO_{2-x}N_x$ thin film deposited by 40W sputtering for 60min with N_2/O_2=6.5/6.0 flow rate upon UV-light illumination.

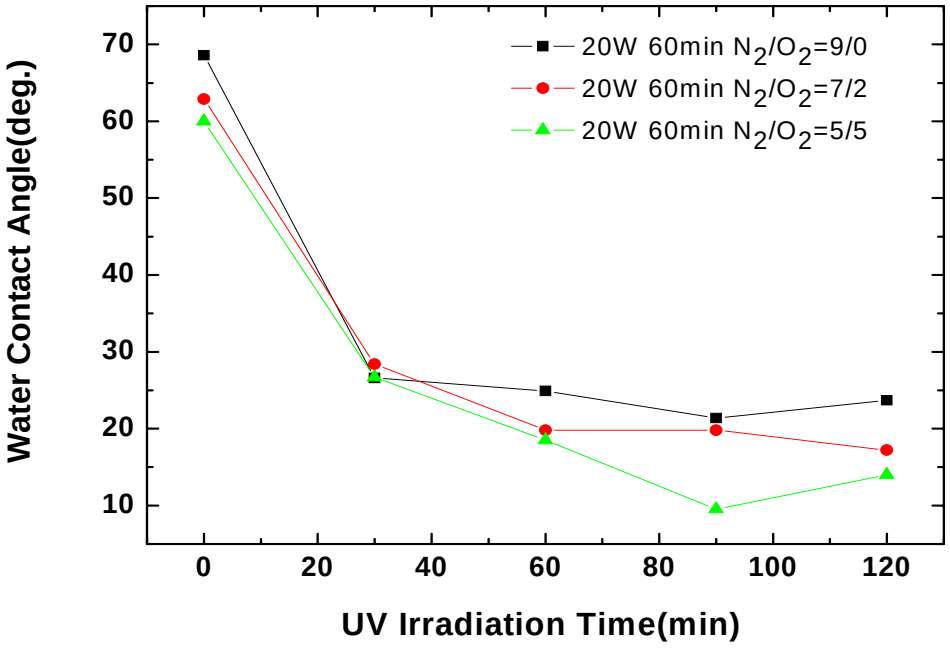

Figure 3-23 Water contact angle profiles of the $TiO_{2-x}N_x$ thin film deposited by 20W sputtering for 60 min with various x.

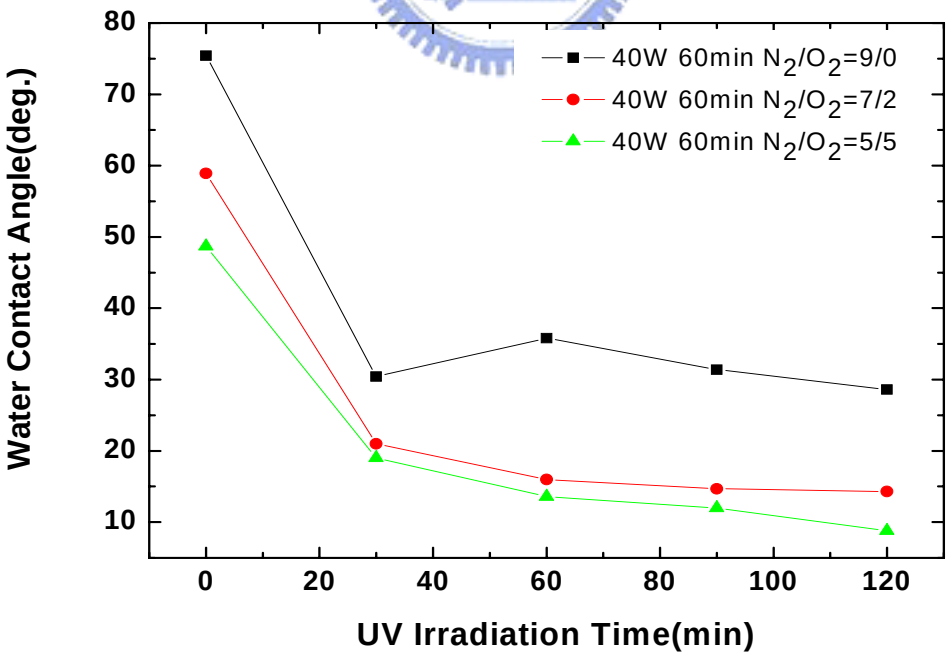

Figure 3-24 Water contact angle profiles of the $TiO_{2-x}N_x$ thin film deposited by 40W sputtering for 60 min with various x.

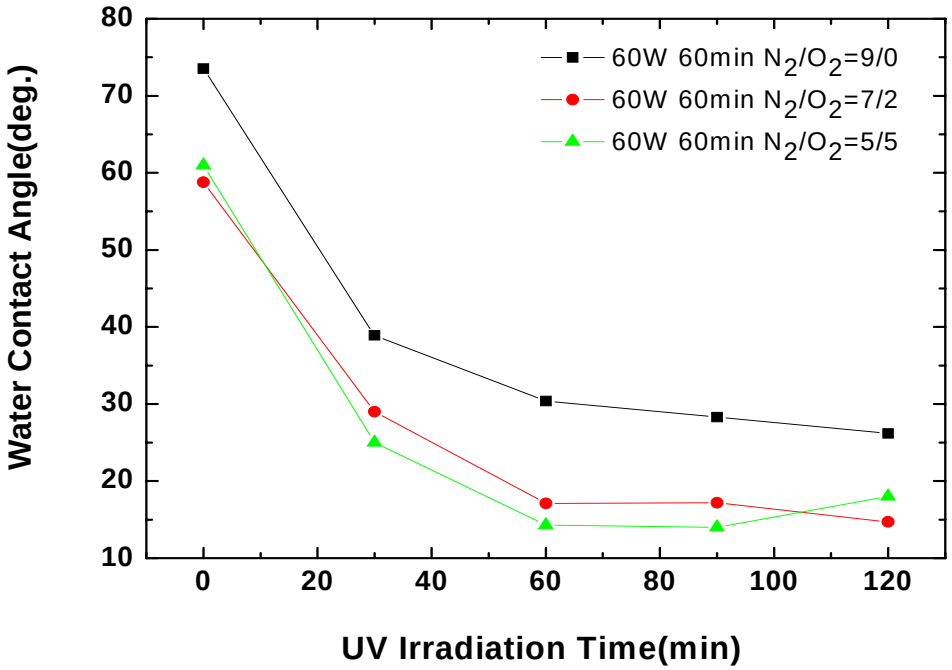

Figure 3-25 Water contact angle profiles of the $TiO_{2-x}N_x$ thin film deposited by 60W sputtering for 60 min with various x.

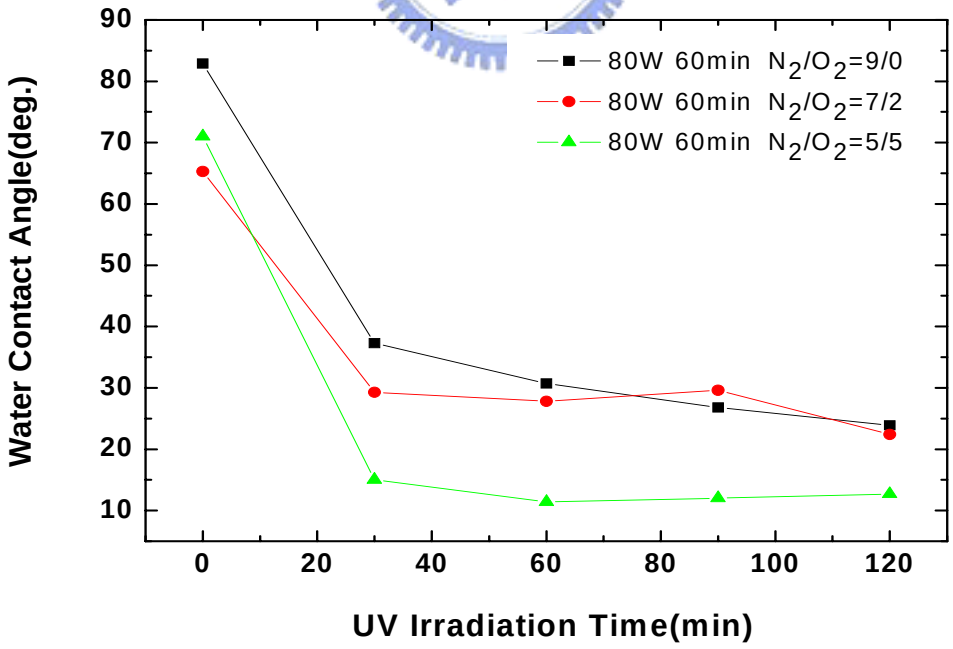

Figure 3-26 Water contact angle profiles of the $TiO_{2-x}N_x$ thin film deposited by 80W sputtering for 60 min with various x.

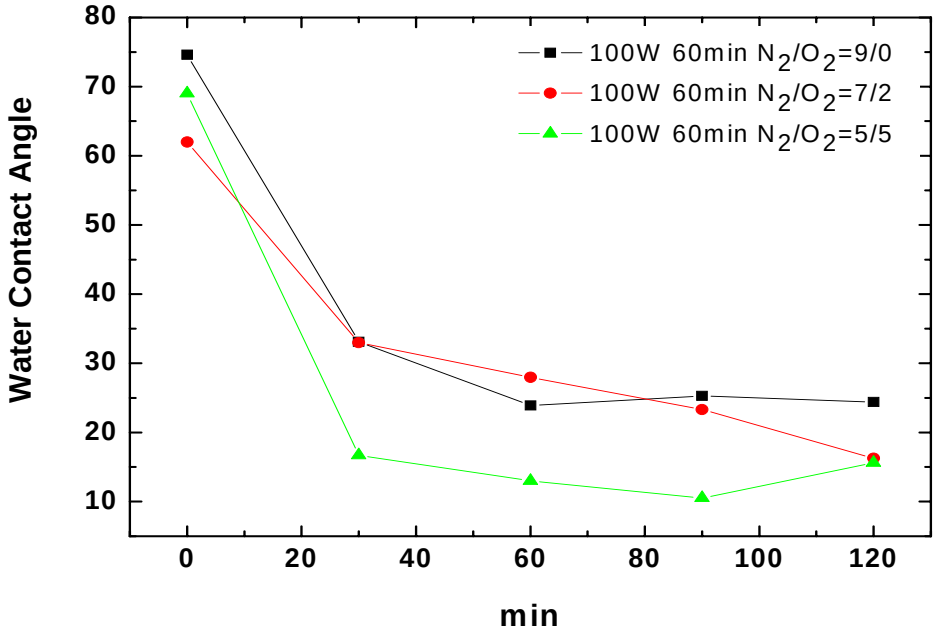

Figure 3-27 Water contact angle profiles of the $TiO_{2-x}N_x$ thin film deposited by 100W sputtering for 60 min with various x.

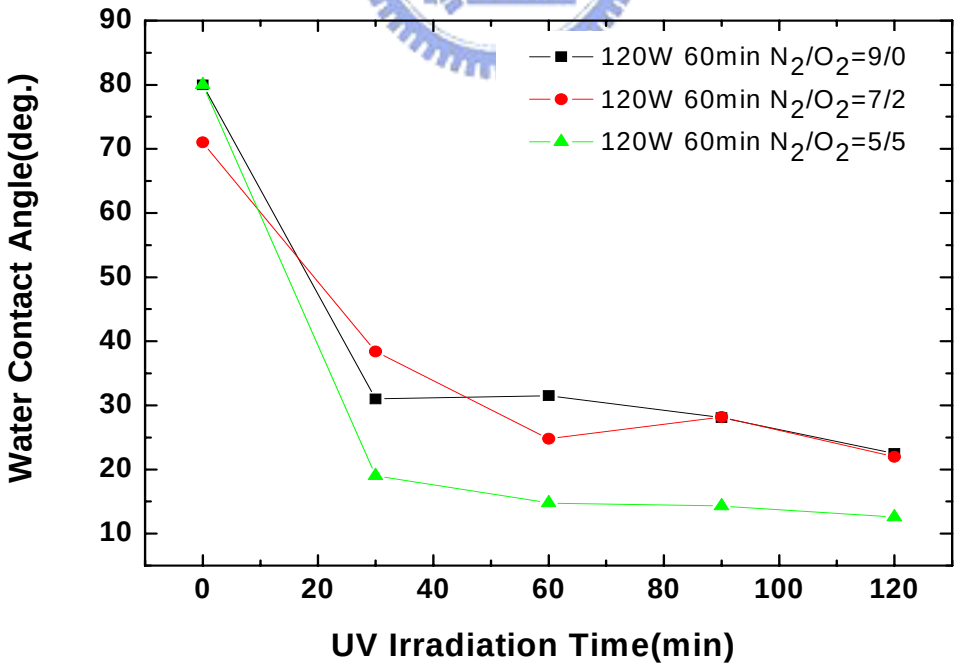

Figure 3-28 Water contact angle profiles of the $TiO_{2-x}N_x$ thin film deposited by 120W sputtering for 60 min with various x.

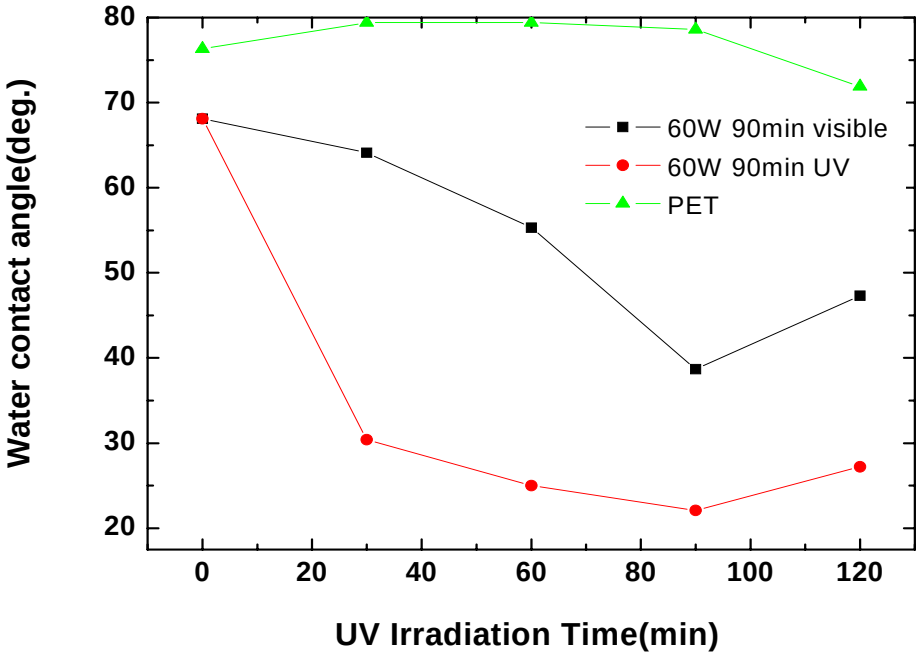

Figure 3-29 Water contact angle profiles of the $TiO_{2-x}N_x$ thin film upon UV-VIS light illumination.

3.6 Roughness Effects on Water Contact Angle

After the $TiO_{2-x}N_x$ thin film has deposited, we sputter extra 5min Ar plasma treatment. We can observe that the first water contact angle is lower than another sample without extra Ar plasma treatment. In Fig3-30, The effect of extra Ar plasma in water contact angle of the $TiO_{2-x}N_x$ thin film deposited by 100W power sputtering for 90min with N_2/O_2=9/0 flow rate is shown. The roughness of the $TiO_{2-x}N_x$ thin film deposited by 100W sputtering for 90min with N_2/O_2=9/0 flow rate with extra Ar plasma treatment is 0.292nm in Fig. 3-31. The roughness of the $TiO_{2-x}N_x$ thin film deposited by 100W sputtering for 90min with N_2/O_2=9/0 flow rate without extra Ar plasma treatment is 0.599nm in Fig.3-32. The $TiO_{2-x}N_x$ thin film of extra Ar plasma treatment is smoother than the one without extra Ar plasma treatment and water contact angle is also smaller. However, the effect of roughness for the water contact angle of the $TiO_{2-x}N_x$ thin film deposited with the same conditions is related with his water contact angle. In Fig. 3-35, the water contact angle of the $TiO_{2-x}N_x$ thin film deposited with the same conditions has different degrees. The roughness of another $TiO_{2-x}N_x$ thin film deposited by 100W sputtering for 90min with N_2/O_2=9/0 flow rate without extra Ar plasma treatment is 3.767nm in Fig. 3-36. The one which roughness is 0.599nm has a lower water contact angle of ~55°C and another water contact angle is about 75°C in Fig. 3-35.

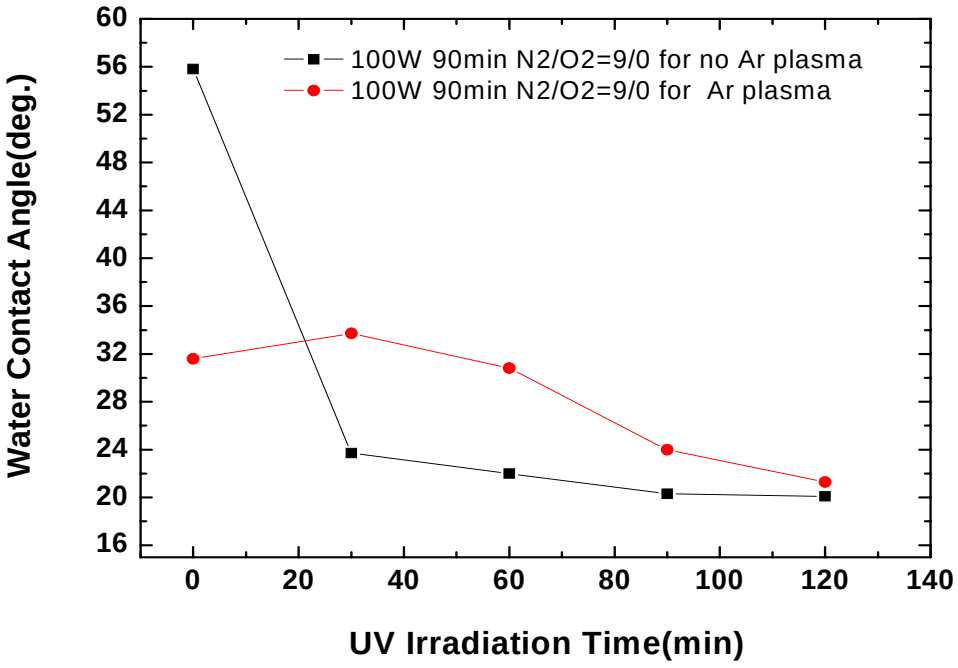

Figure 3-30 The effect of extra Ar plasma treatment for water contact angle of the $TiO_{2-x}N_x$ thin film deposited by 100W power sputtering for 90min with N_2/O_2=9/0 flow rate.

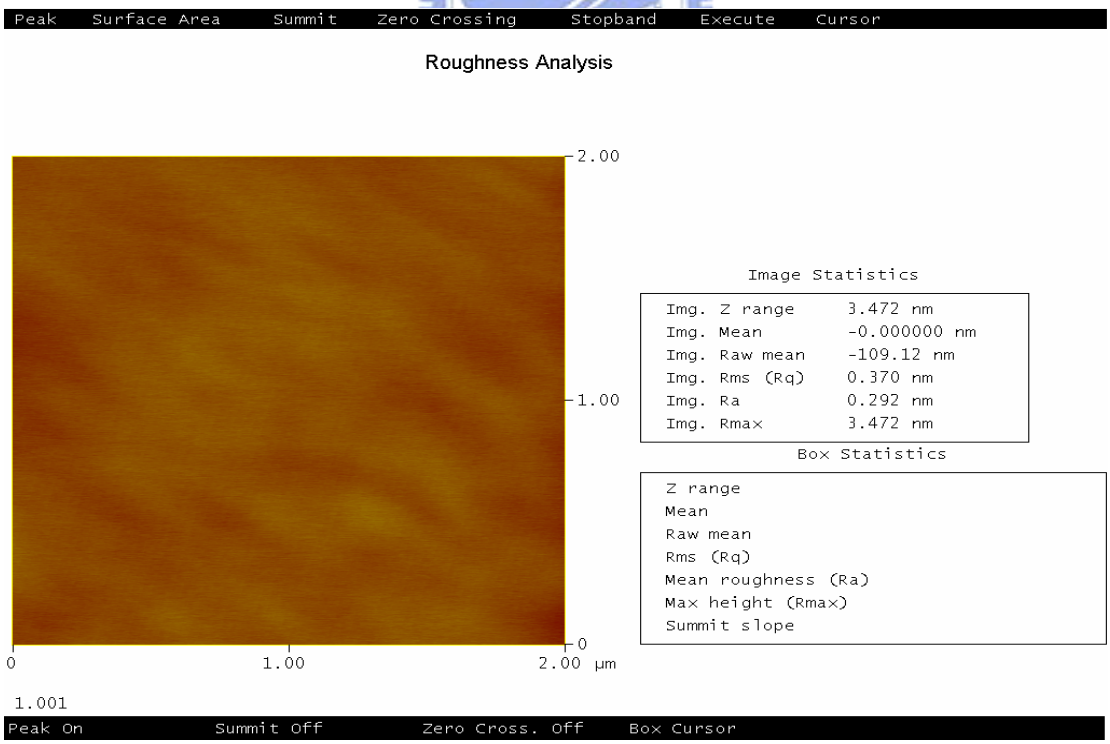

Figure 3-31 Roughness of the $TiO_{2-x}N_x$ thin film deposited by 100W sputtering for 90min with N_2/O_2=9/0 flow rate with extra Ar plasma treatment.

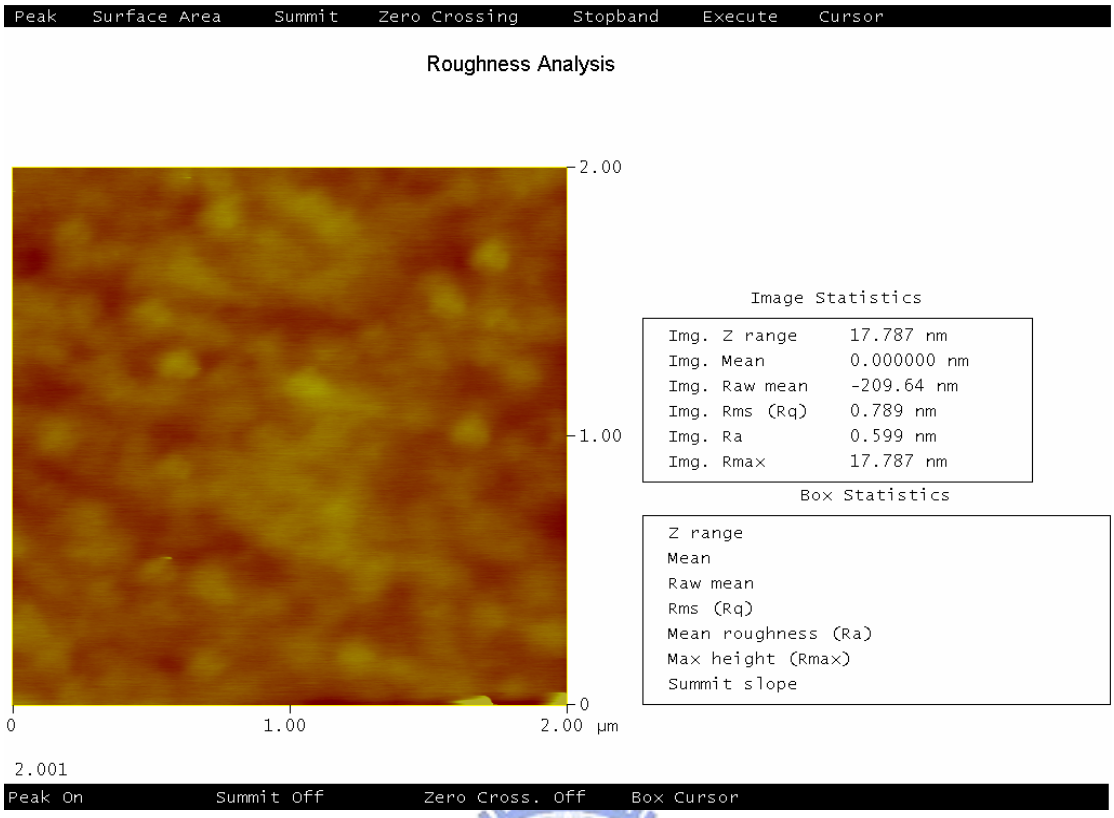

Figure 3-32 Roughness of the $TiO_{2-x}N_x$ thin film deposited by 100W sputtering for 90min with N_2/O_2=9/0 flow rate without extra Ar plasma treatment.

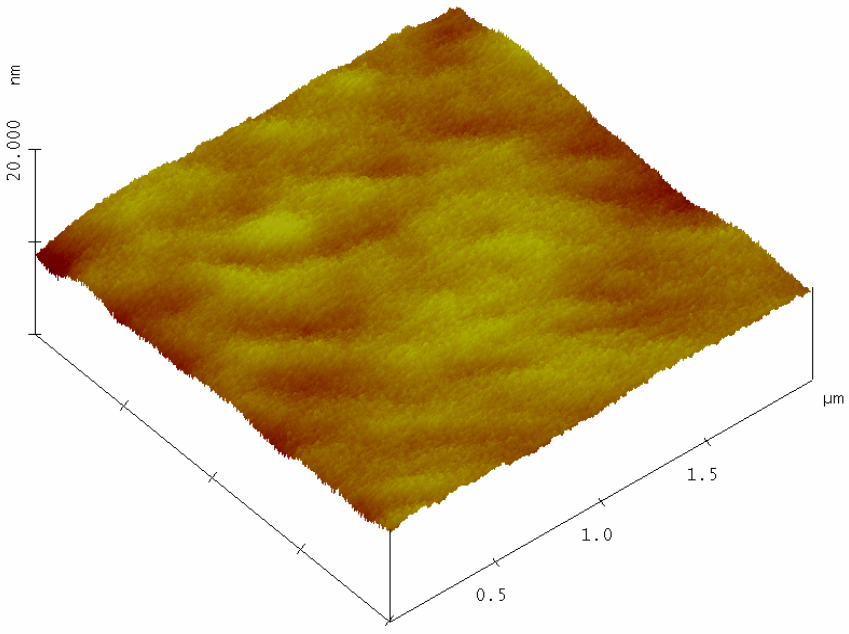

Figure 3-33 3D AFM images of the $TiO_{2-x}N_x$ thin film deposited by 100W sputtering for 90min with N_2/O_2=9/0 flow rate with extra Ar plasma treatment.

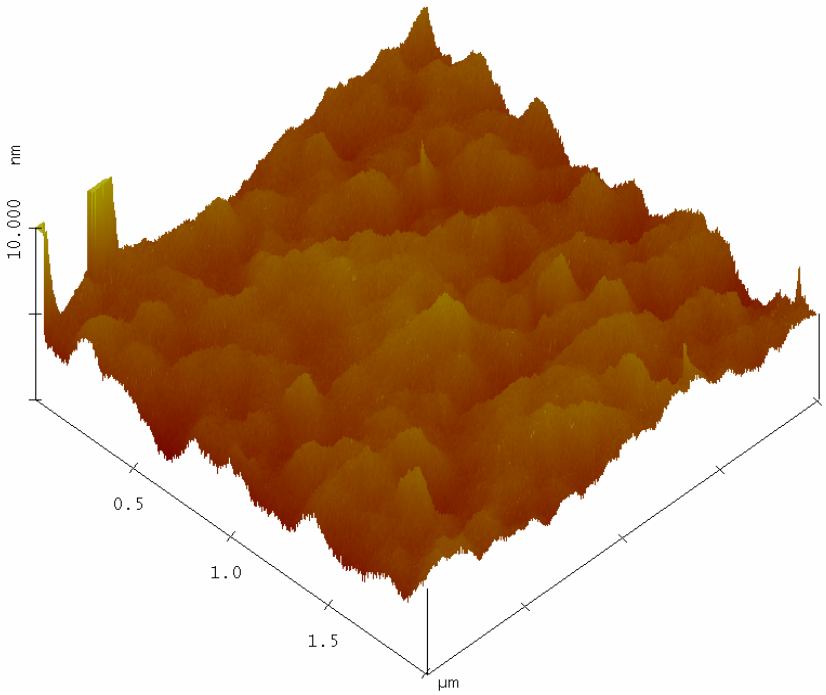

Figure 3-34 3D AFM images of the $TiO_{2-x}N_x$ thin film deposited by 100W sputtering for 90min with N_2/O_2=9/0 flow rate without extra Ar plasma treatment.

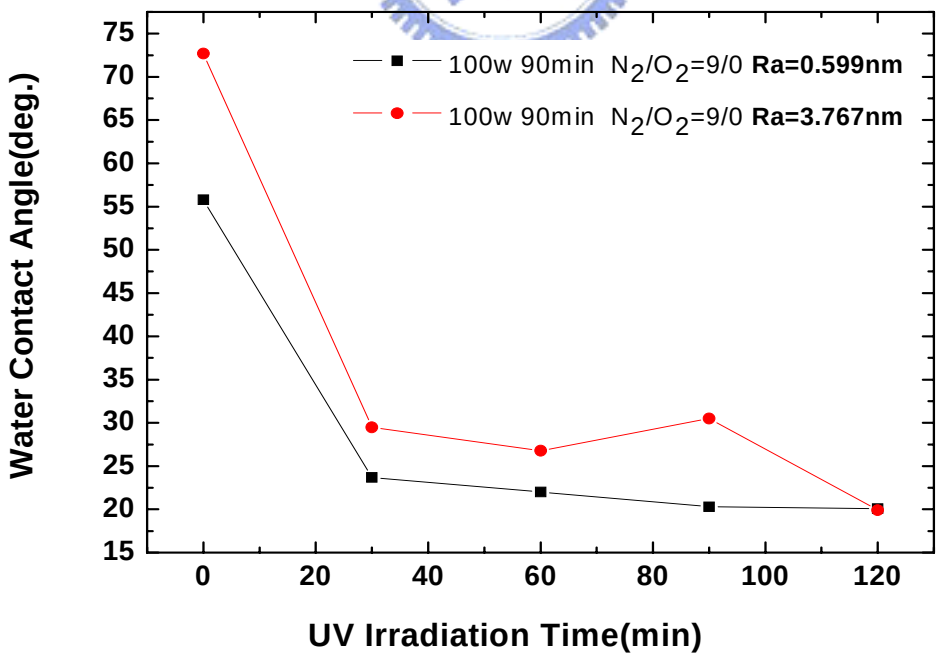

Figure 3-35 The effect of roughness for the water contact angle of the $TiO_{2-x}N_x$ thin film deposited with the same conditions.

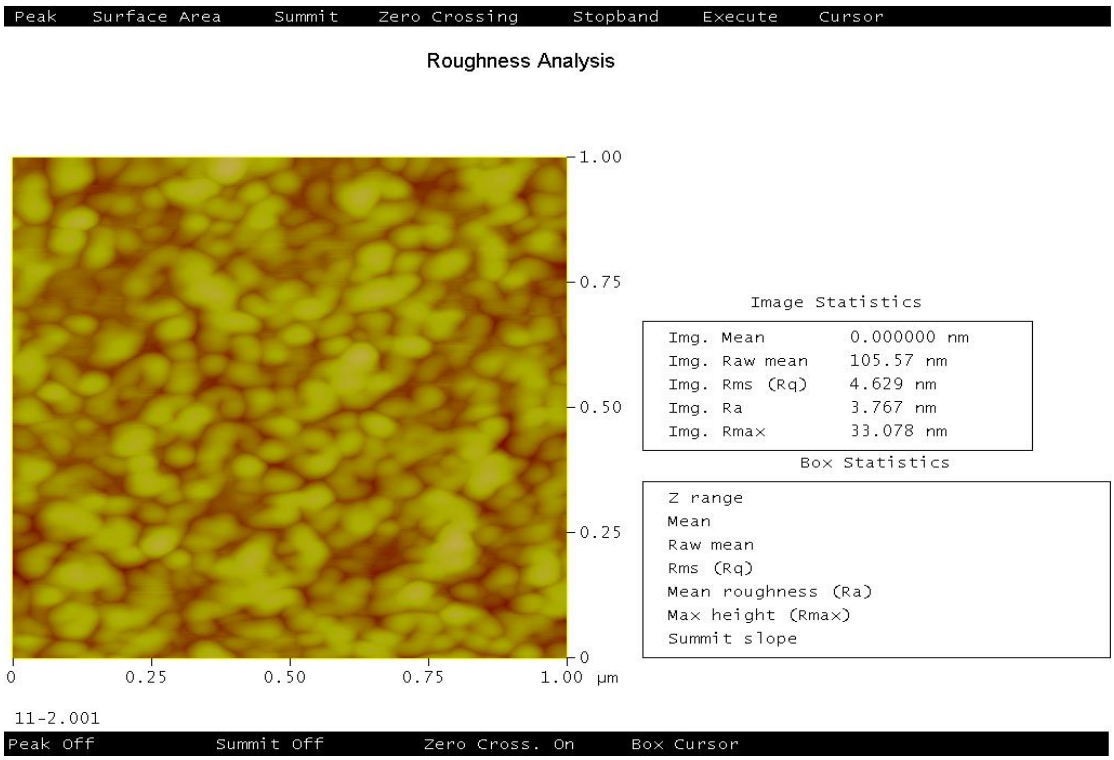

Figure 3-36 Roughness of another $TiO_{2-x}N_x$ thin film deposited by 100W sputtering for 90min with N_2/O_2=9/0 flow rate without extra Ar plasma.

3.7 Light Intensity Effects on Water Contact Angle

The $TiO_{2-x}N_x$ thin film illuminated upon different light intensity affects the water contact angle. The water contact angle upon 77uW/cm2 source illumination is about 10°C. The water contact angle upon 18uW/cm2 source illumination is about 30 °C in Fig.3-37. Light intensity decreases about 76.6 percentage and the water contact angle increases 3 times. The UV-light has no public intensity, so that the light sources affect the experiment result

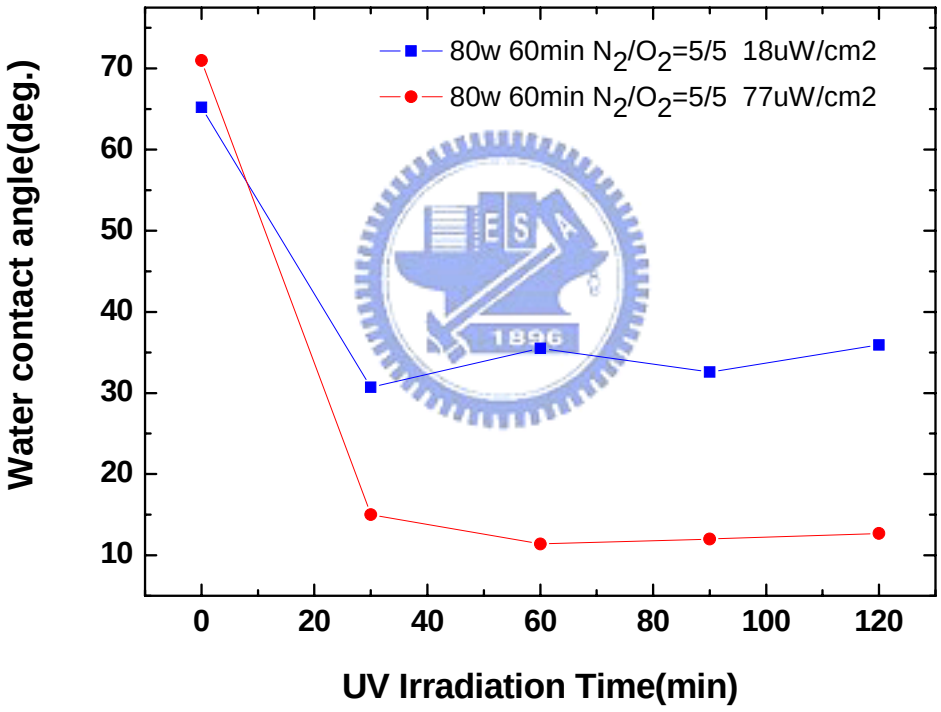

Figure 3-37 The $TiO_{2-x}N_x$ thin film illuminated upon different light intensity.

3.8 The Absorption on various substrates of PET and Glass

UV-visible absorption spectra of the $TiO_{2-x}N_x$ thin film deposited on basis of glass is much smooth than the $TiO_{2-x}N_x$ thin film deposited on PET substrate. The $TiO_{2-x}N_x$ thin film deposited on glass substrate by 90min sputtering time and N_2/O_2=9/0 flow rate with various power supply is shown in Fig. 3-38. The intensity of UV-visible absorption increases with power supply. The intensity of absorption in UV region is also larger than the intensity of absorption in visible region. In Fig. 3-39, we can observe the region of the peak the $TiO_{2-x}N_x$ thin film deposited on glass at 300nm is wider and larger than the region of the peak the $TiO_{2-x}N_x$ thin film deposited on PET at 320nm. However, we also can observe the visible region of the peak the $TiO_{2-x}N_x$ thin film deposited on glass at 400nm to 600nm is smaller than the visible region of the peak the $TiO_{2-x}N_x$ thin film deposited on PET at 400nm to 600nm in Fig. 3-40. UV-visible absorption spectra of the $TiO_{2-x}N_x$ thin film deposited on glass and PET substrates by 90min sputtering time and N_2/O_2=9/0 flow rate with 120W power supply at UV region is shown in Fig.3-43. The area of glass's absorption in UV region is larger than that absorption of PET in UV region in Fig. 3-43. So that the water contact angle on glass substrate with UV-illuminated is smaller than PET UV substrate in Fig. 3-44. The water contact angle on glass substrate with UV-illuminated is about 9.7° and the water contact angle on PET substrate is about 12.9°. The area of PET's absorption in visible region is larger than the area of glass's absorption in visible region in Fig.3-45. So that the water contact angle glass substrate with visible-illuminated is larger than the water contact angle PET substrate in Fig. 3-46. The water contact angle on glass substrate with visible-illuminated is about 50° and of PET substrate is about 39.4°. The roughness of glass is about 0.261nm and that of PET is 2.35nm in Fig.3-48 and Fig.3-49. It is

another reason why the water contact angle of the $TiO_{2-x}N_x$ thin film deposited on glass substrate is better than the water contact angle of the $TiO_{2-x}N_x$ thin film deposited on PET substrate in Fig.3-47.

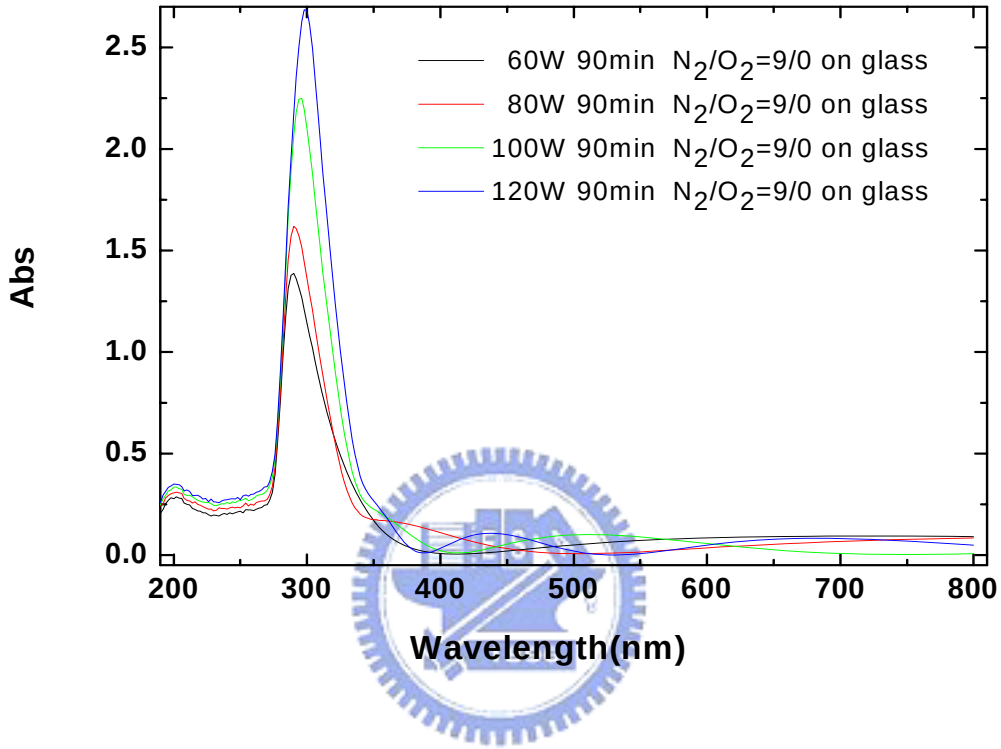

Figure 3-38 UV-visible absorption spectra of the $TiO_{2-x}N_x$ thin film deposited on basis of glass by 90min sputtering time and N_2/O_2=9/0 flow rate with various power supply.

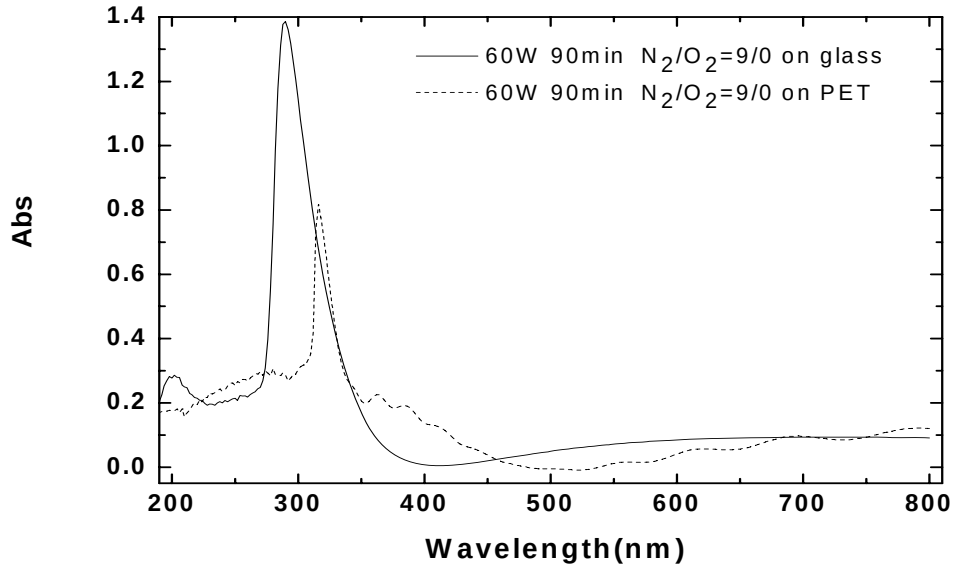

Figure 3-39 UV-visible absorption spectra of the $TiO_{2-x}N_x$ thin film deposited on basis of glass and PET by 90min sputtering time and N_2/O_2=9/0 flow rate with 60W power supply.

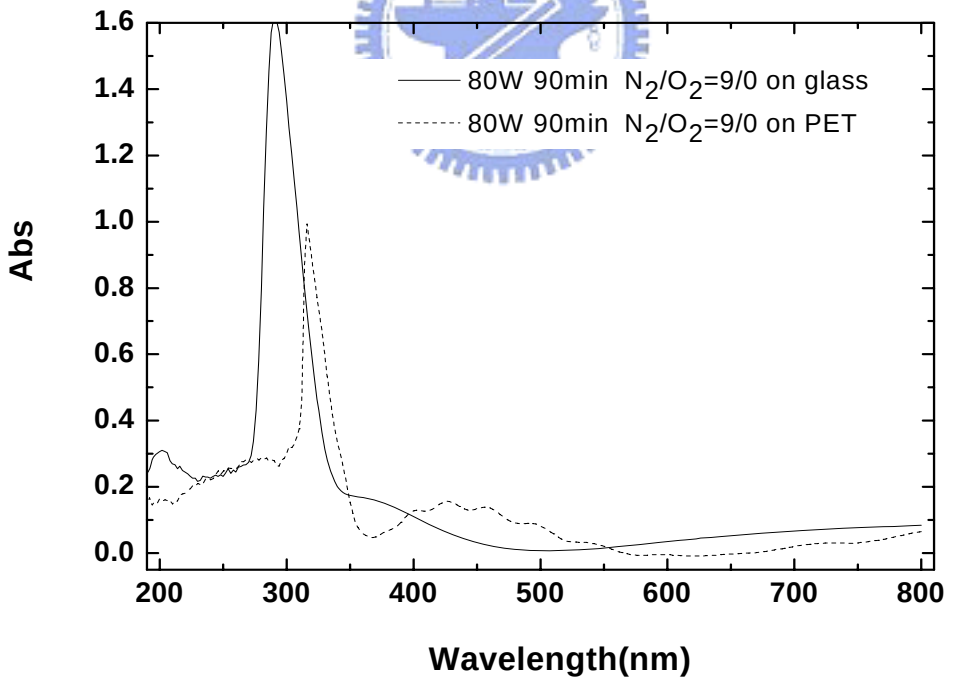

Figure 3-40 UV-visible absorption spectra of the $TiO_{2-x}N_x$ thin film deposited on basis of glass and PET by 90min sputtering time and N_2/O_2=9/0 flow rate with 80W power supply.

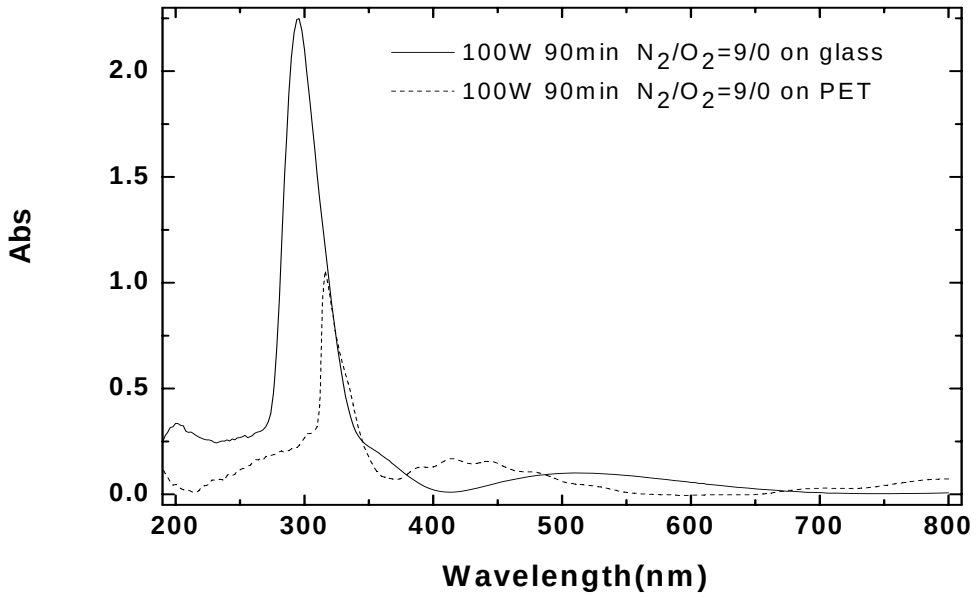

Figure 3-41 UV-visible absorption spectra of the $TiO_{2-x}N_x$ thin film deposited on basis of glass and PET by 90min sputtering time and N_2/O_2=9/0 flow rate with 100W power supply.

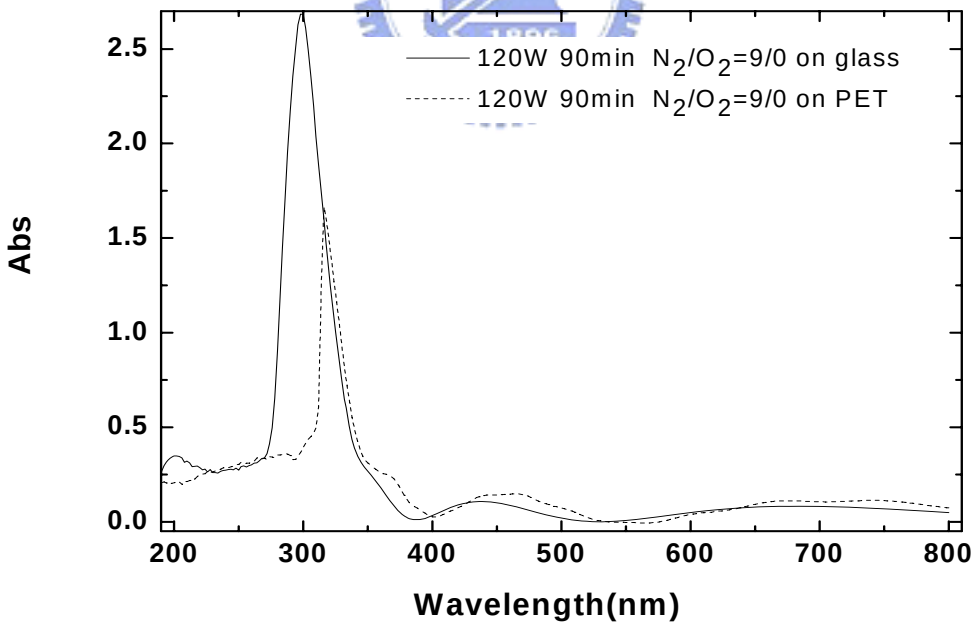

Figure 3-42 UV-visible absorption spectra of the $TiO_{2-x}N_x$ thin film deposited on basis of glass and PET by 90min sputtering time and N_2/O_2=9/0 flow rate with 120W power supply.

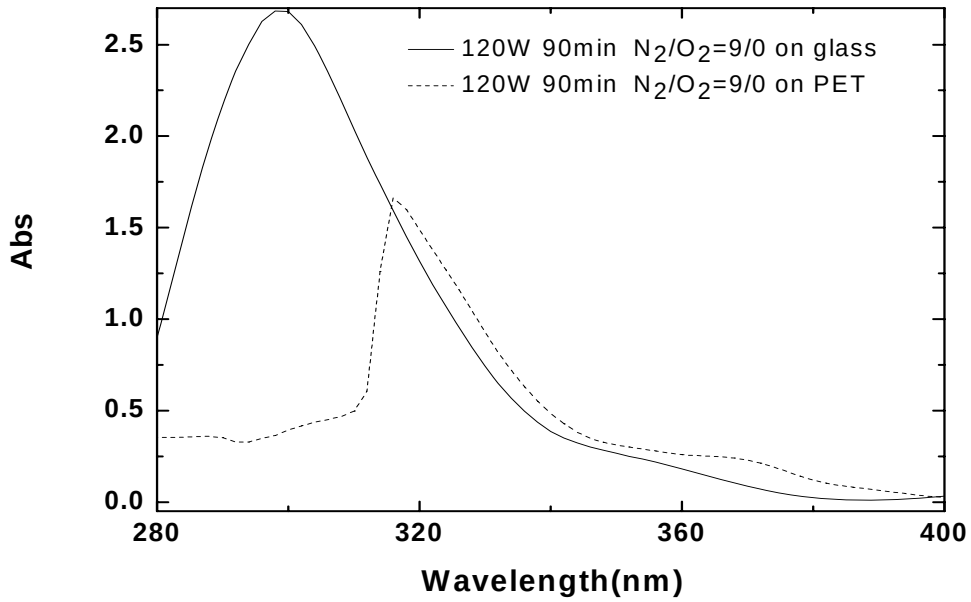

Figure 3-43 UV-visible absorption spectra of the $TiO_{2-x}N_x$ thin film deposited on basis of glass and PET by 90min sputtering time and N_2/O_2=9/0 flow rate with 120W power supply at UV region.

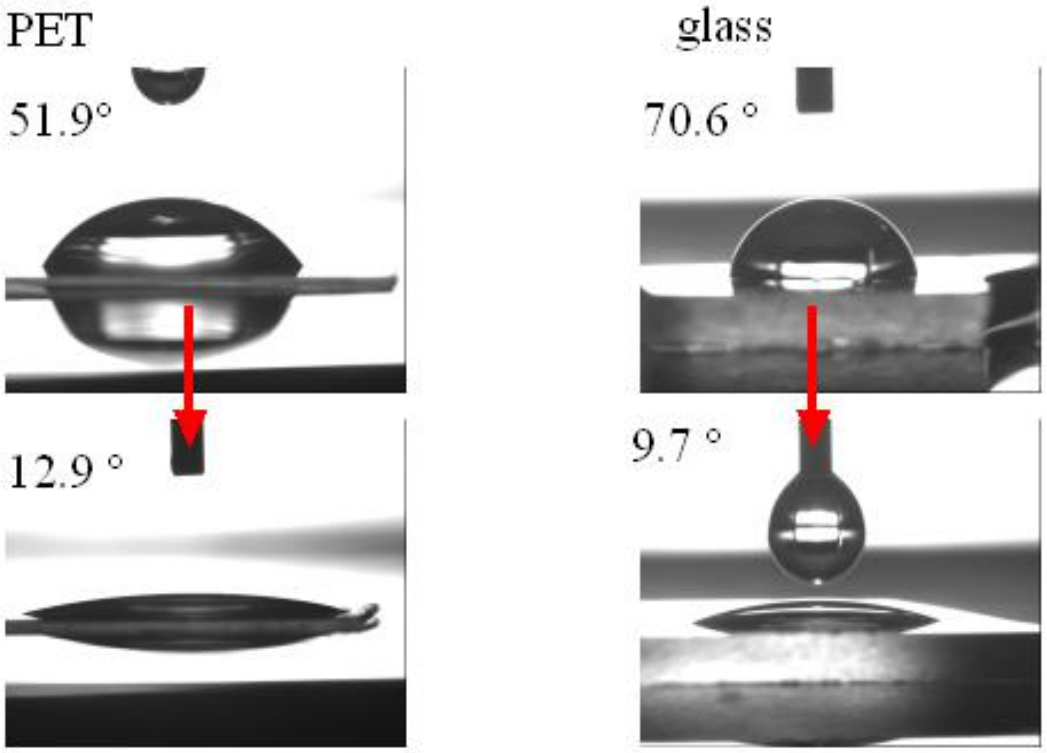

Figure 3-44 Water contact angle images of the $TiO_{2-x}N_x$ thin film deposited by 120W sputtering for 90min with N_2/O_2=9/0 flow rate upon UV-light illumination.

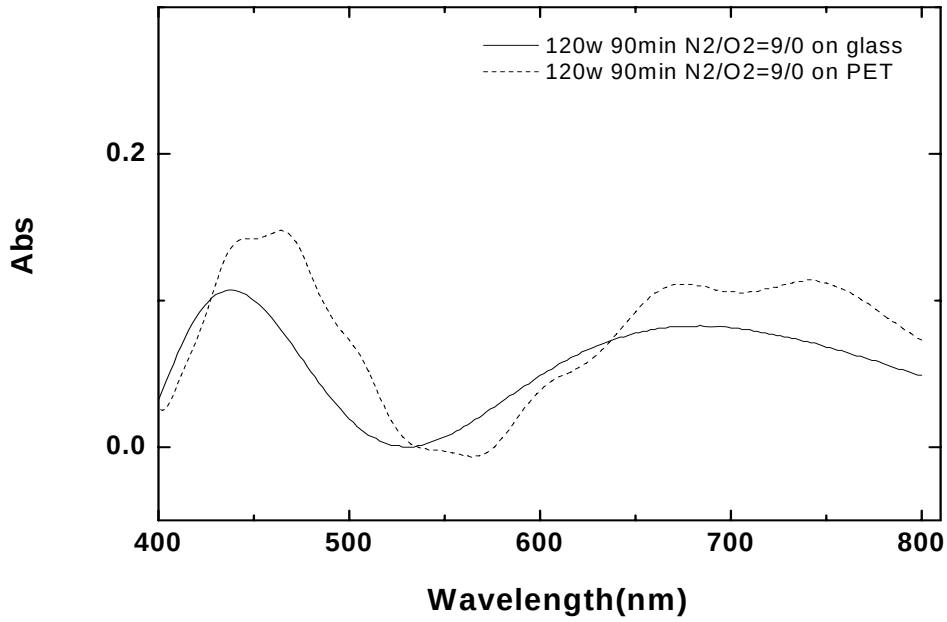

Figure 3-45 UV-visible absorption spectra of the $TiO_{2-x}N_x$ thin film deposited on basis of glass and PET by 90min sputtering time and N_2/O_2=9/0 flow rate with 120W power supply at visible region.

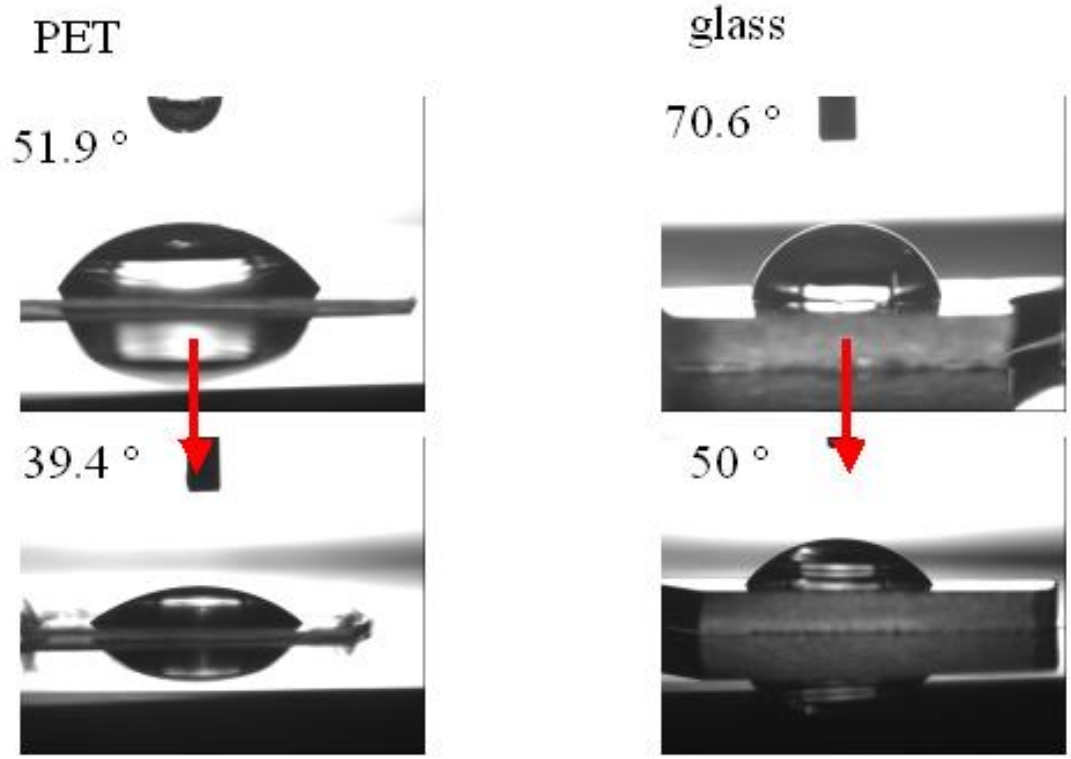

Figure 3-46 Water contact angle images of the $TiO_{2-x}N_x$ thin film deposited by 120W sputtering for 90min with N_2/O_2=9/0 flow rate upon visible-light illumination.

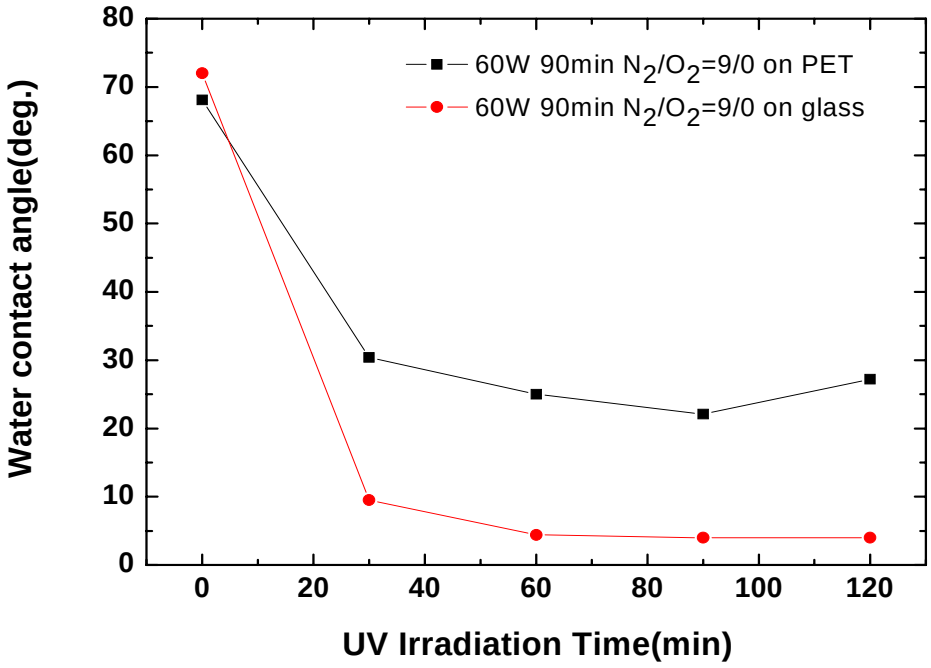

Figure 3-47 Water contact angle images of the $TiO_{2-x}N_x$ thin film deposited on bases of PET and glass.

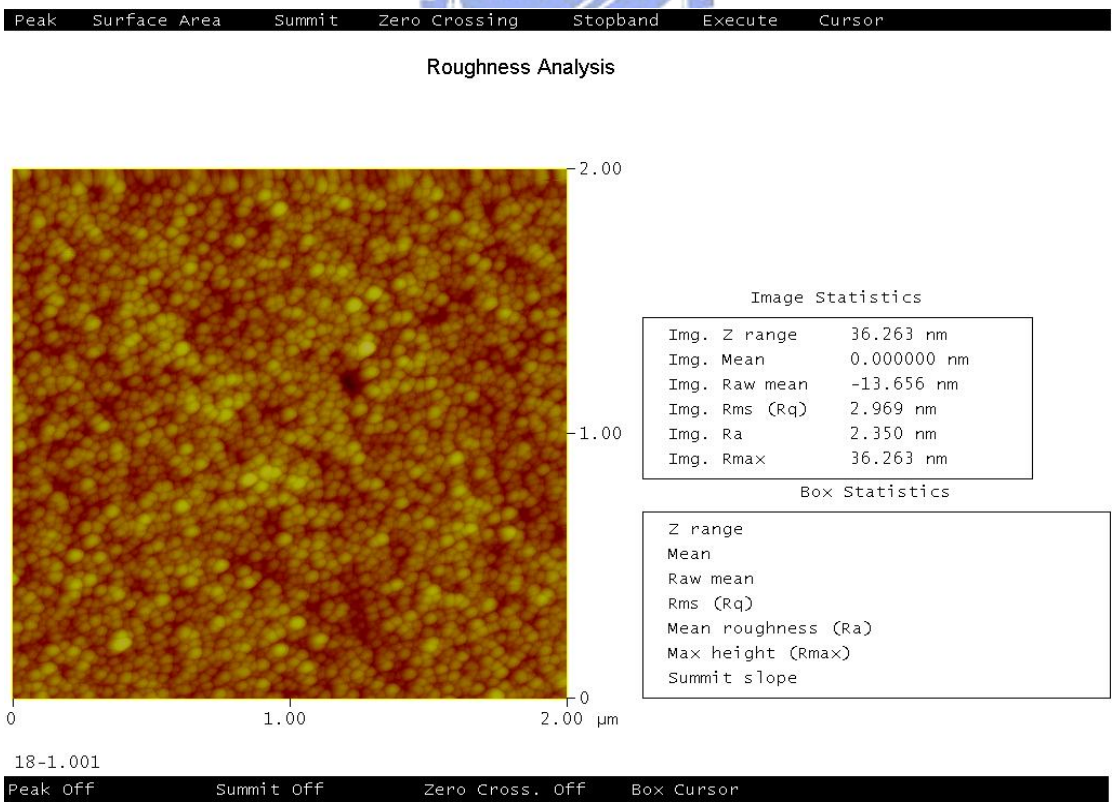

Figure 3-48 The roughness of the $TiO_{2-x}N_x$ thin film deposited on base of PET.

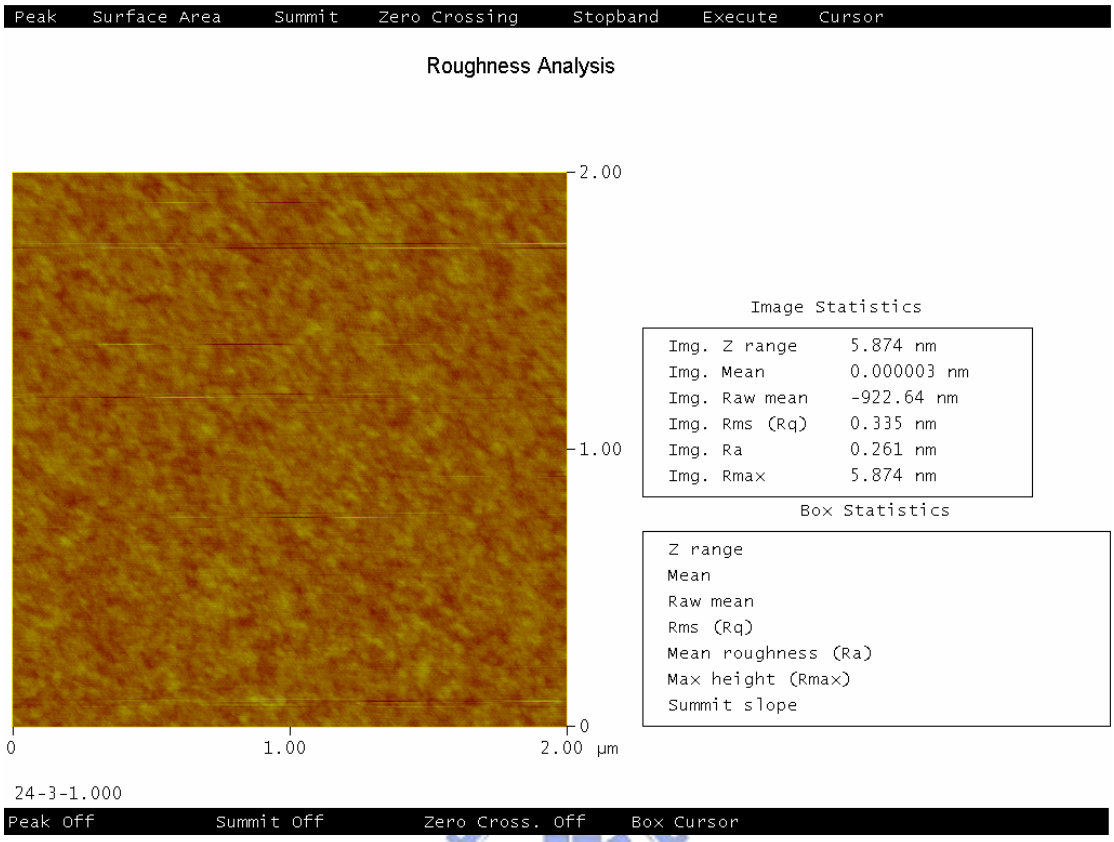

Figure 3-49 The roughness of the $TiO_{2-x}N_x$ thin film deposited on base of glass.

3.9 Sputter's Power and Time Effect on Absorption spectra

We plan to prove the effect of sputtering power and sputtering time is the same result for thickness. In Fig. 3-50, UV-visible absorption spectra of the $TiO_{2-x}N_x$ thin film deposited by 100W sputtering power supply and N_2/O_2=7/2 flow rate with various time is shown. With increasing sputtering time, the shoulder of UV-visible absorption at nearly 400nm shifts from UV region to visible region. So that we use the $TiO_{2-x}N_x$ thin film deposited by 60min sputtering time and N_2/O_2=7/2 flow rate with 120W power supply. In Fig. 3-51, the thickness of the $TiO_{2-x}N_x$ thin film deposited by 60min sputtering time and N_2/O_2=7/2 flow rate with 120W power supply is about 122nm. In Fig. 3-52, the thickness of the $TiO_{2-x}N_x$ thin film deposited by 70min sputtering time and N_2/O_2=7/2 flow rate with 100W power supply is about 122nm. These two samples of UV-visible absorption spectra are almost the same in Fig. 3-54. UV-visible absorption spectra of the $TiO_{2-x}N_x$ thin film deposited through N_2/O_2=7/2 flow rate with various time and power supply in order to get the same thickness can be the same result. Both sputtering time and power supply can control the thickness of the $TiO_{2-x}N_x$ thin film.

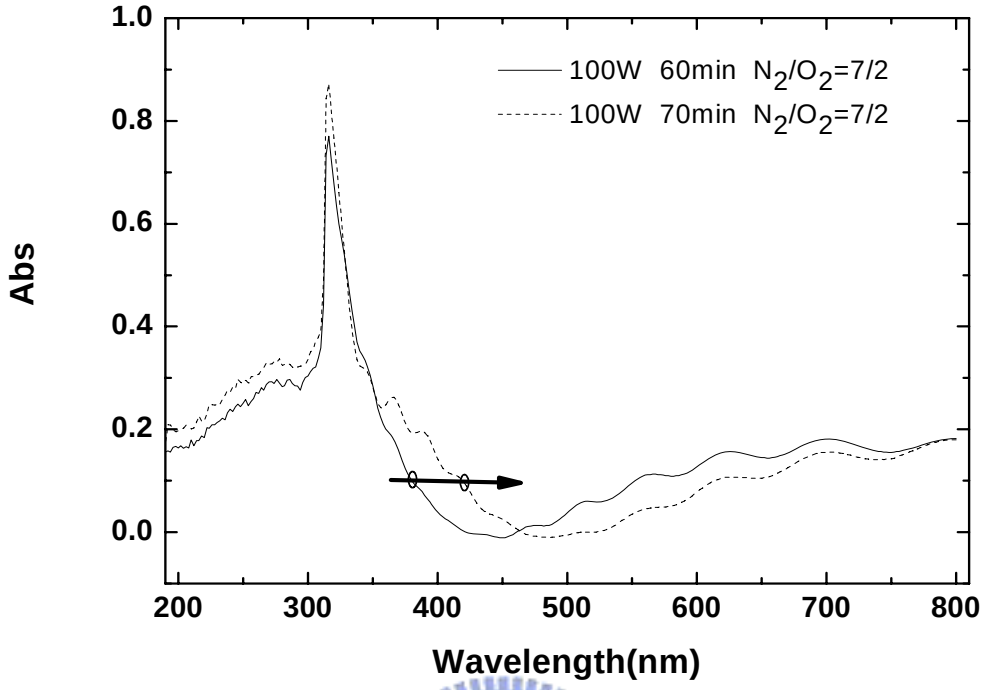

Figure 3-50 UV-visible absorption spectra of the $TiO_{2-x}N_x$ thin film deposited by 100W sputtering power supply and N_2/O_2=7/2 flow rate with various time.

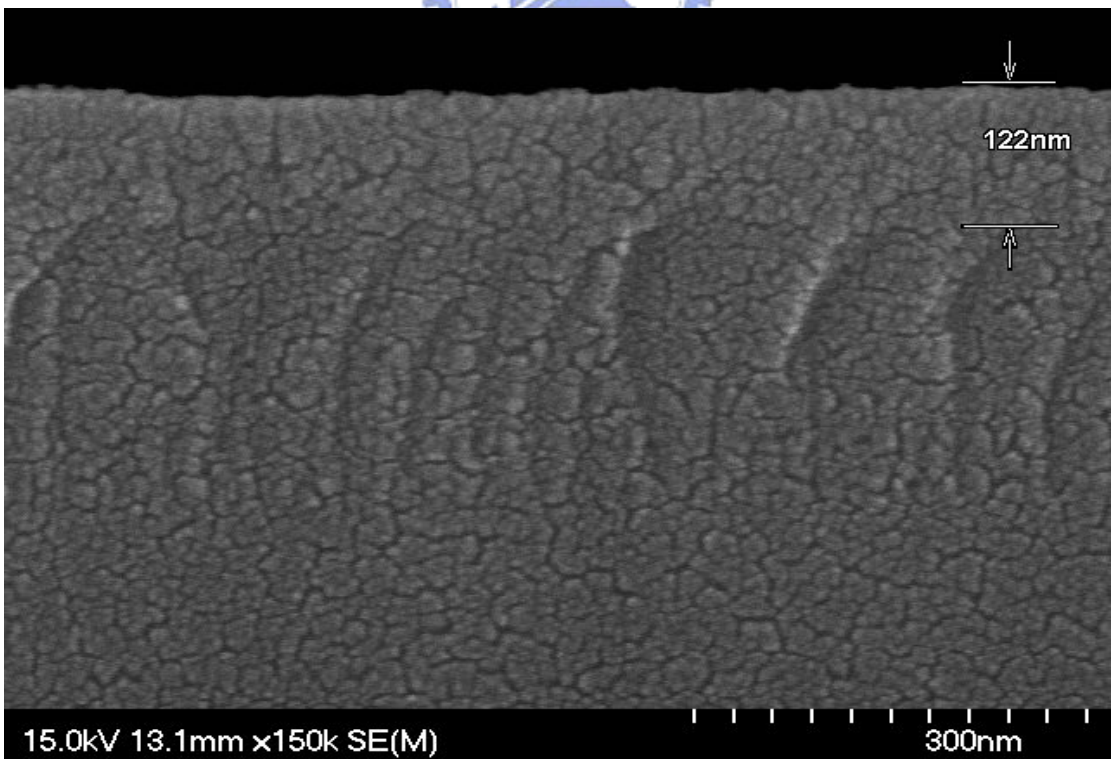

Figure 3-51 SEM images of the $TiO_{2-x}N_x$ thin film deposited by 60min sputtering time and N_2/O_2=7/2 flow rate with 120W power supply.

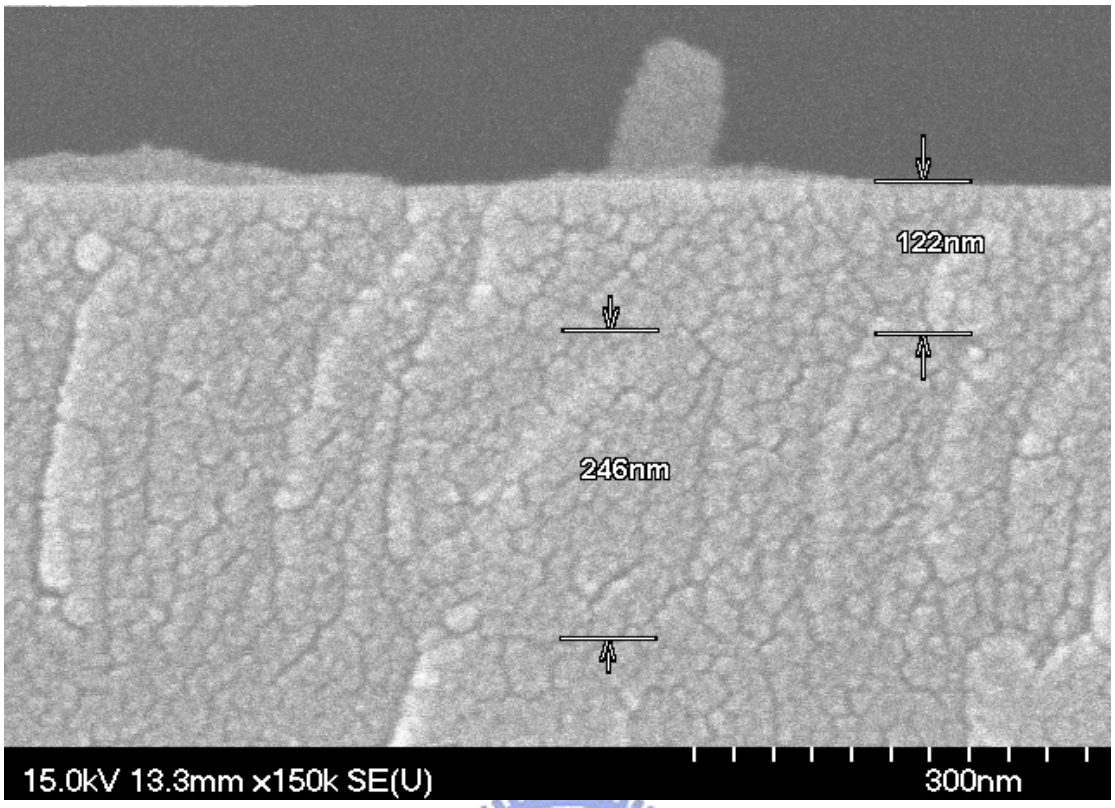

Figure 3-52 SEM images of the $TiO_{2-x}N_x$ thin film deposited by 70min sputtering time and N_2/O_2=7/2 flow rate with 100W power supply.

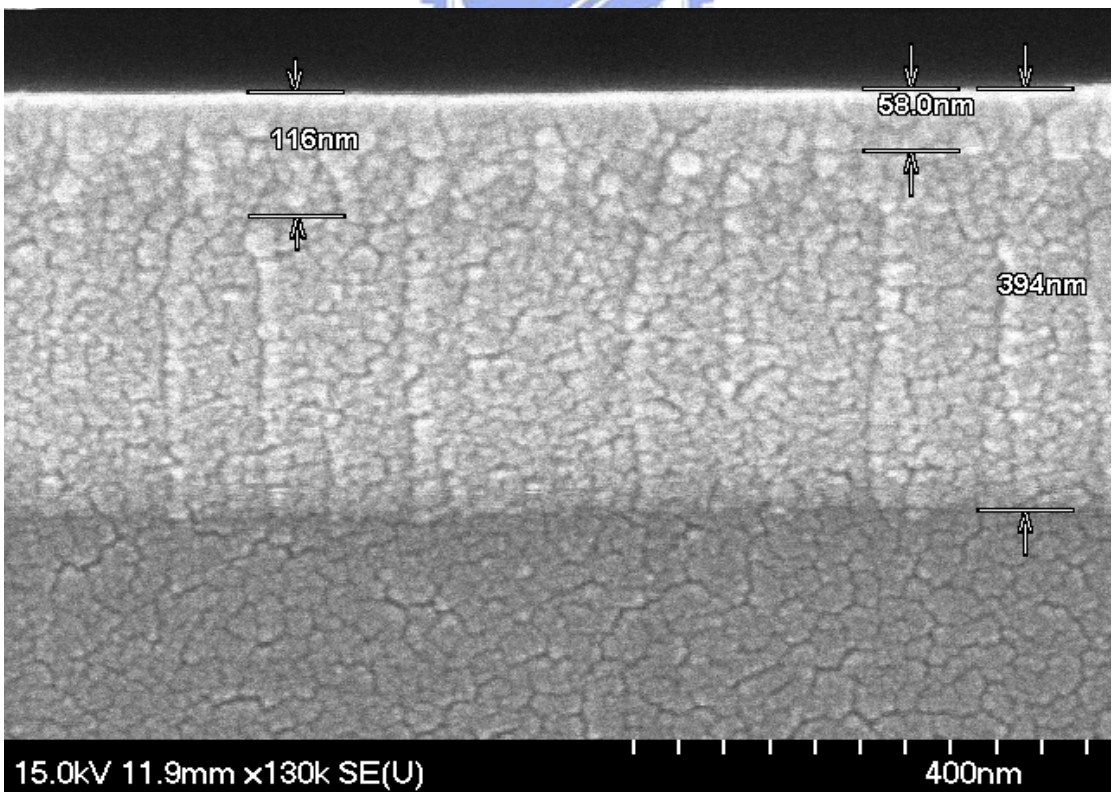

Figure 3-53 SEM images of the $TiO_{2-x}N_x$ thin film deposited by 60min sputtering time and N_2/O_2=7/2 flow rate with 100W power supply.

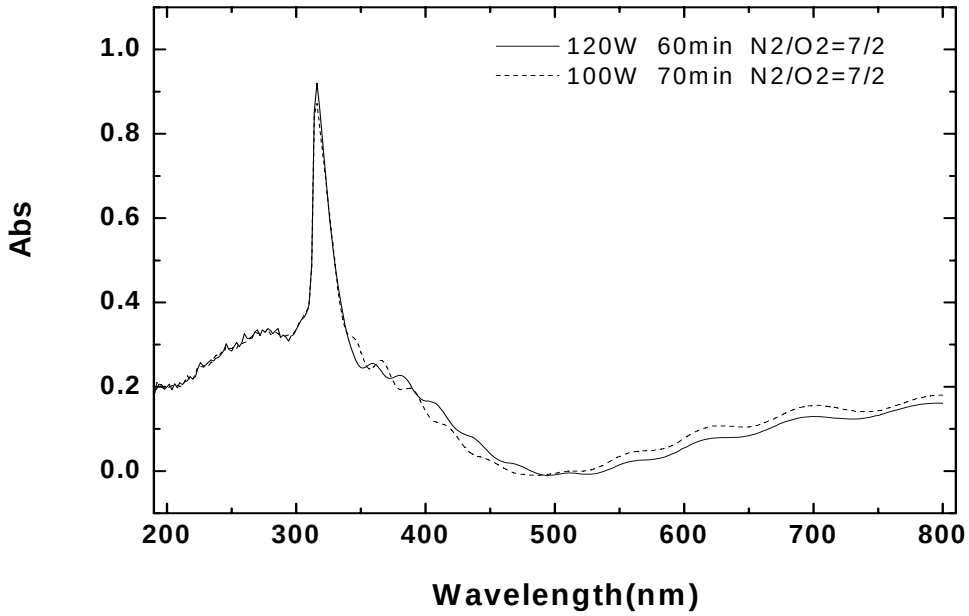

Figure 3-54 UV-visible absorption spectra of the $TiO_{2-x}N_x$ thin film deposited through N_2/O_2=7/2 flow rate with various time and power supply in order to get the same thickness.

Chapter 4 Conclusions

The PET and glass plates coated with TiO2-xNx thin films have obvious approach in hydrophilicity under UV and visible light irradiation. UV-VIS absorbance spectroscopy of PET and glass coated with $TiO_{2-x}N_x$ thin films appear a significant shift of the absorption edge to a lower energy in the visible-light region. Absorbance of $TiO_{2-x}N_x$ thin films is better with increasing thickness, and there are peaks of absorbance in the visible region. The peak intensity of absorbance on glass substrate are wider and larger than that on PET substrate in UV-light region. Therefore, the water contact angles on glass substrates are smaller than those on PET substrates upon UV-light illumination. The peak intensity of absorbance on glass substrate are narrower and smaller than that on PET substrate in VIS-light region. Therefore, the water contact angles on glass substrates are bigger than those on PET substrates upon VIS-light illumination. The amounts of nitrogen doping on $TiO_{2-x}N_x$ thin film appear direct proportion of influences on photo-generated hydrophilicity of thin films. The optical energy band gaps of $TiO_{2-x}N_x$ thin films narrow with increasing nitrogen. The mid-gap level energy band gaps of $TiO_{2-x}N_x$ thin films can be near 2.0eV. The photo-induced surface wettability conversion reaction of the thin films was investigated by water contact angle measurement. PET and glass plates coated with $TiO_{2-x}N_x$ thin films were found to exhibit a low water contact angle than without coated membranes when the surfaces were illuminated with UV and visible light in the air. The $TiO_{2-x}N_x$ thin film on the PET substrate upon UV-VIS light illumination exhibits lowest water contact angle near 8° and 35°, respectively. Because of roughness and intensity of absorbance, water contact angles of glass plates coated with $TiO_{2-x}N_x$ thin films are smaller than water contact angles of PET plates coated with $TiO_{2-x}N_x$ thin films. The surface of PET and glass are expected to

be smooth. Roughness and the photo-induced surface wettability conversion reaction of the thin films affect the degrees of water contact angles.

References

[1] Takeshi MORIKAWA, Ryoji ASAHI, Takeshi OHWAKI, Koyu AOKI and Yasunori TAGA " Band-Gap Narrowing of Titanium Dioxide by Nitrogen Doping " *Jpn. J. Appl. Phys*. Vol. 40 (2001) pp. L 561–L 563 Part 2, No. 6A, 1 June 2001.

[2] Shahed U. M. Khan, Mofareh Al-Shahry, William B. Ingler Jr." Efficient Photochemical Water Splitting by a Chemically Modified n-TiO2 " *SCIENCE* VOL 297 27 SEPTEMBER 2002.

[3] Kesong Yang, Ying Dai, Baibiao Huang, and Shenghao Han " Theoretical Study of N-Doped TiO2 Rutile Crystals "*J. Phys. Chem. B* 2006, 110, 24011-24014.

[4] Hiroshi Irie, Yuka Watanabe, and Kazuhito Hashimoto* "Nitrogen-Concentration Dependence on Photocatalytic Activity of TiO2-*x*N*x* Powders "*J. Phys. Chem. B* 2003, 107, 5483-5486.

[5] Hiroshi Irie,*a* Seitaro Washizuka,*a* Norio Yoshino*b* and Kazuhito Hashimoto**a* " Visible-light induced hydrophilicity on nitrogen-substituted titanium dioxide films " *CHEM. COMMUN.*, 2003, 1298–1299 .

[6] Ren-De Sun, Akira Nakajima, Akira Fujishima, Toshiya Watanabe, and Kazuhito Hashimoto, "Photoinduced Surface Wettability Conversion of ZnO and TiO2 Thin Films "*J. Phys. Chem. B* 2001, *105,* 1984-1990.

[7] R. Asahi, T. Morikawa, T. Ohwaki, K. Aoki, Y. Taga "Visible-Light Photocatalysis in Nitrogen-Doped Titanium Oxides "*SCIENCE* VOL 293 13 JULY 2001

[8] Jeromerajan Premkumar, "Development of Super-Hydrophilicity on Nitrogen-Doped TiO_2 Thin Film Surface by Photoelectrochemical Method under Visible Light "*Chem. Mater,* 16 (21), 3980 -3981, 2004. 10.1021/cm049055g.

[9] Jun-Bo Hana, Xia Wanga, Nian Wanga, Zheng-He Weia, Guo-Ping Yua, Zheng-Guo Zhoua, Qu-Quan Wanga,b,* "Effect of plasma treatment on hydrophilic properties of

TiO2 thin films "*Surface & Coatings Technology* 200 (2006) 4876 – 4878 .

[10] T. Watanabea, A. Nakajimaa, R. Wanga,1, M. Minabea, S. Koizumia, A. Fujishimab, K. Hashimotoa "Photocatalytic activity and photoinduced hydrophilicity of titanium dioxide coated glass "*Thin Solid Films* 351 (1999) 260±263 .

[11] Masahiko Maeda* and Teruyoshi Watanabe "Visible Light Photocatalysis of Nitrogen-Doped Titanium Oxide Films Prepared by Plasma-Enhanced Chemical Vapor Deposition "*Journal of The Electrochemical Society*, 153 (3) C186-C189 (2006).

[12] Marta Mrowetz, William Balcerski, A. J. Colussi, and Michael R. Hoffmann "Oxidative Power of Nitrogen-Doped TiO2 Photocatalysts under Visible Illumination " *J. Phys. Chem. B,* Vol. 108, No. 45, 2004 .

[13] Soon-Kil Joung, Takashi Amemiya, Masayuki Murabayashi, and Kiminori Itoh "Mechanistic Studies of the Photocatalytic Oxidation of Trichloroethylene with Visible-Light-Driven N-Doped TiO2 Photocatalysts "*Chem. Eur. J.* 2006, 12, 5526 ─ 5534.

[14] Masahiko Maeda, Teruyoshi Watanabe "Evaluation of photocatalytic properties of titanium oxide films prepared by plasma-enhanced chemical vapor deposition "*Thin Solid Films* 489 (2005) 320 – 324.

[15] K. Prabakar, T. Takahashi,a_ and T. Nezuka , T. Nakashima , Y. Kubota , A. Fujishima " Effect of nitrogen on the photocatalytic activity of TiO*x*N*y* thin films "*J. Vac. Sci. Technol.* Jul/Aug 2006 .

[16] S. Buzby , M. A. Barakat , H. Lin , C. Ni , S. A. Rykov and J. G. Chen , S. Ismat Shaha "Visible light photocatalysis with nitrogen-doped titanium dioxide nanoparticles prepared by plasma assisted chemical vapor deposition "*J. Vac. Sci. Technol.* May/Jun 2006.

[17] Xu Dong Chena,b,_, Zhi Wanga, Zheng Fu Liaob, Yu Liang Maic, Ming Qiu Zhanga,b, "Roles of anatase and rutile TiO2 nanoparticles in photooxidation of polyurethane

"*Polymer Testing* 26 (2007) 202—208.

[18] Naresh C. Saha and Hadand G. Tompkins "Titanium nitride oxidation chemistry: An x-ray photoelectron spectroscopy study "*J. Appt. Phys*, Vol. 72, No. 7, 1 October 1992.

[19] Rong Wang, Nobuyuki Sakai , Akira Fujishima, Toshiya Watanabe, and Kazuhito Hashimoto " Studies of Surface Wettability Conversion on TiO_2 Single-Crystal Surfaces " *J. Phys. Chem. B,*103 (12), 2188 -2194, 1999. 10.1021/jp983386x

[20] V. Rico, C. Lo' pez, A. Borra' s, J.P. Espino' s, A.R. Gonza' lez-Elipe " Effect of visible light on the water contact angles on illuminated oxide semiconductors other than TiO2 " *Solar Energy Materials & Solar Cells* 90 (2006) 2944 – 2949

[21] Nadica D. Abazovi, Mirjana I. omor, Miroslav D. Dramianin, Dragana J. Jovanovi, S. Phillip Ahrenkiel, and Jovan M. Nedeljkovi "Photoluminescence of Anatase and Rutile TiO2 Particles "

[22] Marshall D. Earle "The Electrical Conductivity of Titanium Dioxide **"***Phys. Rev.* 61, 56 - 62 (1942).

[23] Francisco, E; Bermejo M, Garcia Baonza V, Gerward L, Recio JM (2003). "Spinodal equation of state for rutile TiO_2". *Physical Review B* 67 (6): 064110-1.

[24] This article incorporates text from the Encyclopædia Britannica Eleventh Edition, a publication now in the public domain.

[25] "Stem Cell Attachment to Layer-by-Layer Assembled TiO2 Nanoparticle Thin Films" Dinesh S. Kommireddy, Shashikanth M. Sriram, Yuri M. Lvov, David K. Mills, *Biomaterials*, 2006, 27, 4296-4303.

[26] "Layer-by-Layer Assembly of TiO2 Nanoparticles for Stable Hydrophilic Biocompatible Coatings" Dinesh S. Kommireddy, Amish A. Patel, Tatsiana G. Shutava, David K. Mills, Yuri M. Lvov. *Journal of Nanoscience and Nanotechnology*, 2005, 5, 1081-1087.

[27] Nanotubes with the TiO2-B structure Graham Armstrong, A. Robert Armstrong, Jesús

Canales and Peter G. Bruce *Chemical Communications*, 2005, (19), 2454 - 2456 Abstract

[28] "Titanium dioxide (TiO2) as photocatalyst" , *Green Quest Technology*

[29] Jacob Israelachvili, *Intermolecular and Surface Forces*, Academic Press (1985-2004)

[30] T S Chow " Wetting of rough surfaces " *J. Phys*.: Condens. Matter **10** No 27 (13 July 1998) L445-L451

[31] P.G. de Gennes " Wetting: statics and dynamics " *Reviews of Modern Physics*, 57, 3 (part I), July 1985, p.827-863.

[32] " Layer-by-Layer Assembly of TiO2 Nanoparticles for Stable Hydrophilic Biocompatible Coatings" Dinesh S. Kommireddy, Amish A. Patel, Tatsiana G. Shutava, David K. Mills, Yuri M. Lvov. *Journal of Nanoscience and Nanotechnology,* 2005, 5, 1081-1087.

[33] A.K. vam der Vegt & L.E. Govaert, Polymeren, van keten tot kunstof .

[34] Agricola, Georgius, De re metallica, translated by Herbert Clark Hoover and Lou Henry Hoover, *Dover Publishing*

[35] Marchand , R . , Brohan , L . , Tournoux , M . , *Mater . Res . Bull* . , 15 1129 (1980).

[36] Banfield, J . , Veblen , D . , Smith , D . , *Am . Mineral* . , 76 343 (1980).

[37] http://www.lasurface.com/database/elementxps.php.

簡歷

姓名：余松蒔

性別：男

生日：72．06．15

出生地：桃園

籍貫：台灣桃園

學歷：國立武陵高中

國立彰化師範大學電機工程系

國立交通大學電子研究所

論文題目：

以濺鍍法製備氮摻雜二氧化鈦薄膜物性及光學特性之研究

Physical and Optical Characteristics of Sputtered Deposited TiO2-xNx Thin Films